Grain Boundary Structure, Phase Transitions and Segregation Phenomena in Copper Alloys

Dissertation

zur

Erlangung des Grades Doktor-Ingenieur

der

Fakultät für Maschinenbau

der Ruhr-Universität Bochum

von

Thorsten Meiners

aus

Lingen (Ems)

Bochum 2019

Science doesn't always go forward. It's a bit like doing a Rubik's cube. You sometimes have to make more of a mess with a Rubik's cube before you can get it to go right.

Jocelyn Bell Burnell

Acknowledgment

Abstract

The improvement of engineering materials as well as the development of new materials has been always a strong objective of research. The effect of grain boundaries in materials has drawn special attention, since they have an enormous impact on the properties. Especially the mechanical properties can vary strongly with respect to grain boundary density (grain size) and structure. Since many decades the field of grain boundary engineering deals with manipulating these crystal defects in order to tailor the material's properties with respect to certain applications. The atomic structure and local chemistry of the grain boundary mainly determine its properties (such as mobility, cohesive strength, energy, etc.) and how they relate to the materials performance. The observation of the local atomic structure and chemistry, however, brings extreme difficult experimental conditions with it and limits this field up to date. The enormous development of transmission electron microscopy in combination with increasing computational power for atomistic simulations has led to a huge progress in this field. But, due to the high complexity of grain boundaries, the observation of the local atomic structure is limited to special tilt grain boundaries, where both grains share a common low index zone axis parallel to the electron beam.

In this thesis, grain boundary structures and phenomena in pure copper and different copper alloys have been investigated in detail by high resolution scanning transmission electron microscopy in combination with atomistic simulations. The work comprises the observation of congruent grain boundary phase transitions in pure copper, chemically triggered structural transitions in copper-zirconium and copper-tantalum alloys and the investigation of sulfur-induced embrittlement in high purity, polycrystalline copper alloys.

Copper thin films were grown on Sapphire which leads to a strong [111] texture and mostly $\Sigma 3$, $\Sigma 7$, $\Sigma 19b$ and $\Sigma 37c$ tilt grain boundaries are formed. These tilt boundaries are perfectly suited for high resolution imaging. The main focus was on a special high angle tilt grain boundaries, the $\Sigma 19b$. Two different symmetric variants, with strongly differing atomic structures were found, which were named the zipper structure with $(2\bar{5}3)$ and the pearl structure with $(1\bar{8}7)$ grain boundary planes. Additionally, asymmetric variants are frequently found in the specimen. In the $\Sigma 19b$, $(1\bar{8}7)$ (and its asymmetric variants), congruent grain boundary phase transitions were observed, where two grain boundary phases coexist at the same time. With corresponding atomistic simulations, the transition was determined to be of first order and the two grain boundary phases are characterized by different excess volumes and stresses. The different $\Sigma 19b$ grain boundaries were also alloyed with zirconium and tantalum and the atomic structure was compared to the clean grain boundaries. It was found that tantalum particles form along the grain boundaries and pin them via the Zener effect. Locally, this introduces a curvature of the grain boundary plane. Zirconium, however, was found to segregate to grain boundary steps of the zipper structure and induces structural transitions at the facets between the steps. If no steps are present as such in the pearl structure, zirconium segregates homogeneously and induces a strong atomic disorder.

Sulfur-induced embrittlement is a problem since more than 100 years and was explained by sulfur segregating to grain boundaries. But a direct proof of the exact location and structure / distribution of sulfur at the grain boundaries was still missing. In this study, random high angle and low angle grain boundaries of polycrystalline copper were investigated by high resolution transmission electron microscopy and atom probe tomography. It is shown that sulfur is not decorating the grain boundaries homogeneously, but forms copper sulphides at the grain boundaries. These sulfides are possible sites for crack nucleation and favor intergranular fracture.

Preface

Paper I

Experimental observations of grain boundary phase transitions unveiled by atomistic simulations

Thorsten Meiners, Timofey Frolov, Robert E. Rudd, Christian H. Liebscher and Gerhard Dehm

Nature **579**, 375-378 (2020)

Paper II

Tantalum and zirconium induced structural transitions at complex [111] tilt grain boundaries in copper

Thorsten Meiners, Jazmin M. Duarte, Gunther Richter, Christian H. Liebscher and Gerhard Dehm

Manuscript accepted by *Acta Materialia*

Paper III

Sulfur-induced embrittlement of high-purity, polycristalline copper

Thorsten Meiners, Zirong Peng, Baptiste Gault, Christian H. Liebscher and Gerhard Dehm

Acta Materialia **156**, 64-75 (Sept. 2018)

Paper I: Thorsten Meiners' contribution to this paper comprises the macroscopic and microscopic investigations with optical light microscopy, scanning electron microscopy, electron backscatter diffraction, and scanning transmission electron microscopy. He was also responsible for the sample preparation. The copper alloys were produced by Montanwerke Brixlegg. The tensile tests were performed by Gerhard Bialkowski at MPIE in Düsseldorf. The wave-length dispersive spectroscopy investigations were performed by Irina Wossack. Zirong Peng and Baptiste Gault conducted the atom probe tomography measurements and Daniel Kurz did the wet chemical analysis of the copper alloys. Thorsten Meiners wrote the manuscript with a contribution from Zirong Peng and Baptiste Gault about atom probe. All authors discussed the results and contributed to the final manuscript.

Paper II: The thin films used in this paper were produced by the group of Gunther Richter at the Max-Planck-Institute for Intelligent Systems in Stuttgart. The characterization of the films by EBSD was performed by Thorsten Meiners. He also conducted all scanning transmission electron microscopy measurements and the image simulations using the Prismatic software. The grain boundary structure prediction and molecular dynamic simulations were done by Timofey Frolov from the Lawrence Livermore National Laboratory in Livermore, California (USA). The manuscript was written by Thorsten Meiners with equal contributions from Christian Liebscher and Timofey Frolov. All authors have contributed to the interpretation and discussion of the results and revised the final manuscript.

Paper III: For this work, the same copper thin films, grown in the group of Gunther Richter at the Max-Planck-Institute for Intelligent Systems in Stuttgart, were used. The characterization of the films by EBSD was done by Thorsten Meiners. He also employed all (scanning) transmission electron microscopy and corresponding analytical techniques. The atom probe characterization was performed and analyzed by Jazmin Duarte. The manuscript was written by Thorsten Meiners. All authors revised the manuscript and interpreted the data.

Contents

Nomenclature

ABF .... Annular bright field

ADF .... Annular dark field

AES .... Auger electron spectroscopy

Ag .... Silver

AIFs .... Amorphous intergranular films

APT .... Atom probe tomography

ATGB .... Asymmetrical tilt grain boundaries

BF .... Bright field

BSE .... Backscattered electrons

CCD .... Charge coupled device

Co .... Cobalt

CSL .... Coincident site lattice

CTEM .... Conventional transmission electron microscopy

CTF .... Contrast transfer function

LAGBs .... Low angle grain boundaries

LMIS .... Liquid metal ion source

MBE .... Molecular beam epitaxy

MD .... Molecular dynamic

nc .... Nano-crystalline

O .... Oxygen

OLM .... Optical light microscopy

ppm .... Parts per million

PSF .... Point spread function

S .... Sulfur

SDD .... Silicon drift detector

SE .... Secondary electrons

SEM .... Scanning electron microscopy

SIMS .... Secondary ion mass spectroscopy

STEM .... Scanning transmission electron microscopy

STGB .... Symmetrical tilt grain boundaries

SU .... Structural unit

Ta .... Tantalum

TEM .... Transmission electron microscopy

TKD .... Transmission Kikuchi diffraction

TOF .... Time of flight

UTS .... Ultimate tensile strength

WDS .... Wavelength-dispersive X-ray spectroscopy

WPOA .... Weak phase object approximation

ZLP .... Zero loss peak

Zr .... Zirconium

1. Introduction and Motivation

1.1. Introduction

Most engineering materials are composed of a polycrystalline microstructure. The regions separating individual grains are specified as grain boundaries (GBs) and they are one of the most prominent planar defects in materials. Hence, GBs play a crucial role in dictating material's properties and novel concepts even predict that they can be used as material design elements [1, 2]. The structure of GBs is determined by the alignment of two abutting grains and atoms adopt an arrangement that best resembles the two crystal lattices [3]. The deviating atomic order at the GB core strongly determines their energy, cohesive strength, mobility, diffusivity or sliding resistance [4–7]. Segregation of impurity elements can complicate the situation even more by changing the GB structure and properties. While this is probably the most promising way towards GB engineering to tailor the materials properties [8], it can also lead to dramatic failure of the material [9].

In addition, GBs themselves can exist in multiple phase states and undergo phase transitions, which has been already predicted by thermodynamic considerations more than 50 years ago [10, 11]. The underlying assumption was that multiple stable and metastable states exist for each GB orientation [12, 13]. The terminology complexion was recently introduced to distinguish between those interfacial states that differ in any equilibrium feature [14]. All these considerations together reveal the great complexity of these crystal defects. The main challenge to establish a generalized picture in this field results from the huge variety of GB types [15], the difficulty to experimentally access their atomic structure and to correlate it directly to the GB properties.

A lot of effort has been made over many decades in order to understand the effect of the atomic GB structure on the GB properties [15–19]. Even though many experimental and theoretical studies have been employed to unravel the structure, energy, mobility and diffusion behavior of special GBs, a detailed understanding of the atomistic mechanisms of GBs, segregation effects, phase transitions and their impact on materials properties is lacking [16, 18, 20–25].

The development of aberration-corrected transmission electron microscopes (TEM) made it possible to experimentally access the atomic structure and chemistry of GBs. In recent years, several studies explored the atomic arrangements of tilt GBs in ceramic, metallic and semiconductor systems [23, 26–31]. However, from the experimental data alone, it is difficult to extract the underlying thermodynamic and kinetic properties of the GBs. But in combination with complementary atomistic simulations it is possible to unravel the atomic structure and intrinsic GB properties, such as segregation behavior, structural GB transitions and cohesive properties [1].

1.2. Aim and outline of this thesis

The main topic of this work is based on the atomic scale observation of random and special tilt GBs. The goal is to correlate the GB structure to specific GB properties and conclude from these findings the effect on the macroscopic properties of the material itself. To understand these atomistic mechanisms and the effect on the properties is crucial for GB engineering. To achieve this goal, perfect tilt GBs are obtained by defined thin film growth via molecular beam epitaxy (MBE). Additional thin films of different elements and subsequent annealing can be used to alloy the primary material. The combination of electron backscatter diffraction and the focused ion beam allows the defined and repeatable extraction of specific GBs from the thin film to be able to compare the same GB in different conditions (as grown, annealed, alloyed with different elements, etc.). Aberration-corrected (scanning) TEM techniques (imaging, energy-dispersive X-ray spectroscopy and electron energy loss spectroscopy) are

---

[1]The text in this chapter contains parts of the three manuscripts presented in the chapters 6, 7 and 8[18][32].

coupled with atom probe tomography and atomistic simulations to investigate the atomic structure and local chemistry. Of special interest are structural transitions of GBs in pure metallic systems (but also alloys are of interest in this thesis). Such transitions may result in changing GB properties, such as its energy, mobility and cohesive strength. Therefore, also the macroscopic properties may change strongly. However, experimental studies in this field are still missing and are therefore interesting and important to address, since many phenomena still have to be explained, such as abnormal grain growth (GB mobility changes) or activated sintering (GB diffusivity changes). The chosen main material in this thesis is copper (Cu), since it is a well investigated material and many physical and chemical properties are well known. In addition, it is strongly used in industry and it is always of interest to improve Cu and its alloys. This work comprises the following main investigations:

1. Investigations of special tilt GBs (mainly $\Sigma 19b$ and its asymmetric variations) from Cu thin films grown on (0001) oriented Sapphire, with respect to its atomic structure and GB phase transitions. The combination of high resolution imaging and computer simulations reveal the existence of a first order GB phase transition of a symmetric $\Sigma 19b$ and vicinal GBs and is discussed in chapter 6.

2. The Cu thin film is alloyed with zirconium (Zr) and tantalum (Ta). The structures of the pure GBs are then directly compared with respect to structural/chemical transitions induced by Zr or Ta. In addition, the effect of these alloys to the GBs is related to the stabilization mechanism in nanocrystalline copper (see chapter 7).

3. The investigation of engineering, ultra pure Cu and Cu- sulfur (S) alloys in order to identify with atomic precision the origin of the embrittlement effect of S. The samples contain mostly random grain boundaries and represent a real material. The characterization of random GBs in these alloys cover a large range from the millimeter scale down to atomic distances by using optical microscopy, scanning electron microscopy, transmission electron microscopy and atom probe tomography and is presented in chapter 8. The investigated microstructural features will be then discussed with respect to the embrittlement phenomena. Macro-size tensile testing was performed at different temperatures (room tem-

perature, $200° C$ and $400° C$) with different S concentrations showing the embrittlement effect of S.

2. Grain boundaries

In this chapter the basic theoretical models of GBs, GB phase transitions, segregation as well as precipitation are described. It starts with a general introduction of GBs (section 2.1) followed by the description and categorization of GB structures (section 2.2). The thermodynamics behind GBs and GB phase transitions are described in section 2.3. Afterwards, the most common used models for GB segregation are introduced, which were developed by Gibbs and Langmuir and McLean (section 2.4). Instead of solute segregation, the impurity atoms can accumulate and form precipitates at the GBs if it is energetically more favorable (see section 2.5).

2.1. Introduction to grain boundaries

The interface between two abutting crystals with the same crystal structure, which are misoriented to each other, is called a GB. Even though the two crystals exhibit the same crystal structure and composition, these interfaces are very complex, two dimensional defects in a material. Nowadays, there are still many open questions considering e.g. the GB structure, the interplay between GBs and other defects or how GBs behave under certain thermodynamic conditions (e.g. stress, temperature and chemistry). In the early twentieth century, it was believed that a GB is an amorphous layer between two grains [17]. But soon it was found that this model does not fit to observed phenomena, such as the anisotropy of intergranular penetration of other elements [17]. One of the first theoretical models to describe the structure of GBs was developed by Read and Shockeley [33], called the intrinsic dislocation model, which describes the GB by a set of dislocations with Burgers vector b and spacing h and

links it to the misorientation of the two grains as $\Theta = \frac{b}{h}$. According to this model, the GB energy σ is proportional to the sum of all elastic contributions of the dislocations contained in a GB unit area as follows:

$$\sigma = \frac{G \cdot b}{4 \cdot \pi \cdot h(1 - v)} \left(ln \left(\frac{b}{2\pi\, r_0} \right) - ln \left(\frac{b}{h} \right) \right) \qquad (2.1)$$

where G is the shear modulus, v the Poisson ratio, and r_0 the radius of the dislocation core. An experimental example of such a GB is shown in Fig. 2.1 (a). This model works well for low angle GBs (LAGBs) ($\Theta \leq 15°$), but for higher misorientations, the dislocation spacing h becomes too small and the model fails. However, modifications / extensions of this model have been proposed for high angle GBs (HAGBs) and a good summary can be found in [17]. Furthermore, the dislocation model does not account for the distinct GB structure and it does not consider the microscopic degrees of freedom (explanation in the next subsection), nor the bonding type (e.g. covalent, metallic, etc.) or any atomic interaction at the GB core.
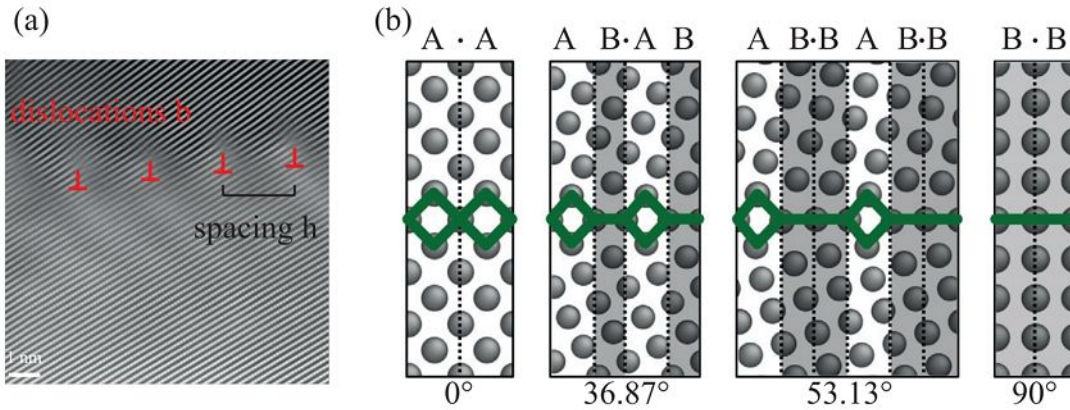
Fig. 2.1.: **Dislocation and structural unit model**: (a) high angle annular dark field scanning TEM image of a low angle GB showing dislocations with spacing h. (b) Principle of structural unit model. The two delimiting boundaries are at 0° and 90° and have the units A and B. All other GBs between $0 - 90°$ should be able to be built by these two units, as is shown for 36.87° and 53.13°. This figure is taken from ref [34].

With the advent of atomistic simulations these topis became a central aspect in predicting and explaining GB structures. Computer simulations of many high angle GBs (especially highly symmetric GBs in fcc crystals) were carried out, which take these considerations into account and describe the GBs on an atomic level. One simulation tool was the hard sphere model, proposed from Hornestra in 1959, which described

the atomic structure of GBs. It says that the GB core is an arrangement of polyhedral atomic units, which are built up with balls and sticks [35]. The number of local coordinations has to be optimized in order to get the best arrangement of atoms. Thus, it is a pure geometrical approach and was used more than 20 years, e.g by Frost et al. [20, 36]. Nevertheless, it was shown that this model has limits, especially with respect to metallic GBs [17]. Other simulation techniques focused more on the energy minimization with respect to the GB structure [16, 37]. Based on the simulated GB structures, the structural unit model was introduced for special coincident site lattice (CSL) GBs, which describes the atomic GB structure by repeating 2D building blocks (structural unit (SU)) [16, 37, 38]. In this model, a GB that consists of only one single SU type (e.g. $| A |$) is called a delimiting boundary. Such a boundary is shown in Fig. 2.1 (b) for 0° and 90° and the units A and B. The SU model predicts that each GB with a certain misorientation Θ_{GB} can be constructed using a combination of the units from two delimiting GBs (with SUs $| A |$ and $| B |$) with misorientations $\Theta_{GB \pm \delta}$ (one GB with smaller and one with higher misorientation). This is schematically demonstrated in Fig. 2.1 (b). Many theoretical studies focused on the description of the SUs of different symmetric and asymmetric GBs [16, 20, 21, 37]. Frost et al. [20] presented a catalogue of predicted structures for [001], [011] and [111] symmetric tilt GB in face-centered cubic (fcc) hard sphere crystals. Wang et al. [21] followed the approach and presented structures of [001] and [111] tilt GBs and their energies. However, more recent studies have shown that the SU model does not work in general for all kinds of GB, e.g in low stacking fault materials and for long period GBs [39, 40]. Therefore, the SU model was revisited and extended by Han et al. [34] including stable and metastable GB structures as delimiting boundaries in order to extend the complexity of GBs. In this thesis, it will be shown, that [111] tilt GBs in pure Cu do even not serve the extended SU model, but seem to have a much higher complexity (see chapter 7).

2.2. Description of grain boundaries

A full, geometrical description of a general GB needs in total 5 macroscopic degrees of freedom [15]. Three are used to describe the misorientation between the two abutting

crystals and is commonly displayed by a rotation axis $[h_O k_O l_O]$ and an angle θ. The remaining 2 degrees of freedom describe the normal vector $\vec{n}$ of the shared plane between the two grains, the GB plane. This is illustrated schematically in Fig. 2.2 (a) for a pure tilt GB (i.e $[h_O k_O l_O] \perp \vec{n}$). In theory, "infinite" different GBs for only one misorientation exist if one considers a continuous change of the GB plane inclination. In reality, however, only a few GB plane inclination will be favored due to energetic reasons. In general, the GB inclination can be visualized by a Wulff plot, where each inclination is represented by a vector in normal $\vec{n}$ direction and a magnitude, which is proportional to the GB energy [41]. There are a few conditions, where a GB becomes a special boundary. If the rotation axis O is parallel or perpendicular to the GB plane $\vec{n}$, then the GB is called a pure twist or tilt GB. Furthermore, if the normal vector of the GB plane $\vec{n}$ is identical in the two grains, $(h_{G1} k_{G1} l_{G1}) = (h_{G2} k_{G2} l_{G2})$, then the GB is called symmetric. Based on these definitions, each GB can be described as follows:

$$\theta [h_o k_o l_o], (h_{G1} k_{G1} l_{G1})/(h_{G2} k_{G2} l_{G2}) \tag{2.2}$$
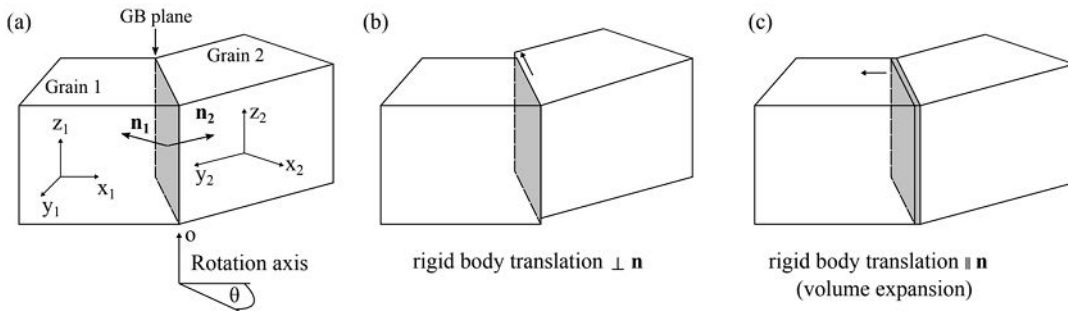
Fig. 2.2.: Tilt grain boundary geometry: (a) shows the orientation between two single crystals with their corresponding coordinate system. The misorientation is defined by the rotation axis O and the angle θ. The shared interface is the GB plane. Its orientation is defined by the two normal vectors $\vec{n}_i$. (b) and (c) schematically show rigid bod translations between both crystals perpendicular and parallel to the GB plane normal.

In addition to the macroscopic (geometrical) degrees of freedom, three microscopic degrees have to be added in order to fully describe the atomic structure of a GB. Rigid body translations describe small translations between the two grains in each direction [15]. If the translation is perpendicular to $\vec{n}$, it can be seen as a shear between both grains (see one possibility in Fig. 2.2 (b)), and if it is parallel to $\vec{n}$, the GB width widens (see Fig. 2.2 (c)), which is known as GB volume expansion [42].

The last feature of GB descriptions to mention here is the coincidence site lattice (CSL) model, which can be applied to GBs with special orientations of the two grains only [43]. Under specific misorientation conditions, a certain number of atom positions match by overlapping the two grains and form a superstructure. These positions are called coincidence sites and how many of them exist in a special configuration is typically given by a Σ value. The Σ value is determined by this ratio [15]:

$$\Sigma = \frac{\#\,of\,coincidence\,sites\,in\,an\,elementary\,cell}{\#\,total\,lattice\,sites\,in\,an\,elementary\,cell} \qquad (2.3)$$
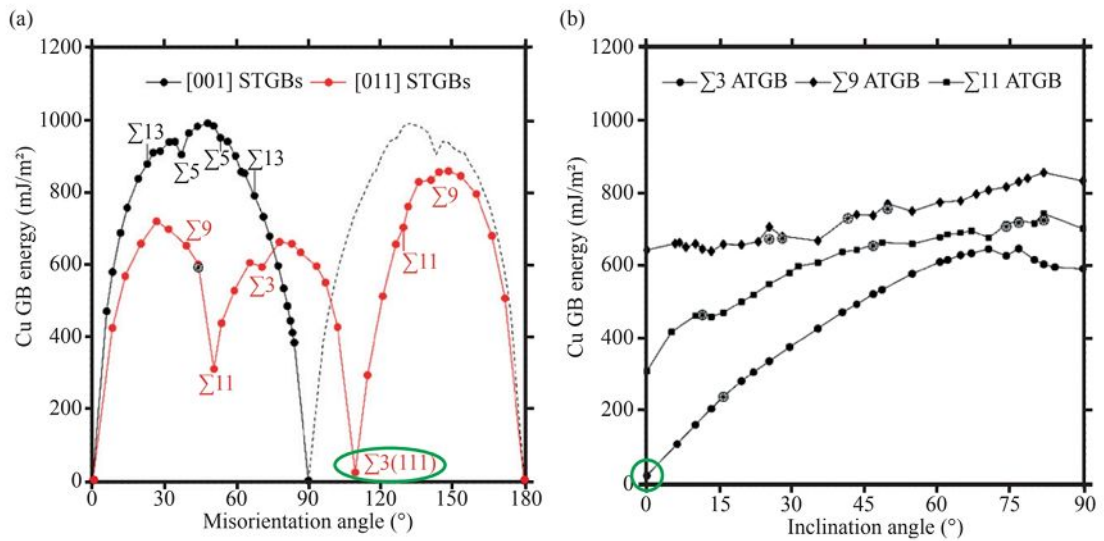
Fig. 2.3.: GB energy as a function of misorientation and GB plane inclination: (a) GB energy versus misorientation plot of [001] (in black) and [011] (in red) STGBs in Cu. (b) GB energy versus GB plane inclination angle for three different [011] ATGBs, the $\Sigma 3$, $\Sigma 9$ and $\Sigma 11$ in Cu. The data point at 0° belongs to the STGB of $\Sigma 3\,(111)$, $\Sigma 9\,(114)$ and $\Sigma 11\,(113)$, as indicated by the green circle examplarily for the $\Sigma 3\,(111)$. The plot is taken from [44].

In the easiest case, where two grains are joined without any / very small misorientation (like in a single crystal or in a LAGB), the Σ value is equal 1. The GB with the lowest Σ value is the twin boundary, which has a value of 3.

One important property of a GB is the GB energy, which depends strongly on the misorientation and GB plane inclination. The effect of misorientation is typically demonstrated by cusp plots, where the GB energy versus the misorientation is plotted. An example is shown in Fig. 2.3 (a) for [001] and [011] symmetrical tilt GBs (STGBs) in Cu and was taken from [44]. It demonstrates that LAGBs have smaller energies than

HAGBs. Furthermore, some CSL boundaries are local energy minima, e.g the $\Sigma 3$ (111) and $\Sigma 11$ (113), while other low Σ boundaries, such as the $\Sigma 9$, have a rather high energy compared to the other two. Also the GB plane inclination can have a strong effect on the GB energy, which is shown in Fig. 2.3 (b), where the GB energy is plotted against the inclination for three different low Σ GBs. The plot starts at a STGB (at $0°$) and with an increasing inclination angle the GBs become asymmetric tilt GBs (ATGB). The GB energy behaves differently for different GBs. For the $\Sigma 3$ and $\Sigma 9$ GB the energy increases strongly already for small inclination angles, while it stays rather constant for the $\Sigma 11$ GB. Thus, each GB type behaves quite different by changing certain geometric parameter. In this thesis the focus will be on symmetric and asymmetric $\Sigma 19$ [111] tilt GBs in chapters 6 and 7 and on general GBs in chapter 8.

2.3. Grain boundary thermodynamics and transitions

General thermodynamics can be used to describe GBs as was done already for other interfaces, such as free surfaces [41]. Even though GBs are non-equilibrium defects, a polycrystalline material with a GB network is an object with a local energy minimum and thus the GBs in the samples can be treated thermodynamically [45]. Gibbs popular description of dividing surfaces was the first thermodynamic description of interfaces [46]. This idea was further developed by John Cahn and is nowadays more commonly used [47]. Here the thermodynamic state variables are obtained from the internal energy of an open system with two identical grains. According to Gibbs, the internal energy is defined as [46]:

$$dU = TdS - PdV + \sum_{i=1}^{n} \mu_i dn_i + \sigma dA \qquad (2.4)$$

with U being the internal energy, T the temperature, S the entropy, P the pressure, V the volume, n_i the amount of components with their chemical potential μ_i and A is the GB area. Cahn defined σ as the GB energy per unit area at constant V and n_i,

which changes the internal energy of the system with respect to the GB area [47]:

$$\sigma = \left(\frac{\partial U}{\partial A}\right)_{S,V,n_i} \tag{2.5}$$

Equation 2.5 can also be rewritten with the help of the fundamental state function $G = U + PV - TS$ so that the GB energy becomes:

$$\sigma = \left(\frac{\partial G}{\partial A}\right)_{T,P,n_i} \tag{2.6}$$

with T, P and n being constant. This equation says that the Gibbs energy of the system is increased, when GBs are present in the bulk. It is stated that this is the most important representation of the GB energy per unit area. How much the GBs increase the Gibbs energy depends strongly on the GB energy, which is usually determined by the geometry and atomic structure (as seen before by the cusp plots), but also the composition, temperature and pressure play a role [15].

For now, the models describing the GB's structure minimize the energy in a low temperature regime (e.g. dislocation model, SU model, CSL model). At higher temperatures, however, the situation is more complicated and much less is known about the GB behavior [11]. Long time ago it was already stated that GBs can exist in different states, where each state has its own free energy. Therefore, the GBs can undergo phase transitions as bulk phases do, which can induce discontinuities of the GB properties [10]. Hart suggested that a GB can be seen as a 2D phase described by Gibbs thermodynamics. Also the term complexion has been introduced for the different GB phases and is seen as the 2D analogon to bulk phases [14]. In this thesis, however, the term GB phase will be used. The thermodynamics of GB phase transitions were intensively studied by Hart [10, 11], Cahn [12] and Rottman [13]. A GB phase transition can occur, if the two respective Gibbs free energy curves σ_1 and σ_2 (Equ. 2.6) cross, which is defined as a **non-congruent** transition, or only touch in one point, which is referred to as a **congruent** transition. This situation requires a change in at least one thermodynamic parameters change, e.g. the temperature T, the chemical potential μ or the composition (chemistry) n_i. During a congruent transition, the composition of the GB as well as the shape must remain unchanged [12]. In a non-congruent transition,

however, the GB composition, as well as the shape (involving faceting and dissociation) can be varied. The transition is a first-order transition, if the slopes of the free energy curves are discontinuous at the transition point [10, 11]. It comes along with changes in thermodynamic properties of the GBs and it was recently shown that also the excess volume and the GB stress tensor can be used to define a first-order transition [25].

congruent GB phase transition

Misorientation θ and
GB plane **n** stay constant

non-congruent GB faceting transition

Misorientation θ stays constant
GB plane: **n** facets into **n₁** and **n₂**

non-congruent GB dissotiation transition

GB plane **n** stays constant
Misorientation θ changes due to new
formed bulk phase into θ₁ and θ₂
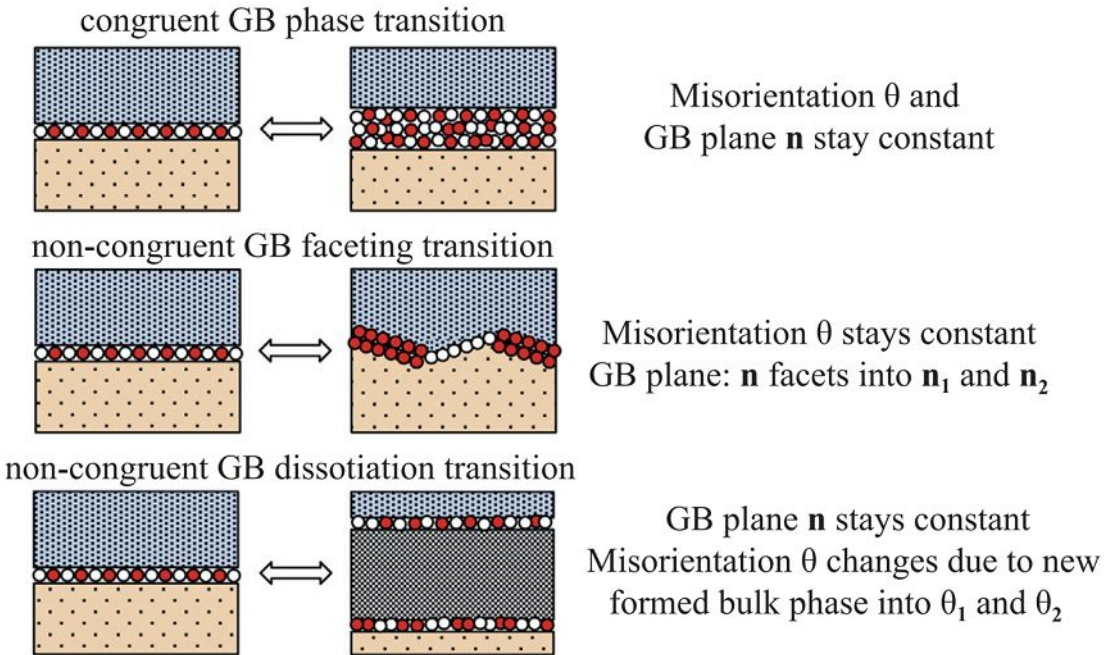
Fig. 2.4.: GB phase transitions: This figure demonstrates the categorization of GB phase transitions. (a) defines a congruent phase transition, (b) a non-congruent faceting transition and (c) a non-congruent dissociation transition. This figure was taken from [6].

In a pure (metallic) system, a congruent GB phase transition can be described on the atomic scale as a structural transition of the GB core structure. This may be, for example, the formation of new structural units or a melting transition. The misorientation and GB plane inclination remain constant (see Fig. 2.4 (a)). In multi-component systems, the composition must also remain constant during a congruent transition. In a non-congruent transition, all geometric parameter and also the composition can change. A typical non-congruent transition is the faceting transition (see Fig. 2.4 (b)). The GB splits up into facets, which have different GB planes n_1 and n_2, where the former GB plane is then defined as $n = n_1 + n_2$. If the misorientation between grain 1 and grain 2 changes, usually the transition is called a dissociation transition. Here the interface splits up and a new phase is formed. This builds up two new GBs between

grain 1 and 2 and the new phase. The planes of the new GBs are the same as before, but the misorientation changed (Fig. 2.4 (c)). Both types of non-congruent transitions can occur in pure and multi-component systems [41]. In multi-component systems, segregation can also be described as another non-congruent transition. Cahn proposed that congruent transitions in pure systems occur only at specific thermodynamic conditions according to the phase rule [12] and are very difficult to observe experimentally. Furthermore, he assumed that they occur mostly in non-equilibrium conditions, while they are highly unlikely in equilibrium conditions. In addition, these transition occur most likely at high symmetric GB orientations. However, it was recently predicted that these transitions may occur more frequently than thought [24, 25, 48, 49].

2.4. Grain boundary segregation

As GBs increase the Gibbs energy, the system always tends to reduce the energy gain in order to minimize the total Gibbs energy. This can be achieved in many ways, for example by interacting with other defects or by alloying / impurity elements. In this section, the interaction between GBs and foreign atoms will be briefly discussed. In many cases, it is thermodynamically favorable for solutes to accumulate at the GBs, thereby reducing the GB energy. Solute segregation describes all concentration changes of an element at the GB, if there is no formation of a new phase [50]. If a secondary particle/phase is formed, it is called GB precipitation. The difference between these two phenomena can be related to solubility. In general, the solubility of a solute in a bulk material can be very different to the one at a GB [51]. In general, segregation is divided into equilibrium and non-equilibrium segregation. **Equilibrium segregation** is a local redistribution of solutes at the GB caused by Gibbs energy minimization and depends strongly on the GB structure. The process is analogous to adsorption in surface science and the chemical potential of all species involved is constant. **Non-equilibrium segregation** appears when concentration gradients play a role, e.g during rapid cooling of an alloy (quenching). Thus, it deals with more kinetic events and is much more difficult to describe theoretically. Since in this thesis

all alloys/materials have been annealed and slowly cooled down, it is approximated that only equilibrium segregation needs to be considered here. That solute segregation reduces the Gibbs energy can be explained by different interaction mechanisms, which consider elastic and electronic effects. Elastic effects consider the difference of strain energy caused by solutes in the bulk and in the grain. One contribution is a size effect between solute and solvent atoms, which creates a strain field. The segregation energy is defined as the strain energy difference between the solute being in the GB or in the bulk [17]:

$$\Delta E_{segregation} = E_{strain}^{GB} - E_{strain}^{bulk} \tag{2.7}$$

A second contribution is the difference in elastic moduli of solutes and solvents. Since the GB is considered to be softer than the bulk, the strain energy of the solute is most likely smaller inside the GB [17]. Electronic effects on segregation are seen as difference in electronegativity between solutes and solvents and are well explained by the second and third Hume-Rothery rule (for more information see [52]).

GB segregation can be treated thermodynamically in many different approaches. The two most popular theorems are the **Gibbs adsorption theorem** [46] and the **Langmuir-McLean types of segregation isotherm** [53] and are coming from classical thermodynamics and will be described here briefly. For the variety of other approaches, the books of Lejcek [15] and Priester [17] provide good overviews and in detail bibliographical references.

The Gibbs adsorption theorem for a binary system (solute i and matrix M) is defined as [15, 46]:

$$\Gamma_{i,M}^{GB} = -RT^{-1} \cdot \left(\frac{\partial \sigma}{\partial ln(X_i)} \right)_{P,T} \tag{2.8}$$

where $\Gamma_{i,M}^{GB}$ is the adsorption of solutes i at the GB and X_i is the atom fraction of the solutes i in bulk. The equation relates the adsorption to the change in GB energy with respect to the solute concentration X_i in the bulk M. It has been frequently used for experimental purposes, to quantify for example the GB segregation of sulfur in iron [50]. However, it is very difficult to measure the solute bulk concentration X_i and the GB energy σ for many temperatures at the same time. Thus, it is easier and more popular to use the theorem of Langmuir and McLean. While the model of Gibbs is cal-

culated using pure thermodynamics and considers general liquid-liquid interfaces, the model of Langmuir and McLean is the first theory especially designed for GBs. It describes the pure thermodynamic approach of Gibbs with statistical mechanics. By distributing the solutes randomly at the GB, this model finds the minimum energy for a specific segregation configuration, with the assumption that the chemical potentials of all components stays constant. **The classical segregation isotherm of Langmuir-McLean** in a binary system is then defined as [15, 53]:

$$\frac{X_i^{GB}}{X_i^{GB,0} - X_i^{GB}} = \frac{X_i}{1 - X_i} \cdot exp\left(\frac{-\Delta G_i^{GB}}{RT}\right)$$ (2.9)

where $X_i^{GB,0}$ is the saturation concentration of solute i at the GB, X_i^{GB} the actual/measured solute concentration at the GB and ΔG_i^{GB} is the change in Gibbs free energy due to segregation. If the saturation concentration is assumed to be 1 (that means one monolayer) the equation can be approximated to:

$$\beta = \frac{X_i^{GB}}{X_i} = exp\left(\frac{-\Delta G_i^{GB}}{RT}\right)$$ (2.10)

where β is named the enrichment factor. This relation says, if $\Delta G_i^{GB} < 0$, then segregation increases with decreasing solubility of element i in the bulk. But at the same time, segregation decreases with increasing temperature. Since it is fairly easy to experimentally measure the excess concentration X_i^{GB} of the solutes i at the GB and the solute concentration X_i in the bulk, the Langmuir-McLean model is more easy to use and the GB enrichment ratio is used to quantify GB segregation [8, 15].

2.5. Grain boundary precipitation

Precipitation can occur at GBs as well as within the grains. However, GB precipitation is favored, if nucleation is energetically less costly as within the grain, or if the diffusion at GBs is much higher and new nuclei can be formed faster due to faster migration. Furthermore, a strong segregation tendency of the solutes can favor GB precipitation as well [17]. Second phase precipitates can have a tremendous effect on the properties of the materials, e.g. the plastic deformation and recrystallization

behavior. This can be explained by the Zener drag effect [54, 55]. It is well known that precipitates can hinder the GB to migrate within the crystal. Since plastic deformation and recrystallization come along with GB migration, both are strongly affected if precipitates are present at the GBs. GB precipitation is a heterogeneous process and occurs if the total free enthalpy ΔG_T decreases with the formation of the particle [17]:

$$\Delta G_T = V \Delta G_V + \Sigma A_{a/b} \gamma_{a/b} - A_{a/a} \gamma_{a/a} \tag{2.11}$$

ΔG_V is the free enthalpy per unit volume, $A_{a/b}$ is the area of the interface of the precipitate and the matrix with its corresponding surface energy $\gamma_{a/b}$ and $A_{a/a}$ is the deleted GB area with its energy $\gamma_{a/a}$. Thus, the summation is the difference between the energy to create the new particle/matrix interface (with area A) and the energy gain from the destruction of the GB area A. If $\Delta G_V < 0$, than precipitation will occur.

The shape of the precipitates as well as the form of the interfaces a/b can be very different and depends on the GB properties (energy, atomic structure, extrinsic dislocations, GB plane inclination, etc.). The interface a/b can be coherent, semi-coherent and incoherent. Coherent interfaces are a perfect match of the two lattices, independent on the chemistry of the two phases. These special interfaces come along with a preferential orientation between matrix and precipitate. This relationship can lead to different shapes of the precipitates (i.e the particles form low energy facets), such as cubes, rectangles, etc. The form of precipitates (also the semi-coherent and incoherent ones) can be described by the Wulff construction. A detailed description of the different precipitates and the Wulff construction can be found in [17]. Semi-coherent interfaces are formed when there is a too large misfit between the lattice parameter so that misfit-dislocations are inserted into the boundary (similar to intrinsic dislocations in GBs). The energy of the phase boundary is then the sum of the coherent interface (pure chemical contribution) and the strain energies of the dislocations. Incoherent precipitates contain only interfaces with the matrix where the two lattices do not show any periodicity of planes across the interface, respectively. If there is a mixture of coherent and incoherent interfaces, it is called partly coherent. In this thesis, incoherent precipitates are of interest, as will be shown later in chapter 7 and 8. These precipitates have no orientation relation to the matrix and can be seen similar

as random GBs. Their shape is usually "elliptical" and is called allotriomorph.

3. Characterization Techniques

This chapter summarizes the basic principles of all employed experimental and simulation techniques in this thesis. Each technique will be briefly introduced, while detailed explanations are restricted to the important and most used techniques. The knowledge for section 3.3 was taken from [56–59] if not cited otherwise.

3.1. Scanning electron microscopy

In scanning electron microscopy (SEM) an image is formed by a small electron beam which is scanned across a specimen surface, as in STEM. The electrons interact with the sample and produce different signals, which can be detect with various detectors to collect information about the chemistry and topography. The electron source can be a tungsten filament, a LaB_6 crystal or a FEG. Each source generates electrons which are then accelerated typically to an energy of $1-30\,keV$. A Wehnelt cylinder collects the electrons and forms a beam crossover. An optical system consisting of electrostatic lenses then focuses the electron probe onto the specimen surface and scan coils are used to raster the specimen surface. The electrons interact with the surface in form of elastic and inelastic scattering generating secondary electrons (SE), back scattered electrons (BSE), Auger electrons and characteristic x-rays. These signals are detected individually and simultaneously with different detectors to gather information about the specimen. Secondary electrons have usually an energy up to $50\,eV$ and are usually generated close to the specimen surface. Back scattered electrons can exhibit an energy up to the initial electron energy and are sensitive to the Z number of the elements due to elastic scattering at the nucleus of the specimen atoms.

In the following the principle SEM image formation, electron back scatter diffraction and wavelength-dispersive spectroscopy will be introduced briefly. Literature for this whole section is [60].
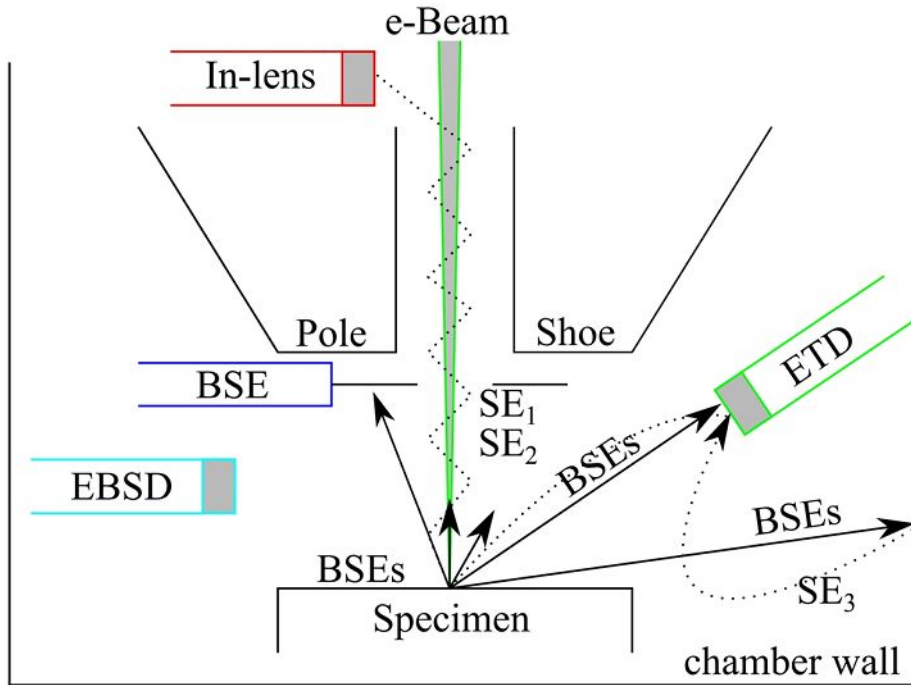
Fig. 3.1.: SEM chamber Setup: This figure depicts schematically the SEM chamber. The different detectors are colored and the primary electron beam is drawn in green/gray. The image was redrawn after [60].

3.1.1. Imaging

A SEM image is formed by collecting a specific signal for each beam position (each pixel in the image) for a specific time (the dwell time). A modern and well equipped SEM usually contains multiple detectors which can be used simultaneously. The most common detector is the Everhart-Thornley-Detector (ETD). It consists of a scintillator in a Faraday cage and is located inside the chamber close to the specimen, as shown in Fig. 3.1 in green. The scintillator converts the electrons into photons which are collected and amplified by a photomultiplier to generate a signal. Usually a small positive voltage is applied to the Faraday cage to attract the SE. However, some of the BSE also reach the ETD so that the final image under these conditions is always a mixture between the SE and BSE contrast. If the Faraday cage is negatively biased, the SE signal can be suppressed and a BSE image is formed. To suppress the BSE

component of the image, the detector can be placed inside the objective lens, a so-called in-lens detector (the red detector in Fig. 3.1). This detector works with the same principles as the ETD, but the detector is hidden inside the lens behind a small edge, so that BSE cannot reach the detector because of their high velocity. Thus an almost pure SE image can be formed. BSE images can be optimized by special BSE detectors which are placed directly between the specimen and the pole shoe, as shown in dark blue in Fig. 3.1. Usually they are round and have a whole in the middle where the primary electron beam and SEs passes the detector. Since most BSE have a direction back to the electron column, in this way the intensity can be increased compared to a negatively charged ETD detector which is located inside the chamber and not as close to the column as the BSE detector. Literature for this subsection is [60].

3.1.2. Electron backscatter diffraction

Electron backscatter diffraction (EBSD) is a characterization technique for crystalline materials. It can determine crystal structures, different phases, grain orientations and dislocation densities with SEM resolution. The incoming electrons undergo inelastic scattering events with the specimen atoms and can be seen as a divergent electron source in all direction. These scattered electrons undergo afterwards elastic scattering events and if the Bragg condition is fulfilled, the scattered electrons will interfere constructively and form an EBSD pattern, also called Kikuchi pattern. These pattern are recorded for each pixel in a SEM image and a full EBSD map is formed. The EBSD pattern are recorded with a special detector which can be inserted into the chamber with an angle of 90° with respect to the electron beam (see Fig. 3.1). The detector contains a phosphor screen, which converts the electrons into photons, and a CCD, CMOS or TV camera, which films the diffraction pattern in each pixel. In order to align the back scattered electrons better to the detector, the sample is tilted to 70° towards the detector. A mathematical transformation, called Hough transformations, determines all the positions and angles of the Kikuchi lines and poles, which are representative for the angles between the lattice planes. By comparing the obtained pattern with a database the crystal phase and orientation can be determined. This is done for each electron beam position of the SEM image so that an phase/orientation map can

be created. For more details see [61]

3.1.3. Wavelength-dispersive X-ray spectroscopy

Wavelength-dispersive X-ray spectroscopy (WDXS) is a famous technique in SEM to accurately determine the composition of the investigated material with μm lateral resolution. The generated X-rays from the SEM are characteristic for the elements of the investigated specimen. In contrast to EDXS, WDXS does not collect the energies of the incoming X-rays, but separates the X-rays by diffracting them through single crystals and collecting only one wavelength at a time. While EDXS provides a good qualitative overview of the chemistry, WDXS is used as a quantitative analysis due to its much better sensitivity and resolution. Usually WDXS measurements are performed in dedicated instruments, called electron micro probe analyzer (EPMA), because it requires a powerful beam to penetrate deep into the samples in order to create many X-rays. Therefore, a large beam diameter and high beam current is necessary. Since this influences the imaging resolution badly, a WDXS system is found rarely in dedicated SEM. A detailed overview on the working principle of WDXS, the used single crystals as diffractors and the quantitative chemical sensitivity can be found in [60].

3.2. Focused ion beam microscope

A focused ion beam (FIB) workstation is in principle similar to an SEM, but uses ions instead of electrons. The main application of FIB in this thesis is the defined removal of material with nanometer precision for TEM lamella preparation. An ion beam is created using a liquid metal ion source (LMIS), a tungsten needle with a tip diameter of $\sim 2-5\mu m$ and an extractor electrode. The LMIS should have ideally a low melting point and vapor pressure and a good wetting behavior to tungsten. In many FIB systems Gallium (Ga) is used as an ion source. The Ga reservoir is connected to a tungsten tip. When the Ga reservoir is heated, the Ga wets the tungsten tip and forms a uniform Ga film on the needle. By applying a voltage to the extraction electrode, the high electric field at the tip forms a small ($\sim 2-5\,nm$) Ga point source with a

Taylor cone shape. If the surface tension and the electric field are in equilibrium, Ga ions are extracted from the tip and accelerated by a high voltage (typically between $3-30\,keV$). A condenser lens is used to form the ion probe, an objective lens focuses the ion probe onto the specimen surface and scan coils raster the beam across defined patterns. The current and size of the ion probe can be controlled with different apertures of varying diameter. Typical beam currents are in the range between a few pA to several nA. The Ga ions interact with the specimen via elastic and inelastic scattering processes, like the electrons in the SEM do. Due to the higher mass of the ions and depending on the beam current, the material can be removed either in large volumes (high current) or the material can be gently polished (low current) by sputtering processes. The sputter rate depends strongly on the beam current, the accelerating voltage, the dose and the material itself. Also the ion beam generates SE and secondary ions (SI), which can be used for imaging. In this thesis, however, a dual beam SEM-FIB was used, where ion and electron beams are coupled on one spot. So imaging with the electron beam is possible during milling with the ion beam. More detailed descriptions of FIB can be found in [62]

3.3. Transmission electron microscopy

In TEM, thin, electron transparent specimens (usually $\leq 100\,nm$) are illuminated by an high energetic electron beam. The beam is generated by an electron source, which is in modern machines often a field emission gun (FEG), but also LaB_6 crystals and tungsten filaments are common in older instruments. After the electrons are generated they are accelerated with a high electric potential, which is commonly in the range of $80-300\,kV$. As a condenser system, electro magnetic lenses are used to focus either a parallel electron beam (TEM) or a small electron probe (STEM) onto the specimen. The electrons pass through the specimen either without interaction or they undergo elastic or inelastic scattering events. The electrons are then focused by an objective lens and projected onto a viewing screen or an electron detector (usually a charge coupled device (CCD)) by an intermediate and projector lens. Due to the variable (weak and very strong) objective lens and its very small focal length, small and

high magnifications, such as $\sim 10^3 - 10^6$, can be achieved. The strength of the inter-mediate lens, also known as diffraction lens, can be tuned in order to view the image in different magnifications or to project a diffraction pattern on the viewing screen / CCD. In contrast to optical light microscopes, the resolution of a TEM is not limited by the wave length (Abbe diffraction limit [63]), but by the aberrations of the (electron) optics. While first order astigmatism and coma can be compensated fairly easy by stigmators (usually quadrupoles or hexapoles), higher order aberrations and other aberrations like spherical aberration are corrected using a special, complex aberration corrector, which was developed recently and improved the image resolution and the analytical methods enormously [64, 65]. The position of this corrector determines if the microscope is dedicated for HRTEM or STEM. In HRTEM, the corrector compensates the aberrations of the objective lens and is placed after the specimen and the objective lens. In STEM, however, the corrector compensates the aberrations of the condenser system in order to minimize the electron probe and is located in front of the specimen. In the next subsections, a quick description on conventional TEM (CTEM) and HRTEM is given, followed by a more detailed treatment on aberration correction and STEM, since this is the main technique in this thesis. The literature for this section can be found in [56, 58, 59, 66–68]

3.3.1. Conventional transmission electron microscopy

Independent on the materials structure and composition, it is always helpful to first look at the diffraction pattern of a specimen, since it reveals how the material interacts with the electrons. When the primary electrons pass through the specimen they can either undergo elastic and inelastic scattering processes or they pass through without any scattering. Inelastic scattering is the interaction of primary electrons with shell electrons of the specimen and causes almost no deviation from the original path (strong forward scattering). So these electrons form together with the unscattered electrons the so called direct beam. This beam, which is illustrated as a gray ray in Fig. 3.2, travels along the optical axis and is not affected by the lens system. Elastic scattering is defined as the interaction of the primary electrons with the Coulomb potential of a nucleus and leads to a larger scattering angle from its original path (up

to 200 $mrad$ and even higher) and is illustrated by the colored rays in Fig. 3.2. In a crystalline material the elastic scattering occurs at well ordered specimen atoms with a specific periodicity. If a single crystalline specimen is oriented with a zone axis parallel to the electron beam, the electrons fulfill the Bragg condition for many lattice planes and constructive interference occurs, which is described by the Bragg equation:

$$2 \cdot d_{hkl} \cdot sin(\Theta_{Bragg}) = n \cdot \lambda \tag{3.1}$$

where d_{hkl} is the lattice spacing between the planes hkl, Θ_{Bragg} is the Bragg angle and λ is the wave length of the electrons. Thus, a diffraction pattern is formed in the TEM as follows (also illustrated in Fig. 3.2 (a)): The initial beams are colored in red and yellow for the off axis beams (gray for the beam along the optical axis). The beams interact with the specimen and diffracted and un-diffracted electrons pass the objective lens and are focused to the back focal plane, where the first diffraction pattern is formed (these are marked by colored circles in Fig. 3.2 (a)). With the selected area diffraction (SAD) aperture , which is located in the first image plane, a confined area can be selected to create the diffraction pattern. The intermediate / diffraction lens must be switched in diffraction mode in order to view the diffraction pattern on the screen/CCD. The pattern contains information about the crystal structure and orientation and can be used to determine lattice parameters. In the case of GBs, the misorientation and GB plane normal $\vec{n}$ can be determined by taking a diffraction pattern of both grains at the same time, provided that the GB plane is parallel aligned along the electron beam direction.

For imaging, an objective aperture, located in the back focal plane of the objective lens, is used to select only specific electrons from the diffraction pattern to form an image in the image plane of the lens. The resulting images are called bright field (BF) or dark field (DF) images. A BF image is formed when only the direct beam is collected with the objective aperture and all elastically scattered electrons are blocked. Regions that occur bright in the image can be interpreted as low scattering regions, whereas dark regions scatter the electrons strongly due to Z-contrast, different specimen thickness, higher atomic density or these regions fulfill a certain diffraction condition. Thus, a BF image can be a mixture between mass-thickness and diffraction

(a)

optical axis

specimen

objective lens
objective aperture

····· bfp

1st diffraction pattern in bfp

SAD aperture
intermediate /diffraction lens

intermediate diffraction pattern

projection lens

Final diffraction pattern

(b)

optical axis

specimen

objective lens

selecting one spot

bfp ·····

1st intermediate image

2nd intermediate image

Final (bright field) Image
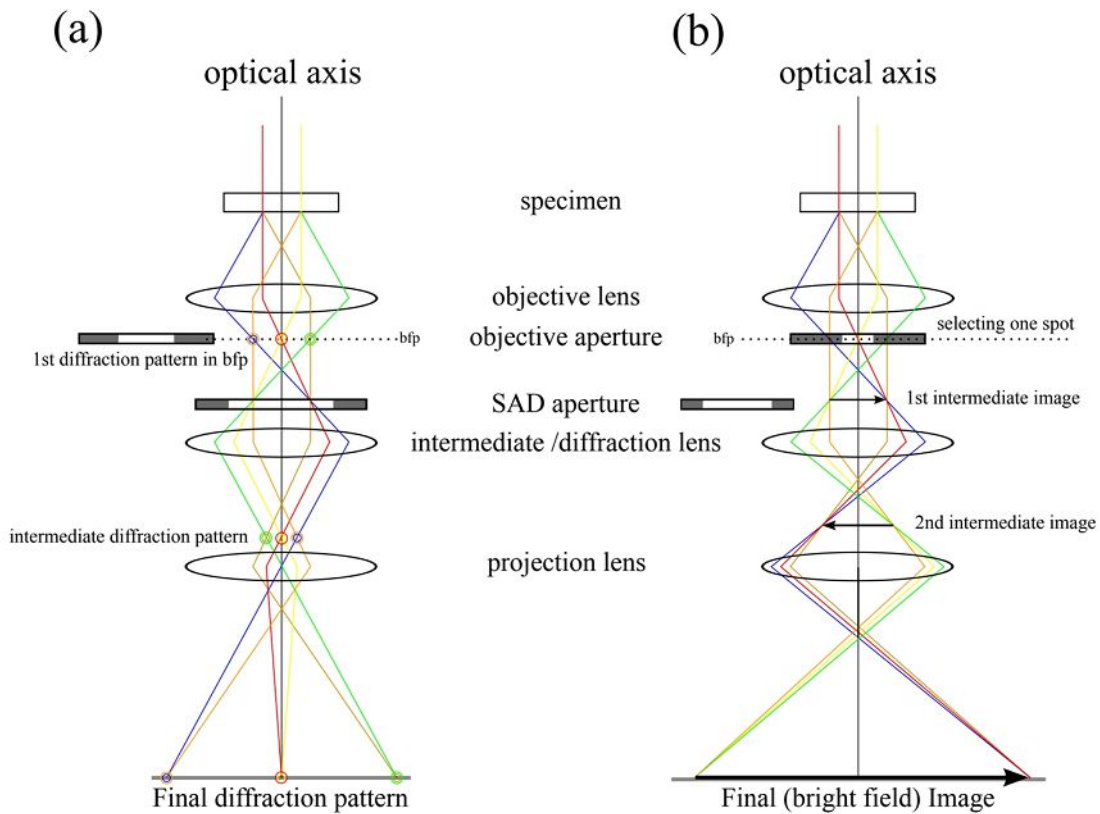
Fig. 3.2.: Electron path inside the TEM: (a) illustrates the electron path for building a diffraction pattern. (b) By changing the strength of the diffraction lens, instead of the diffraction pattern, the first intermediate image is transferred to the camera. The image was redrawn after [57]

contrast. In DF images, the objective is centered around a specific diffraction spot hkl and the image is formed only by electrons scattered at the corresponding lattice planes d_{hkl} in a specific direction. All other electrons are blocked by the aperture. The image typically appears dark and features corresponding to the selected scattering centers, such as small grains or dislocations appear bright. Thus, a DF image is dominated by diffraction contrast.

3.3.2. High-resolution transmission electron microscopy

In high resolution TEM no objective aperture or large apertures capturing many diffracted spots are used and the image contrast is formed by interference of all/many diffracted electron waves passing the specimen. To understand the contrast formation in this technique, it is advantageous to see electrons as coherent waves instead of particles. During interaction of the electron wave with the specimen, the amplitude and phase

of the electron wave is modulated. The phase modulation contains information of the atomic structure of the specimen. However, the phase modulation cannot be measured directly so that the microscope aberrations are used to transform the arising phase contrast into amplitude contrast, which then can be measured. How this contrast is transferred inside the microscope by its lenses is described by the contrast transfer function:

$$CTF(\vec{q}) = A(\vec{q})B(\vec{q})E(\vec{q}) \tag{3.2}$$

where $\vec{q}$ is the spatial frequency and $A(\vec{q})$ is the aperture function, which is 1 for all spatial frequencies inside and 0 for all spatial frequencies outside the objective aperture. $B(\vec{q})$ is the aberration function and depends mainly on the defocus Δf of the objective lens and the spherical aberration coefficient C_s of the microscope and is defined as:

$$B(\vec{q}) = sin\left(\frac{\pi}{2}\left(C_s \cdot \lambda^3 \cdot q^4 - 2 \cdot \Delta f \cdot \lambda \cdot q^2\right)\right) \tag{3.3}$$

The CTF is only valid in the weak phase object approximation (see literate for more details), which is the case for only very thin specimen thicknesses (for lighter elements a few nanometers). This aberration function describes an oscillation of the contrast transfer as a function of the spacial frequencies $q(\vec{r})$. Especially at high spacial frequencies the contrast transfer oscillates, which means that the contrast transfer inverts and the image becomes more difficult to interpret. Two examples are shown in Fig. 3.3 (a) and (b) for an uncorrected and a corrected microscope, respectively. The point where the function crosses the first time the x-axis is called the point resolution, because to this point the contrast is directly interpretable since no inversion took place so far. As is shown in Fig. 3.3 (a) and (b), the correction of the spherical aberration gives a great improvement. The last term in the PSF $E(\vec{q})$ is called the envelope function and depends on the initial electron energy, the energy resolution, the wavelength and on the chromatic aberration coefficient C_c. It describes an exponentially decrease of the intensity mainly due to chromatic aberration of the optical system and is defined as:

$$E(\vec{q}) = e^{-\pi^2 \cdot C_c^2 \cdot \left(\frac{\Delta E}{E}\right)^2 \lambda^2 \cdot q^4} \tag{3.4}$$

with E being the electrons energy and ΔE the energy resolution.
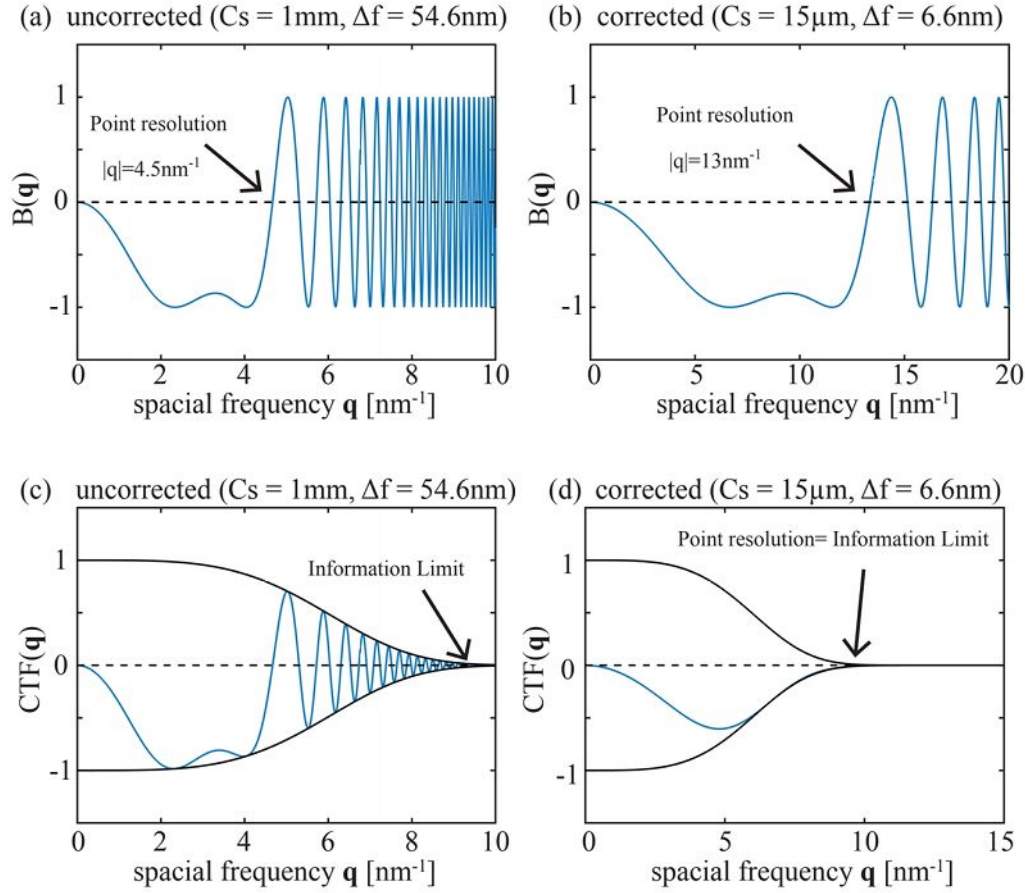
Fig. 3.3.: Contrast Transfer Functions: (a) Aberration function representing an uncorrected TEM with a spherical aberration coefficient of $C_s = 1\,mm$ under Scherzer defocus $\Delta f = 54.6nm$ conditions. (b) shows the aberration function for a corrected TEM using $C_s = 15\,\mu m$ and $\Delta f = 6.6nm$). The total CTF is depicted in (c) and (d) for an uncorrected and a corrected TEM including the envelope function.

Insertion of all parts in $CTF(\vec{q})$ yields:

$$CTF(\vec{q}) = A(\vec{q})\,sin\left(\frac{\pi}{2}\left(C_s \cdot \lambda^3 \cdot q^4 - 2 \cdot \Delta f \cdot \lambda \cdot q^2\right)\right) \cdot e^{-\pi^2 \cdot C_c^2 \cdot \left(\frac{\Delta E}{E}\right)^2 \lambda^2 \cdot q^4} \qquad (3.5)$$

It describes how the contrast is transferred by the microscope and its aberrations to the image with respect to the spatial frequencies. Fig. 3.3 (c) and (d) shows the final CTF (using both $B(\vec{q})$ and $E(\vec{q})$). $E(\vec{q})$ leads to a dampening of the aberration function $B(\vec{q})$. The point, where the function goes to zero is called the information limit. In an uncorrected microscope the contrast still oscillates so that usually the final images need to be compared with image simulations in order to understand the contrast in the image. In a corrected microscope, however, the CTF is fully damped before the

contrast inverses, which means that the point resolution is identical to the information limit. Therefore, the interpretation of HRTEM images is usually straight forward by carefully adjusting the microscope aberrations with a corrector.

3.3.3. Scanning transmission electron microscopy

In STEM a small electron probe is focused onto the specimen and then scanned across it, similar to the SEM. This is achieved by the TEM condenser lens system, which acts in STEM therefore as a probe-forming objective lens. In each pixel the electrons interact with the specimen by elastic and inelastic scattering events and the image can be formed by detecting only specific electrons using annular detectors. The most used image in STEM is the high angle annular dark field (HAADF) image, which is also known as Z-contrast images. The image is formed by an annular detector, which collects only electrons, which have scattered to high angles. The detector has therefore a similar function as the objective aperture in CTEM. Under HAADF conditions, each atom in the specimen can be seen as an independent scattering center, which means that there is no phase relationship anymore between the scattering event of an electron with different atoms. Thus, the atoms are incoherent sources. If the electron probe is scanned across the atoms, the image intensity in each pixel will correspond to a fraction of the electron probe intensity, which was scattered by the scattering sources (the atoms). In a mathematical sense this is described by the following convolutions, which represents the definition of incoherent imaging:

$$I(\vec{r}) = O(\vec{r}) \otimes \mid P(\vec{r}) \mid^2 \tag{3.6}$$

where $O(\vec{r})$ is the object function, which is mainly defined by the scattering cross section, and $\mid P(\vec{r}) \mid^2$ is the intensity of the electron probe. Therefore, the HAADF images represent the atoms, which are blurred out be the shape and size of the electron probe. If the probe is much bigger than the atomic distances however, atomic resolution cannot be reached respectively. This is one main feature of STEM: Spatial resolution is determined by the size and shape of the probe only and not by an image-forming lens. Since different atoms have different scattering cross sections, they can
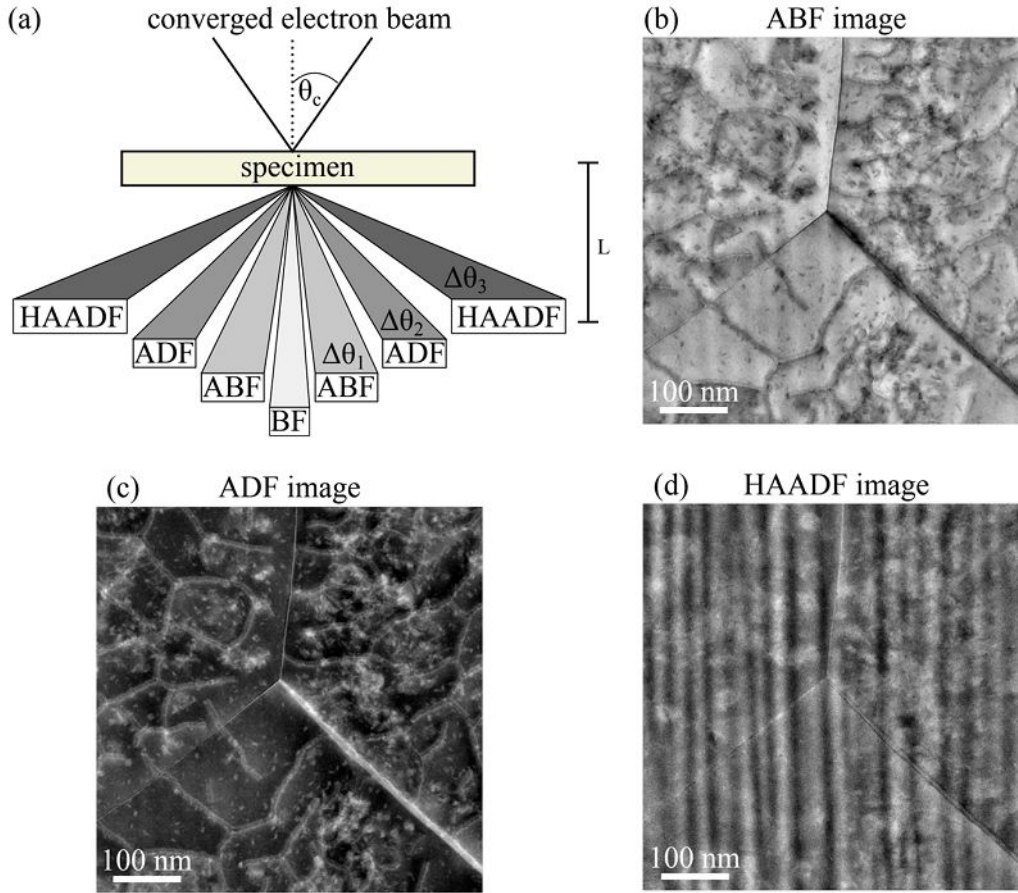
Fig. 3.4.: Detector setup in STEM: (a) working principle of STEM image formation with a multiple detector setup, where θ_c means the semi-convergence angle, $\Delta\theta_i$ the collection angles ranges and L the camera length. (b) -(d) show an example of a ABF, ADF and HAADF image at an identical specimen position to compare the contrast

be easily distinguished in HAADF images. For incoherent scattering the differential cross section is defined as:

$$\frac{d\sigma}{d\Omega} = \left(\frac{1}{4\pi \cdot \epsilon} \cdot \frac{Z \cdot e^2}{4 \cdot E_0} \right)^2 \cdot \frac{1}{\sin^4 \frac{\Theta}{2}} \tag{3.7}$$

ϵ is the dielectric constant, Z the atomic number of the scattering nucleus, E_0 the electron energy, Ω the solid angle and Θ the scattering angle. The differential cross section, and thus, the angular distribution of the scattered electrons depends on the initial beam energy and is proportional to the square of the atomic number Z of the specimen elements. Therefore, the contrast in HAADF images is also called Z-contrast. The angular distribution covers a wide range from $0\,mrad$ up to several $100\,mrad$. Since the specimen contains more than one atom, the scattering depends

also strongly on the thickness and density of the specimen. HAADF images are typ-ically recorded with electrons scattered to angles between $73\,mrad$ and $200\,mrad$ (this are the values used in this thesis). These angles are called collection angles. At lower collection angles, other contrast mechanism come into play, such as diffraction, strain and phase contrast. Using multiple detectors, different images with different contrast mechanism can be formed, as is shown in Fig. 3.4 (a). The other detectors are called BF, annular BF (ABF) and annular DF detector. Each detector forms an im-age by collecting the electrons only in a certain angular range $\Delta\theta_i$. One example for ABF, ADF and HAADF images is shown in Fig. 3.4 (b) - (d). It nicely shows that lower magnification ABF and ADF images contain much diffraction contrast by showing the dislocation network and the three GBs and have a lower sensitivity to the specimen thickness,. In the HAADF image, however, the dislocations are barely visible since the collection angle is too high. Mainly vertical bright and dark lines can be seen, which arise from a thickness difference due to curtaining in the focused ion beam machin-ing process. These thickness variation are invisible in the ABF and ADF signal. The collection angles can be easily varied by the camera length L (see Fig. 3.4 (a)) so that the contrast mechanism can be controlled carefully.

As already mentioned, the magnification in STEM does not depend on lenses, but on the scan region dimensions (as in SEM). The resolution, however, is determined by the size and shape of the electron probe, which is controlled by the objective aperture and its aberrations. Therefore, it is desirable to create the smallest probe size possible with a Gaussian intensity shape. The probe size depends mainly on the electron gun source size, the diffraction limit from the probe-forming aperture and the aberrations of the probe-forming lens. The diffraction limit can be decreased by increasing the aperture size, which directly scales with the convergence angle (semi convergence angle θ_c is depicted in Fig. 3.4 (a)). Therefore, the higher the convergence angle, the better the resolution. However, the higher the electrons deviate from the optical axis, the stronger are the aberrations of the lenses, namely astigmatism, coma and spherical aberration. The aberration function χ is defined as (up to beginning of 4th

order) [68]:

$$
\begin{aligned}
\chi\left(\theta_{(x)},\theta_{(y)}\right) = \frac{2\pi}{\lambda}\Bigg[&\frac{1}{2}C_{10}\theta^2 + \frac{1}{2}C_{12a}\left(\theta_{(x)}^2 - \theta_{(y)}^2\right) + C_{12b}\theta_{(x)}\theta_{(y)} + \\
&\frac{1}{3}C_{21a}\theta_{(x)}\theta^2 + \frac{1}{3}C_{21b}\theta_{(y)}\theta^2 + \frac{1}{3}C_{23a}\theta_{(x)}\left(\theta_{(x)}^2 - 3\theta_{(y)}^2\right) + \\
&\frac{1}{3}C_{23b}\theta_{(y)}\left(\theta_{(y)}^2 - 3\theta_{(x)}^2\right) + \frac{1}{4}C_{30}\theta^4 + \frac{1}{4}C_{32a}\left(\theta_{(x)}^4 - \theta_{(y)}^4\right) + \\
&\frac{1}{2}C_{32b}\theta_{(x)}\theta_{(y)}\theta^2 + \frac{1}{4}C_{34a}\left(\theta_{(x)}^4 - 6\theta_{(x)}^2\theta_{(y)}^2 + \theta_{(y)}^4\right) + \\
&C_{34b}\left(\theta_{(x)}\theta_{(y)}^3 - \theta_{(x)}^3\theta_{(y)}\right) + C_{41a}\left(\theta_{(x)}^4\theta_{(y)} + 2\theta_{(x)}^2\theta_{(y)}^3 + \theta_{(y)}^5\right) + \\
&C_{41b}\left(\theta_{(x)}\theta_{(x)}^4 + 2\theta_{(x)}^3\theta_{(y)}^2 + \theta_{(x)}^5 + ...\right)\Bigg]
\end{aligned}
\tag{3.8}
$$

where $\theta_{(i)}$ are the angles in x and y direction and C_{ij} are the aberration coefficients. In particular defocus C_{10}, twofold astigmatism C_{12}, coma C_{21}, third order spherical aberration C_{30}, third order astigmatism C_{23} and so on. All these aberrations scale with the angle so that in the end an optimum convergence angle must be found for the best balance between diffraction limit and aberration to get the best resolution. The effect of aberrations on the beam shape have been nicely visualized in the book of Kirkland et al. and are shown in Fig. 3.5 [68].

Fortunate, aberration correctors have been developed recently, which can control and minimize the given aberration. Different types of correctors exist, but all of them consist of complex lens combinations (such as quadrupole, hexapole and octopole lenses) in order to correct the different aberrations. This enables to use large semi-convergence angles such as $23.8\,mrad$ (as used in this thesis) or even larger (compared to angles well below $10\,mrad$ in uncorrected STEM machines). This pushes the resolution of STEM at $300\,kV$ in the sub-angstrom regime and atomic resolution is easily reached in HAADF imaging nowadays [65]. Furthermore, as we will see in the next section, the aberration correction results also in large improvements in the analytical techniques concerning spatial resolution and chemical sensitivity.
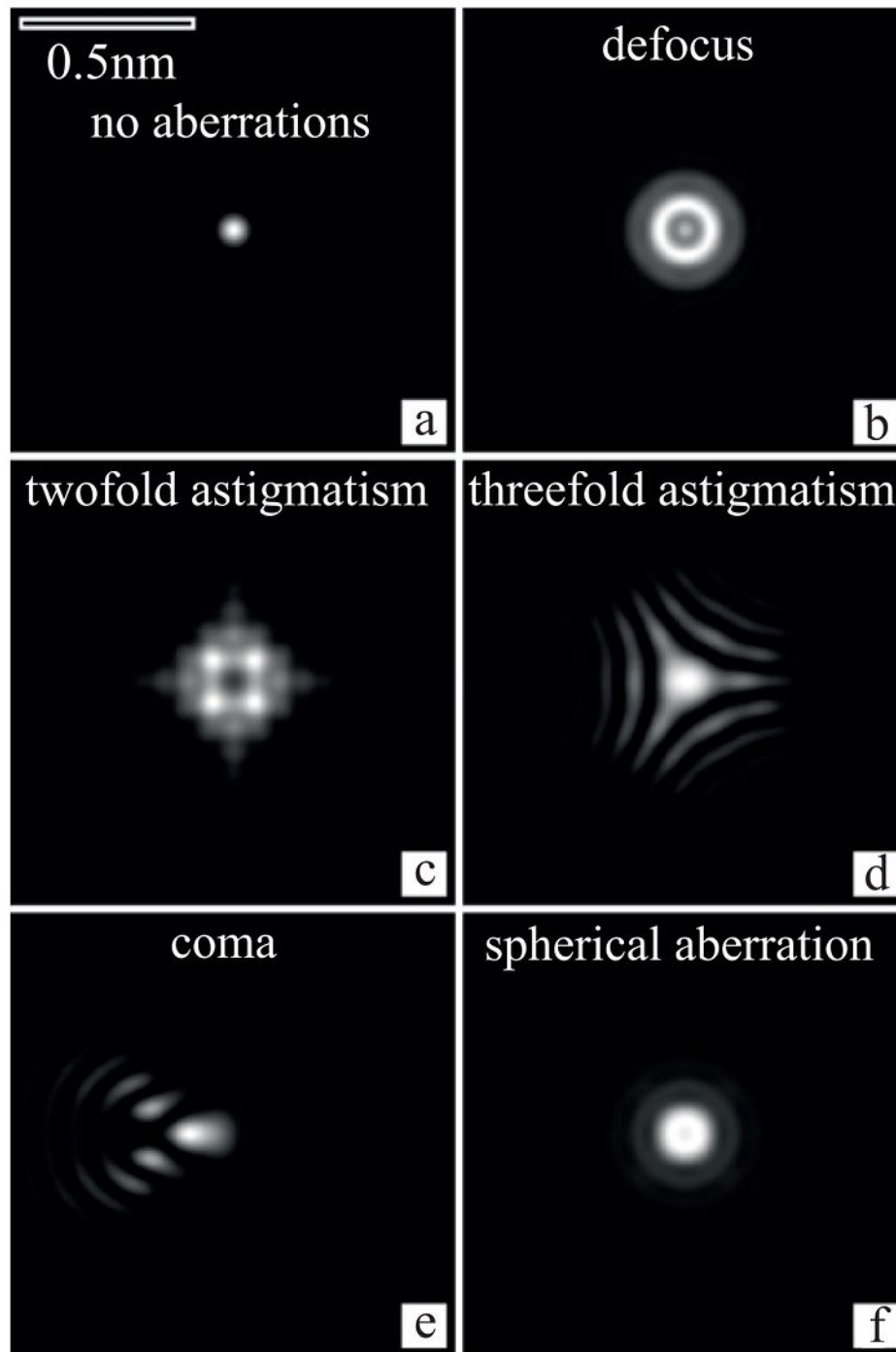
Fig. 3.5.: Effect of aberrations on the electron probe: (a-f) show the effects on the electron probe shape of different aberrations. For more details see the original images in [68].

3.4. Spectroscopy in the TEM

So far, only elastic scattering was discussed in order to understand the image formation in TEM and STEM. But also inelastic scattering processes, which are defined as

electron-electron interactions, play an important role in TEM. During an inelastic collision, the incident electron transfers energy to a shell electron of an atom, which will leave the atom and ionizes the atom into an higher energy state. The atom can stay in this unstable state only for short times (typically some picoseconds) and fills then the inner electron hole with an electron from an outer shell. During this transition, the electron has to emit the energy difference between the two energy levels in form of a photon (more precise X-rays). These generated X-rays are characteristic for each element and can be used for a qualitative and quantitative chemical analysis of the TEM specimen. In Fig. 3.6 a sketch of possible interactions between an incident electron and an atom is depicted. The initial electron is scattered forward (very low angles) and contributes to image formation (a diffuse background) or is used in an energy filter for further analysis.
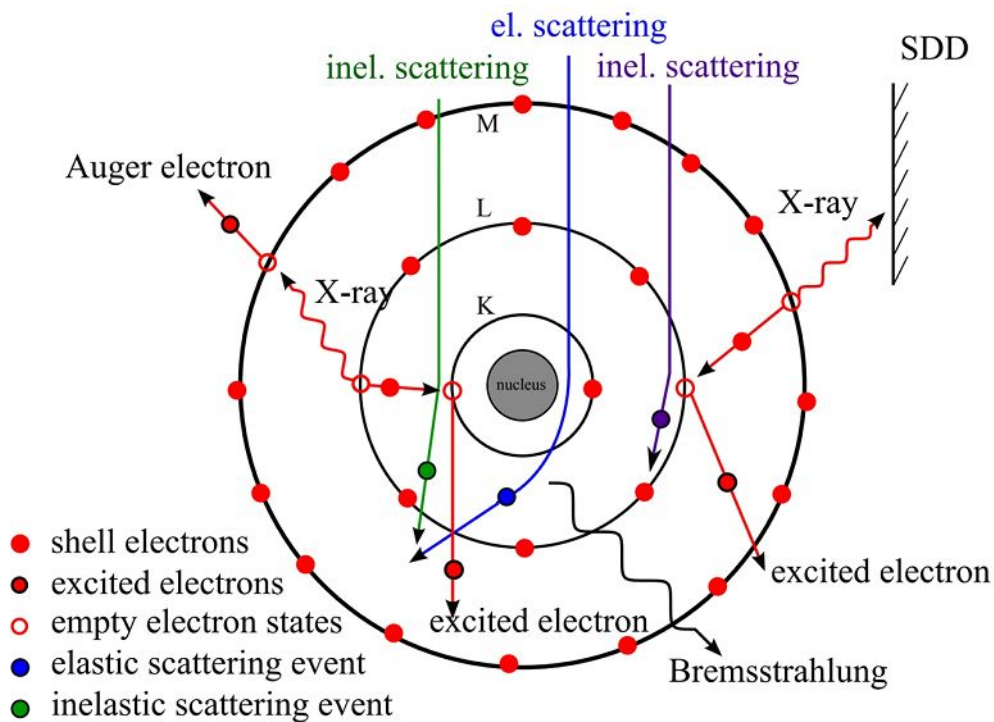
Fig. 3.6.: Principle of EDXS: (a) Sketch of the interaction of incident beam electrons with the nucleus and electrons of one atom. The blue path shows elastic scattering at the nucleus, resulting in Bremsstrahlung. The green and purple electrons show two inelastic scattering events with two different results. The purple event shows the ionization of an electron followed by an emission of an X-Ray photon. In the green inelastic event the resulting X-Ray excites another electron, which leaves the atom and is called Auger electron. The image was drawn due to inspiration from ref.[60].

However, inelastic scattering also has a mayor drawback, since it damages the speci-

men. A detailed analysis of beam damage induced by inelastic scattering can be found in [69]. In TEM there are two common ways to use inelastic scattering for elemental analysis. One technique is to directly detect the generated X-rays with a detector, referred to as energy dispersive X-ray spectroscopy (EDXS). This will be part of the next subsection. The second common technique is called electron energy loss spectroscopy (EELS). As the name already indicates, the electrons, which lost energy in an inelastic collision, are analyzed using a post column energy spectrometer and/or filter.

3.4.1. Energy dispersive X-ray spectroscopy

The characteristic X-rays generated by inelastic scattering processes are detected commonly by semiconductor detectors such as a Lithium doped Silicon detector, or more recently by silicon drift detectors. Even though inelastically scattered electrons are strongly forward scattered, the generated X-rays are emitted in all directions inside the microscope and it is impossible to detect them all. Therefore, large detector areas are needed to collect as many X-rays as possible to get a good efficiency and signal to noise ratio. However, the specimen is located between the two pole pieces of the objective lens, and therefore the space for large area detectors is very limited. One ways to improve the efficiency in modern microscopes, is to used several small detectors (but as big as the pole piece allows) to increase the total solid angle and thus the X-ray counts. With the use of an aberration corrector, the pole piece gap is bigger and allows for larger collection angles using larger detector areas. Nevertheless, the efficiency of EDXS is still low, since still many X-rays do not reach the detector, but hit the specimen holder (which also have strongly improved lately), or the microscope interior.

Each collected X-ray can be assigned to a specific electron transition of a specific element. A K_α or K_β X-ray is generated, if an electron from the K shell is excited and then filled by an electron from the L or the M shell (see sketch in Fig. 3.6). In the same way L_α and L_β X-rays are generated, except that an L shell electron is excited from the initial electron and is then filled by the M or N shell. The Z number of the ele-
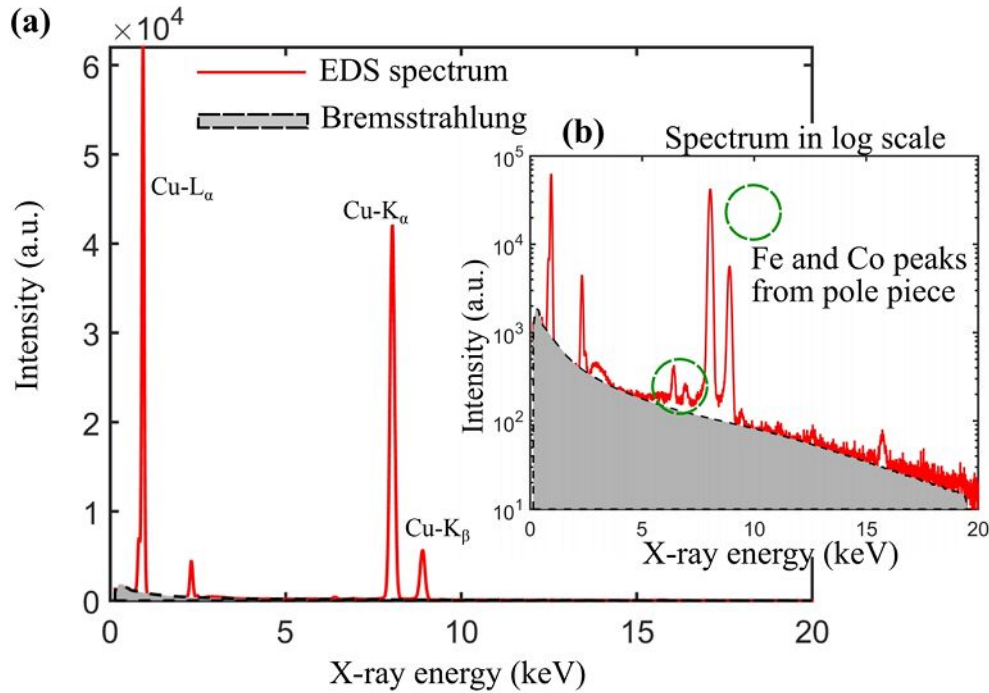
Fig. 3.7.: Typical EDXS spectrum: (a) Typical EDXS spectrum (red) showing some characteristic peaks (here Cu and S) overlaid with the Bremsstrahlung spectrum (gray). (b) shows the same spectrum in a logarithmic scale, which better visualizes the Bremsstrahlung. Additional small peaks arise (Fe and Co) resulting from the microscope's interior.

ment defines how many different transitions exist. For example, the oxygen atom has only occupied states in the K and L shell so that only K_α X-rays can be created. The higher the atomic number Z, the more transition can occur. The X-rays are detected nowadays mostly by silicon drift detectors. In the sensor region (fabricated from pure silicon), the X-rays create electron hole pairs due to ionization processes. The resulting charge of the generated electrons is proportional to the energy of the individual incoming X-ray. The electrons then drift along rings with special field gradients to the anode, while to holes drift to the cathode. The charge at the anode is then converted to a voltage using a field effect transistor and is preamplified. The charge of an X-ray is seen as a voltage step on a linear increasing ramp. The pulse processor converts these voltage steps into a signal pulse, where its height corresponds to the energy of each X-ray and assigns it to the corresponding channel in a spectrum. For more detail see ref [58]. After the collection of all X-rays, a spectrum can be formed where the characteristic X-ray energy is displayed versus the intensity (or X-ray counts), as is depicted in Fig. 3.7 (a) and in (b) with a logarithmic intensity scale. However, due to

stray or backscattered electrons, also X-rays from the pole piece, the specimen holder or the support grid can cause a signal to the detector and have to be taken carefully into account. An example of that can be seen in Fig. 3.7 (b), where Fe and Co peaks (from the pole piece) can be seen in the X-ray spectrum. Another important feature is a continuous background which overlays the characteristic signals from the elements and can be identified as the gray area in Fig. 3.7 (a) and (b). This background arises from an electromagnetic radiation called Bremsstrahlung. When charged particles are decelerated by an external field, they lose energy and irradiate photons. This process is exactly what happens during elastic scattering of the incident electrons at the nucleus, which is schematically illustrated in Fig. 3.6 (a) with the blue electron path. So a continuous background is always detected by the X-ray detector. Luckily, this background can be subtracted easily after the measurement.

EDXS can be used in TEM- and STEM-mode (STEM-EDXS). However, it is more common to use it in STEM because then an EDXS spectrum is collected in each pixel of the STEM image and a whole EDXS elemental maps of the specimen can be collected. With the improvement of the TEM and the development of aberration correctors, elemental maps with atomic resolution can be obtained nowadays.

After the measurement, the direct result is a qualitative EDXS spectrum or, in case of STEM-EDXS, a qualitative STEM-EDXS map of the scanned region, containing a EDXS spectrum in each pixel of the map. But there are also possibilities to obtain a quantitative estimation of the concentration ratio of the present elements, which means to convert the number of X-rays of element A (N_A) to a concentration of element A (n_A). Many decades ago, Raimond Castaing proposed an approximation for this conversion:

$$\frac{n_A}{n_{A,standard}} = K \cdot \frac{N_A}{N_{A,standard}} \tag{3.9}$$

where $n_{A,standard}$ is the concentration and $N_{A,standard}$ the number of X-rays from a well known, characterized standard sample. It takes into account the ionization cross section of an element (depends on the atomic number and the type of the inner shell) and the fluorescence yield (gives the probability of X-ray generation versus Auger electron emission). The fluorescence yield increases usually with increasing atomic number so that heavier atoms tend to generate X-rays while in lighter atoms

the Auger process becomes more probable. Furthermore, absorption of X-rays inside the specimen usually contributes to the K factor. The K-factor for each element is recorded from standard samples with well known concentrations. In thin TEM specimen, however, the absorption and fluorescence contribution can be neglected (for very thin specimen) and Cliff and Lorimer showed that EDXS quantification inside the TEM can be done without any standards, since the K-factor depends (approximately) only on the atomic number of the elements [70]. The Cliff-Lorimer equation takes into account only the intensity ratios of the measured elements and a corresponding K_{AB} factor:

$$\frac{n_A}{n_B} = K_{AB} \cdot \frac{N_A}{N_B} \tag{3.10}$$

This equation can be easily extended to more than two elements, by taking into account the different intensity $I_{i,j}$ (or counts $N_{i,j}$) ratios of each element and the corresponding $K_{i,j}$-factors (with i, j being the different elements in the specimen.).

As mentioned in the STEM section, aberration correction gives a huge improvement in spatial resolution and increases the detection limit. The spatial resolution in X-ray analysis is limit by beam broadening due to the specimen. Therefore, it strongly depends on the specimen thickness. This was investigated by Watanabe et. al in [65] and is shown in Fig. 3.8(a) for Cu. The best spatial STEM-EDXS resolution in an uncorrected microscope is larger than $1\,nm$ even for specimen thicknesses of only a few nm. Due to aberration correction, this spatial resolution is already reached for thicknesses of $40\,nm$. If the thickness is lower than $20\,nm$, they found that the spatial resolution reached atomic distances. The detection limit also improves strongly with aberration correction and is shown in Fig. 3.8(b). The horizontal, dashed line represents the detection limit. everything below that line cannot be resolved. It shows that for thin specimen thicknesses, single Mn atom detection is possible in a Cu-0.12$wt.$% Mn alloy. Therefore, the specimen thickness and the probe size are the crucial parameter for atomically resolved STEM-EDXS.
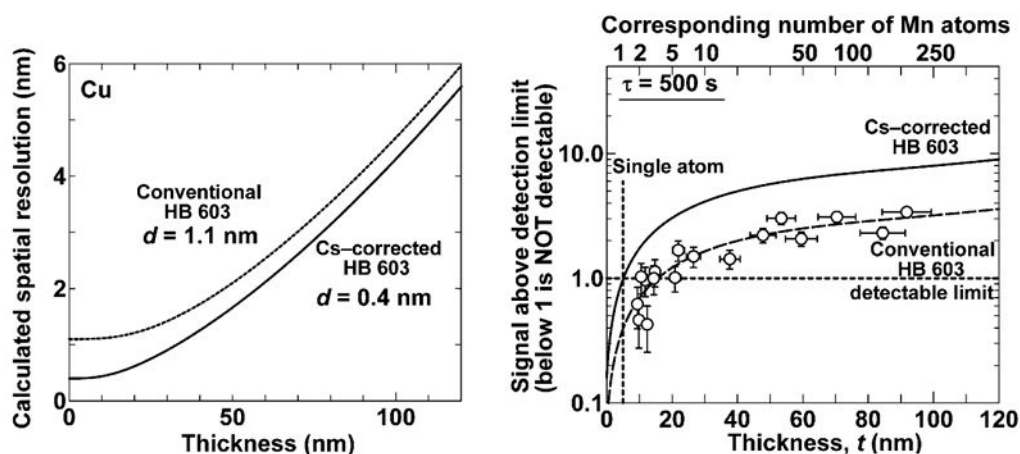
Fig. 3.8.: Improvement of EDXS by aberration correction: (a) Simulation of the spatial resolution of X-ray analysis as a function of the specimen thickness of an uncorrected and corrected microscope. (b) Detection limit of Mn atoms in a Cu-$0.12 wt.$% Mn alloy as a function of the specimen thickness for an uncorrected and corrected microscope. The plots are taken from [65].

3.4.2. Electron energy loss spectroscopy

In EELS, forward scattered electrons with different energies are transferred to a spectrometer after interacting inelastically with the TEM specimen, as is schematically shown in Fig. 3.9 (a). The blue ray represents electrons without energy loss, the green with loss and the red with high energy loss. How many electrons enter the spectrometer, which is defined as the collection angle, can be selected by an entrance aperture. The spectrometer is a magnetic prism, which deflects the electron beam by 90°. The electrons are dispersed with respect to their energy due to the Lorenz force of the prism, so that electrons, which lost a characteristic amount of energy, are deflected more than electrons without any energy loss, as indicated by the colored rays in Fig. 3.9 (a). The dispersed electron energy spectrum is projected to a CCD camera. The spectrum itself is an electron intensity I distribution versus the energy loss ΔE (see Fig. 3.9 (b)). The spectrum is usually divided into two parts, the low loss ($0 - 50\,eV$) and high loss $> 50\,eV$ region. The low loss part contains in the beginning the elastic peak, also called zero-loss peak (ZLP), displaying the electrons without any energy loss, elastically scattered electrons and phonon losses. This peak is very strong compared to the rest of the spectrum, since the inelastic mean free path λ_{IMFP} of the electrons in most materials is much larger than the specimen thickness. Therefore, most of the electrons do not loose energy (or only very small amounts, e.g such as a

dew meV due to phonons). The full width half maximum of this peak determines the energy resolution of the TEM / EELS system and is around $1eV$ in the used machine in this thesis (not monochromated). Using modern monochromators, the resolution can be pushed to $4.2meV$ [71]. The rest of the low loss spectrum contains information about plasmon excitations (seen as green peak in Fig. 3.9 (b)) and outer shell electron transitions (valence electrons). The low loss spectrum can also be used to estimate the thickness of the TEM specimen. The specimen thickness is proportional to the inelastic mean free path of the corresponding material and the logarithmic intensity ratio of the zero loss peak and the total intensity of the spectrum:

$$t = \lambda_{IMFP} \cdot \ln\left(\frac{I_{lowloss}}{I_{zeroloss}}\right) \tag{3.11}$$

The high loss spectrum contains information of the inner shell electron transitions, which are seen in the spectra as characteristic ionization edges and are commonly called core losses. Typically, signals from the K-edge (that means an electron from the K shell was excited) are measured for light elements (such as O) and from the L edge for transition metals, such as Cu. One example is shown in Fig. 3.9 (b) by the red curve. The presence and position of such edges can give very precise qualitative and quantitative information of the chemistry of the specimen. The edge onset is used to assign an energy value to a characteristic electron transition of an element. The exact edge position can shift to lower and higher energies, depending on the valency of the investigated element, which is called a chemical shift. This chemical shift results for example from different oxidation states, which have different binding energies or from a different crystallographic environment. After the edge onset, a characteristic structure can be observed corresponding to the local density of states above the Fermi level. The ionization edges exhibit a more complex structure than a Gaussian peak and are called fine structure. The fine structure itself can be again divided into two parts, the energy loss near edge structure (ELNES) up to $50eV$ after the edge onset and the extended electron energy loss fine structure (EXELFS) $> 50eV$. These signals give information about atom bonding and oxidation states of the characteristic element. E.g. as shown later, the $Cu - L_{2,3}$ Edge is very different for pure Cu and Cu_2S due to differences in the d-band. The spectrum contains also a background, which has
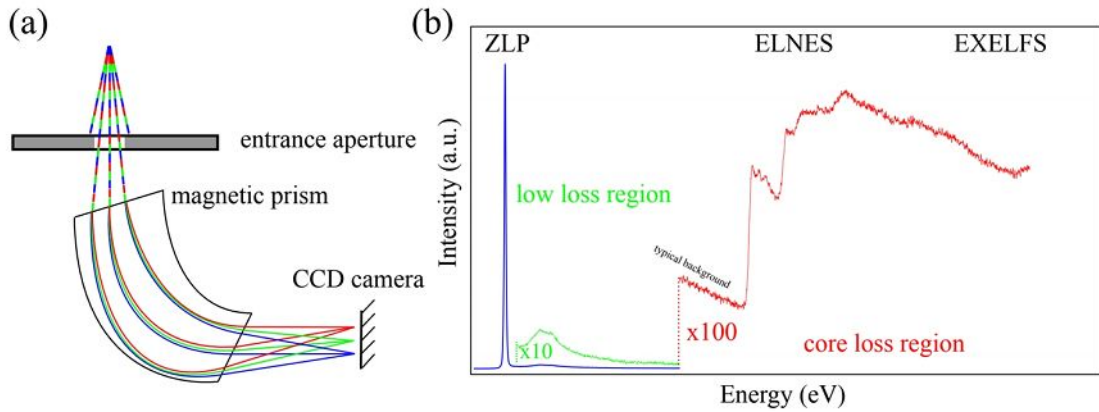
Fig. 3.9.: Working principle of EELS: (a) electrons with different energies (indicated by different colors) enter the spectrometer via an entrance aperture. The magnetic prism disperses the electrons with respect to their energy, which are then projected to a CCD camera. (b) shows sketch of a typical EEL spectrum showing the ZLP in black, the plasmon peak in green and a Cu ionization edge in red.

to be subtracted from the spectra for further analysis. Considering a thin specimen (i.e. $t \ll \lambda_{IMFP}$), the background intensity can be described by a simple power law function.

$$I = A \cdot \Delta E^{-r} \tag{3.12}$$

This function can be fitted to the background and is then subtracted from the spectrum, where A and r are the fitting parameter.

3.5. Atom probe tomography

Atom probe tomography (APT) is an analytic and destructive technique to identify the three dimensional elemental distribution of a small, needle shape specimen, using field evaporation. In principle an atom probe is a field ion microscope in combination with a mass spectrometer and is capable for single atom detection. The specimen is prepared mostly via FIB and should exhibit a tip radius in the range of $\sim 10 - 50\,nm$. The specimen is placed in an ultra high vacuum system and is cooled down to cryogenic temperatures, such as $50\,K$. The tip is aligned towards an ion detector with a distance of typically $\sim 10 - 100\,cm$. By applying a high voltage to the small tip a very high electric field is generated, which is slightly below the necessary ionization field.

The value of the high voltage strongly depends on the material itself in is typically in a range fo $2 - 12\,kV$. Ionization of single atoms from the tip surface is then triggered by voltage or laser pulses with typical frequencies of a few kilohertz. The ions are attracted to a position sensitive detector and the mass-to-charge ratio can be identified by the time of flight. With each pulse ideally a single atom is ionized and its position and species is measured until the whole tip is evaporated. Afterwards the measurements can be used with computational aid to reconstruct a three dimensional model of the elemental distribution with a high accuracy and at near-atomic resolution. A detailed description of APT can be found in [72].

3.6. Atomistic simulations

In this thesis, several simulation methods have been used to complement and support the experimental results in great detail. With molecular dynamic simulations, GB structures can be calculated using appropriate atomic potentials, which then can be compared to the STEM measurements. Evolutionary algorithm are used to predict many different GB structures for a specific system. Using STEM multi-slice simulations, STEM images can be simulated from the predicted and calculated GB structures.

3.6.1. Molecular dynamic simulations

MD simulations the movement of atoms and/or molecules can be simulated by solving Newton's equation of motion numerically [73]. During a short time frame (usually in the pico- to nanosecond range), the trajectories of atoms is calculated according to a potential function. In material science these are called interatomic potentials and are mathematical functions describing the potential energy of a system of atoms with a given structure (or atom positions). Compared to other atomistic simulation techniques, such as density functional theory, in MD systems with number of atoms of up to millions can be numerically simulated, which makes it a perfect technique to simulate GBs, since they usually have a larger cell size and many atoms are needed

a trustfully simulated a real structure (compared to a single unit cell of a single crystal for example). The simulation creates a configuration in a certain thermodynamic ensemble. For the GB simulations in this thesis, a canonical ensemble is used, which describes a closed system, with constant number of particle N, volume V and energy E and a specific constant temperature T. To realize a constant temperature, a thermostat algorithm is used, which basically adds or removes energy from the MD simulations. Lastly, the simulation needs some input of the geometry of the simulation cell. For the GB here, two Cu single crystals are rotated against each other, corresponding to the misorientation angle and axis of the GB. Then the two crystals are joined together along a certain GB plane. To generate the GB structure the γ-surface approach is used to sample basic translations of the two crystals, remove atoms and static relaxations to find the equilibrium structure [16, 41]. For that it calculates the trajectory for each atom, considering the interaction with its neighbors in small time steps. The code, which is most commonly used is the LAMMPS code [74, 75]. The final output of the simulations is visualized and processed with the program Ovito [76]

3.6.2. Evolutionary algorithms for GB structure prediction

In conventional MD simulation, the atomic density in the GB in the γ-surface approach is kept constant. However, in more recent studies it was pointed out that these simulation do not always predict the true ground state of the GB [25]. Zhu et al. presented a new algorithm, based on evolutionary search and machine learning to efficiently predict GB structures in a certain geometry with the additional parameter of the GB density in the GB core. Their tool generates populations of GB structures and searches for low energy structures [25]. In this way, data sets of several thousands of GB structures are predicted, including their energy (determined by empirical force fields) and atomic density at the GB core. By plotting all structures in a diagram as atomic density versus energy, local minimum GB structures can be found. The structures could belong to only one GB phase with different variation, or different GB phases may be found in the specific system. From the simulation, excess properties, such as excess volume or the GB stress tensor τ_{ij} can be extracted. All the structures can then by clustered according to their excess properties, by plotting for example

their GB stress τ_{11} against the excess volume. If there are multiple phases present, which describe a first order transition, this will be visible due to a change in excess properties. I.e. in the diagram the distinct phases are separated (for an example see [25] or chapter 6).

3.6.3. STEM image simulation - The multi-slice method

Multi-slice simulation are the most used algorithm to simulate TEM images, because it is very fast and efficient in large electron scattering simulations [77]. The sample is divided into very thin slices along the electron beam direction. Each slice can be described by an atomic potential $V_i(x, y)$, where i is the number of the slice and x and y are the coordinates in the slice plane. The simulation is based on two operations, the transmission operation and the Fresnel propagation. In the transmission operation, the electron wave function interacts with the potential of a slice and is modulated in its amplitude and phase. The Fresnel propagation then translates the modulated electron wave function to the next slice. These steps are repeated until each slice has interacted with the electron wave and the exit wave function can be extracted and used for image formation. Simulating TEM images and diffraction patterns with the multi-slice algorithms are very fast and efficient. STEM images, however, are much more time consuming, since the simulation has to be performed in each probe position. E.g. for a STEM image of the size $256x256$ pixel, 65536 probe positions have to be calculated. To perform these simulations, the program of Ophus et al. is used [77]. For a very detailed description on image simulations, the reader is referred to [68].

4. Experimental details

This chapter summarizes the experimental conditions, which were used in the chapters 6, 7 and 8. It explains in detail how the materials were processed, how the samples for the different measurement techniques were prepared and what machines and parameters were used for each measurement. The text is taken directly from the corresponding publications / manuscripts [18][32].

4.1. Samples

Cu thin films, used in chapters 6 and 7, were grown by MBE at room temperature on (0001) oriented Sapphire substrates followed by a post deposition annealing for 4 hours at $400\,^{\circ}C$. For the segregation experiments, the Cu film surface was sputter-cleaned prior to deposition of Ta and Zr thin films. Subsequently, $50\,nm$ Ta and $100\,nm$ Zr films were deposited each separately at room temperature on a small piece of the Cu film. To enable GB segregation the Ta/Cu film system was annealed for ~ 24 hours at ~ $600\,^{\circ}C$ and the Zr/Cu film system for ~ 5 hours at ~ $400\,^{\circ}C$ under high vacuum conditions.

Three copper alloys S14, S27 and S7920, used in chapter 8, were produced by Montanwerke Brixlegg. Scrap metals recycled following a route involving pyrometallurgy and hydrometallurgy, resulting in ultra-pure copper. The chemical composition was determined in the MPIE by wet chemistry and is shown in Table 4.1. The S concentration of S14, S27 and S7920 are 14, 27 and 7920 at. ppm, respectively. In order to investigate the influence of temperature during the tensile test on microstructural changes and GB chemistry, the sample with 27 ppm S was annealed for $4\,h$ at $500^{\circ}C$ under vac-

uum. The microstructure and composition were analyzed in the annealed state using WDXS and APT.

Table 4.1.: Impurity concentration in at. ppm from the alloys S14, S27 and S7920 obtained by wet chemistry

	S	Fe	Ag	K	P	Al
Alloy S14	14	13	7	29	18	9
Alloy S27	27	17	8	29	59	6
Alloy S7920	7920	10	9	29	89	2

4.2. Sample Preparation

For chapters 6 and 7, TEM specimens containing GBs (pre-characterized by EBSD) were prepared either by a site-specific plan-view FIB lift-out as described in ref. [78, 79] or as conventional cross-section lift-outs using a dual beam SEM / FIB instrument Helios Nanolab 600i (Thermo Fischer Scientific).

In chapter 8, the samples were prepared as follows: Flat tensile specimens were prepared by spark erosion from the bulk material with individual dimensions of about $2 \cdot 3 \cdot 10\,mm^3$. Tensile tests were performed on a Schenck - Trebel universal testing machine at three temperatures of $20 \pm 2°\,C$, $200 \pm 5°\,C$ and $400 \pm 10°\,C$. For macros-/ and microscopic investigations cube shaped samples were eroded from the bulk material using spark erosion. Optical light microscopy (OLM), SEM, WDXS and EBSD were performed on ground and electro-polished surfaces using phosphoric acid (D2 Struers). TEM specimens were prepared from pre-characterized GBs investigated by EBSD. Cylinders of $3\,mm$ in diameter were spark eroded from selected regions and cut into thin discs of $500\mu\,m$ with a diamond saw. These discs were ground down to $100\mu\,m$ by using silicon carbide paper with a grit size decreasing from $8 - 5\mu\,m$. Electron transparency was achieved by twin-jet polishing at $6.5\,V$ with an electrolyte of 70% ethanol and 30% HNO_3 at $-30.4°\,C$ and Ar^+-ion milling in a Gatan Precision Ion milling system II.

APT specimen were prepared from the pre-characterized GBs with a dual beam SEM / FIB (FEI Helios Nanolab 600i) using a site-specific, in-situ lift-out method [80]. Final

low energy cleaning at $5\,kV$ and $40\,pA$ was performed to minimize the Ga content in the sample, which was found to be at the background level in the regions of interest. To properly place the target GB inside the sharp, needle shaped specimen, TKD was carried out to monitor the position of the GB during milling [81].

4.3. Characterization techniques

The texture and global grain structure of the thin film as well as the bulk samples was determined by EBSD in a JSM-6490 (JEOL) operated at an acceleration voltage of $30\,kV$. EBSD has not been performed on the Ta/Zr covered Cu films, since no diffraction pattern could be recorded through the remaining Ta and Zr.

STEM imaging was performed in a probe-corrected FEI Titan Themis $60-300$ (Thermo Fischer Scientific) S/TEM equipped with a high-brightness field emission gun and gun monochromator operated at an acceleration voltage of $300\,keV$ using an HAADF detector (Model 3000, Fischione Instruments). The semi-convergence angle was chosen to $17\,mrad$ (in chapter 7) or $23.8\,mrad$ (in chapter 6 and 8) and HAADF images were recorded with a collection angle range of $73-200\,mrad$ and a probe current of $\sim 80\,pA$. Raising the camera length to $195\,mm$ changes the semi-collection angles to $38-189\,mrad$ and is referred here to low angle annular dark field (LAADF) imaging. BF, DF and HRTEM imaging was done in an image-corrected FEI Titan Themis $80-300$ (Thermo Fischer Scientific) TEM under negative C_s ($-10\,\mu m$) conditions using an accelerating voltage of $300\,keV$ [82]. Typically, STEM image series with $20-40$ images and a dwell time of $1-2\,\mu s$ were acquire. Afterwards the images were superimposed using a cross correlation to counteract displacements between single images due to specimen drift. Image processing, involving mainly Gauss and Fourier filtering as well as thresholding, was done in MATLAB.

For EDXS and EELS the probe current was raised to $\sim 150-200\,pA$ and X-rays were collected with the ChemiSTEM system (Thermo Fisher Scientific). EELS with a Gatan high-resolution Quantum ERS energy filter was done in STEM mode using a semi-collection angle of $5.4\,mrad$. In all measurements a zero loss and a core loss spectrum

were taken simultaneously [83] with a dispersion of $0.1\,eV/channel$ and a full width half maximum of the zero loss peak of $1.1\,eV$. For all spectra, the core loss region was aligned with respect to the zero loss peak and for background subtraction, a power law was fitted to the data [59].

APT measurements in chapter 7 was conducted on a LEAP 5000 XR local electrode APT from CAMECA instruments in laser-pulsingThe specimen temperature was set to $50\,K$, while the laser pulse energy of $85\,pJ$ at a frequency of $125\,kHz$ were used to evaporate the sample at a detection rate of 0.7%. The presence of oxides and other impurity elements was detected only close to the top surface indicating possible contamination during sample preparation and transfer between instruments. This initial sections, corresponding also to the Zr film, were discarded to focus in the Cu grains and their GBs and no further oxides were found.

APT measurements in chapter 8 were conducted using a LEAP 3000X HR (CAMECA Instruments, Madison, WI, USA) in the laser-pulsing mode with $30\,pJ$ pulse energy and $250\,kHz$ pulse repetition rate. The specimen base temperature was set at $60\,K$ and the target detection rate was 1 ion per 100 pulses.

4.4. Atomistic simulations

STEM multi-slice image simulations. STEM multi-slice simulations have been done using the Prismatic software developed by Colin Ophus [77, 84]. MD simulations serve as input files (xyz files) for the simulations in order to compare the calculated structures with the experimental data. The thickness of all simulated cells was set to $20\,nm$ and a slice thickness of 2Å was used. In total, 8 different phonon configuration were simulated which where incoherently summed up. The pixel size was set to $10\,pm$. The microscope parameter (collection angle, convergence angle, electron energy) where identical to the experiment.

Structure prediction by evolutionary search and clustering at 0K. The $0\,K$ evolutionary search was evolved over 50 generations. The search sampled different atomic densities given as the number of atoms inserted into the boundary in fraction of the

(178) bulk plane ranging from 0 to 1. Four independent evolutionary searches were performed, exploring structures with number of atoms ranging from 1000 to 4500 and 100 to 600 atoms. The GB cross-section was varied during the search between the smallest possible value and a factor of 4 times. The LAMMPS code [75] was used to evaluate the energies of the generated structures. The GB structures were inspected and visualized with OVITO [76].

Finite temperature molecular dynamics simulations. Molecular dynamics simulations were performed using the LAMMPS code [75] in the NVT ensemble with Nose-Hoover thermostat. Periodic boundary conditions were applied only along the $[11\bar{1}]$ tilt axis. The simulation block was terminated by two GB regions in the direction normal to the GB plane and their atomic positions were fixed during the simulation. In the direction perpendicular to the tilt axis within the GB plane, the boundaries are terminated by two open surfaces. The simulation cell was up to $6.3\,nm$ thick along the tilt axis, had an extension in direction normal to the GB plane of $14.1\,nm$ and was up to $4\,nm$ long in the direction perpendicular to the tilt axis within the GB plane. Isothermal simulations between $300\,K$ and $900\,K$ were performed for up to $200\,ns$. The simulated GB transitions were visualized with OVITO [76].

5. Literature Overview

This chapter gives a brief literature overview on the investigated topics in this thesis and where the results can be placed in the overall frame of the corresponding research field. This Chapter is based on the publications [18, 32] and from the manuscript in chapter 7 which is accepted by *Acta Materialia*.

5.1. Grain boundary phase transitions

Intensive research activities have been focusing on characterizing and describing different types of Gb phases and transitions between them, mostly in binary or multicomponent systems [5, 6, 23, 31, 85–88]. High resolution transmission electron microscopy (HRTEM) offers good opportunities to study the segregation behavior at GBs. Several examples exist in literature and show different GBs segregation phenomena in ceramic and metallic materials, such as a clean GB, monolayer, bilayer and trilayer segregation up to the wetting transition [89]. A TEM study on such results is shown in Fig. 5.1. Such studies provide deep insights in unusual segregation pattern formation or layering transitions at GBs and they were correlated to strongly impact interface mobility or cohesion [23, 30, 31, 87, 90–92]. Duscher et al. observed the formation of a bismuth monolayer at a Cu $\Sigma 5$ GB by scanning TEM (STEM) and electron energy loss spectroscopy (see Fig. 5.1 (h)) [23]. In a later study by Schweinfest et al., conducting first principle quantum mechanical calculations, the bismuth-induced embrittlement behavior was related to an atomic size effect between Bi and Cu atoms [93]. Another study, by Sigle et al., presented a HRTEM of the penetration of Ga ions to a $\Sigma 11$ GB in aluminum (see Fig. 5.1 (j)), which is known to promote liquid embrit-

tlement of Al [94]. Recently, Peter et al. reported on a different structural transition. They observed a silver (Ag) segregation-induced nano-faceting transition of an asymmetric Cu GB [30]. While the formed symmetric facets show a Ag enrichment, the remaining asymmetric facets remain Ag free. Accompanying Monte Carlo and molecular dynamics simulation support their experimental observation and show that Ag induces these facets and lowers the overall energy of the GB. Only the combination of atomic resolution STEM and corresponding computer simulations were able to reveal the underlying atomistic and thermodynamic origins in both studies and is the key method to study in detail GB phase transitions.

Such deep and experimentally investigations do not exist up to now for GB phase transitions in single component systems. These have been mainly studied by atomistic simulations, although these are limited by the accessibility of reliable semi-empirical atomic potentials [25, 34, 48, 49, 96, 97]. So experimental atomic scale observations still remain elusive. The direct observation of grain boundary transitions is often limited by experimental constraints due to their strongly confined nature [98, 99]. Indirect detection of these transition can be achieved by measuring the diffusion behavior or mobility of GBs and are often employed to interpret unexpected effects, such as abnormal grain growth, non-Arrhenius type diffusion or liquid metal embrittlement, which can be triggered by interfacial transitions [5, 86, 95]. Divinski et al. measured the diffusivity of Ag in a pure Cu bicrystal containing a $\Sigma 5\,(310)$ GB. They found a non-Arrhenius behavior at temperatures above $800\,K$, as shown in Fig. 5.2 (a). They argued that a structural transition at the GB must be responsible for this non-Arrhenius behavior [95]. With special molecular dynamic simulation, Frolov et al. [24] could show that a congruent transition of the $\Sigma 5\,(310)$ GB takes place at an temperature of $800\,K$, see Fig. 5.2 (b). A Monte Carlo study on the Ag segregation behavior at the two different GB phases, they show that one GB forms monolayer and the other bilayer Ag segregation (see Fig. 5.2 (c)). But up to now, direct experimental proof of this transition or another congruent transition were not shown. In this thesis, such a congruent phase transition in $\Sigma 19b\,[111]$ tilt GBs will be presented by high resolution STEM in chapter 6. With the help of advanced computer simulations it is shown that this is a first order transition.
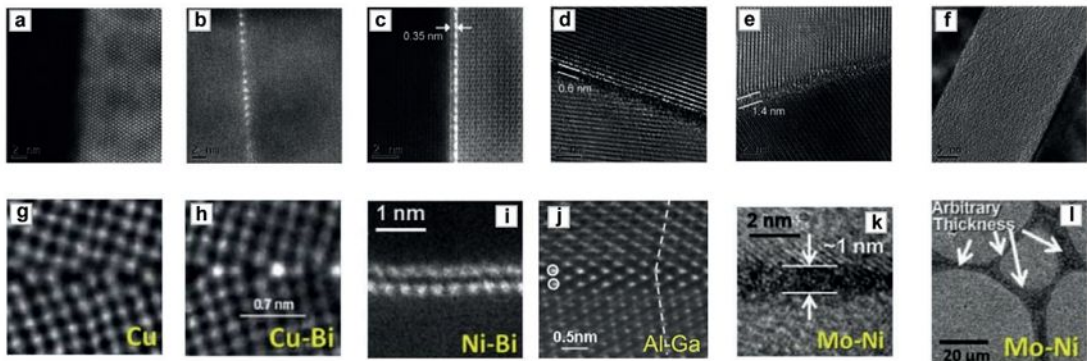
Fig. 5.1.: Segregation phenomena in multi-component alloys: (a-f) shows examples of segregation phenomena in ceramic materials, which are: clean GB (a), monolayer segregation (b), bilayer segregation (c), trilayer segregation (d), nanolayer segregation (e) and a wetting transition (f). The same phenomena also have been found in different metallic systems as shown in (g-l). This figure is taken from [6].
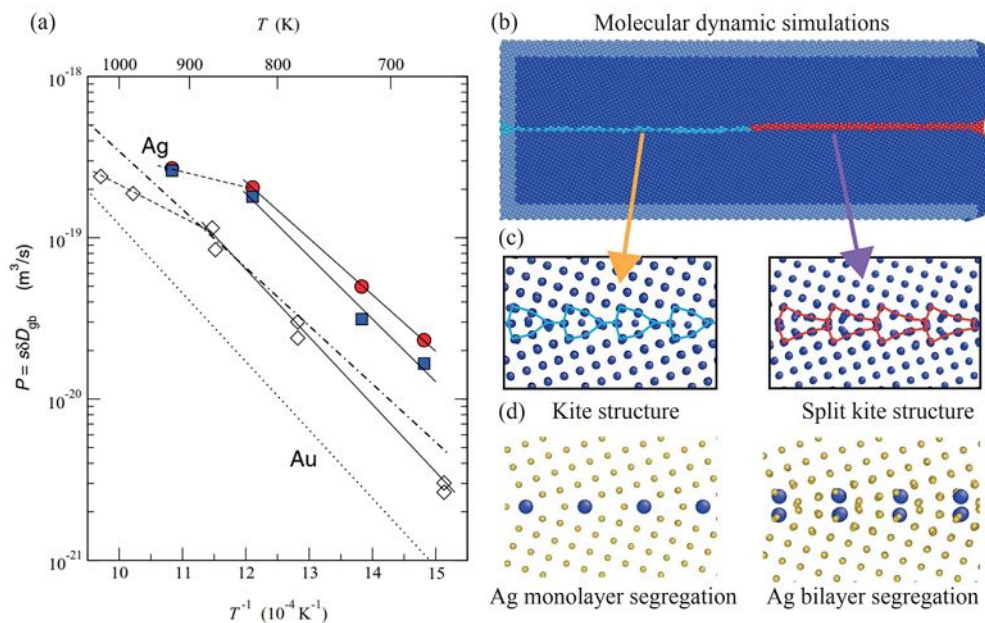
Fig. 5.2.: Indirect observation of a congruent GB transition: (a) shows the Arrhenius plot of silver segregation in a $\Sigma 5\,(310)$ GB in Cu. (b) and (c) show molecular dynamics simulations at $800\,K$ of that GB, revealing a congruent transition from a kite to a split kite structure. (d) Monte Carlo simulations of the Ag segregation result in a monolayer and bilayer segregation for the kite and split kite structure. This figure is composed out of figures from [24, 95]

5.2. The Cu-Ta and Cu-Zr system

As mentioned in the chapter 1, introducing impurity elements at GBs is a promising way to modify the GB properties. The reason for such property deviations can be related to impurity induced structural and chemical transitions [6, 24, 100, 101].

An emerging field where GBs and their transitions play an important role are nanocrystalline (nc) and nano-structured materials [102–107]. They have recently received broad attention because of their unique properties. Especially the mechanical behavior of such materials is to mention here since the yield and flow stress as well as the hardness can increase quite significantly [108–111]. Nc Cu is a particularly interesting candidate. While polycrystalline Cu has excellent electrical and thermal conductivity, it shows a poor mechanical strength [19]. This situation changes in nc Cu, which shows a remarkably high strength [108, 111, 112]. An example is shown in Fig. 5.3 (a) and was taken from [111]. However, rapid grain growth and the resulting instability of the microstructure at elevated temperatures strongly limit its commercial application. The instability is examplarily demonstrated in Fig. 5.3 (b) (filled square symbols) [113]. It shows that grain growth starts already at intermediate temperatures ($\sim 300\,^\circ C$). A way to stabilize the grain structure up to the melting point has been achieved by alloying with immiscible elements. It has been proposed that these elements tend to segregate to GBs and either kinetically or thermodynamically prevent grain growth. The kinetic approach utilizes either second phase precipitation to pin migrating GBs, a process know as Zener pinning [54, 114], or uses solute drag effects [115, 116]. In the thermodynamic approach, the GB free energy is reduced by solute segregation and thus the driving force for grain growth is decreased [115, 117, 118]. Two prominent candidates for stabilizing the nc grain structure are Zr and Ta. the corresponding phase diagrams are shown in Fig. 5.4.

Zr is seen as an excellent candidate to stabilize nc Cu due to its poor solubility in Cu ($0.12\,at.\%$ at $972\,^\circ C$ [119]), which is negligible at room temperature. The binary phase diagram is shown in Fig. 5.4 (a) and reveals that several intermetallic phases exist in this system [119]. In solution however, Zr induces a large elastic strain in the matrix, which is why the tendency to segregate to GBs in Cu is very high [113, 120]. That Zr

(a) Comparism strength between nano and corse grained Cu

(b) Temperature stability of pure Cu and Cu-Zr
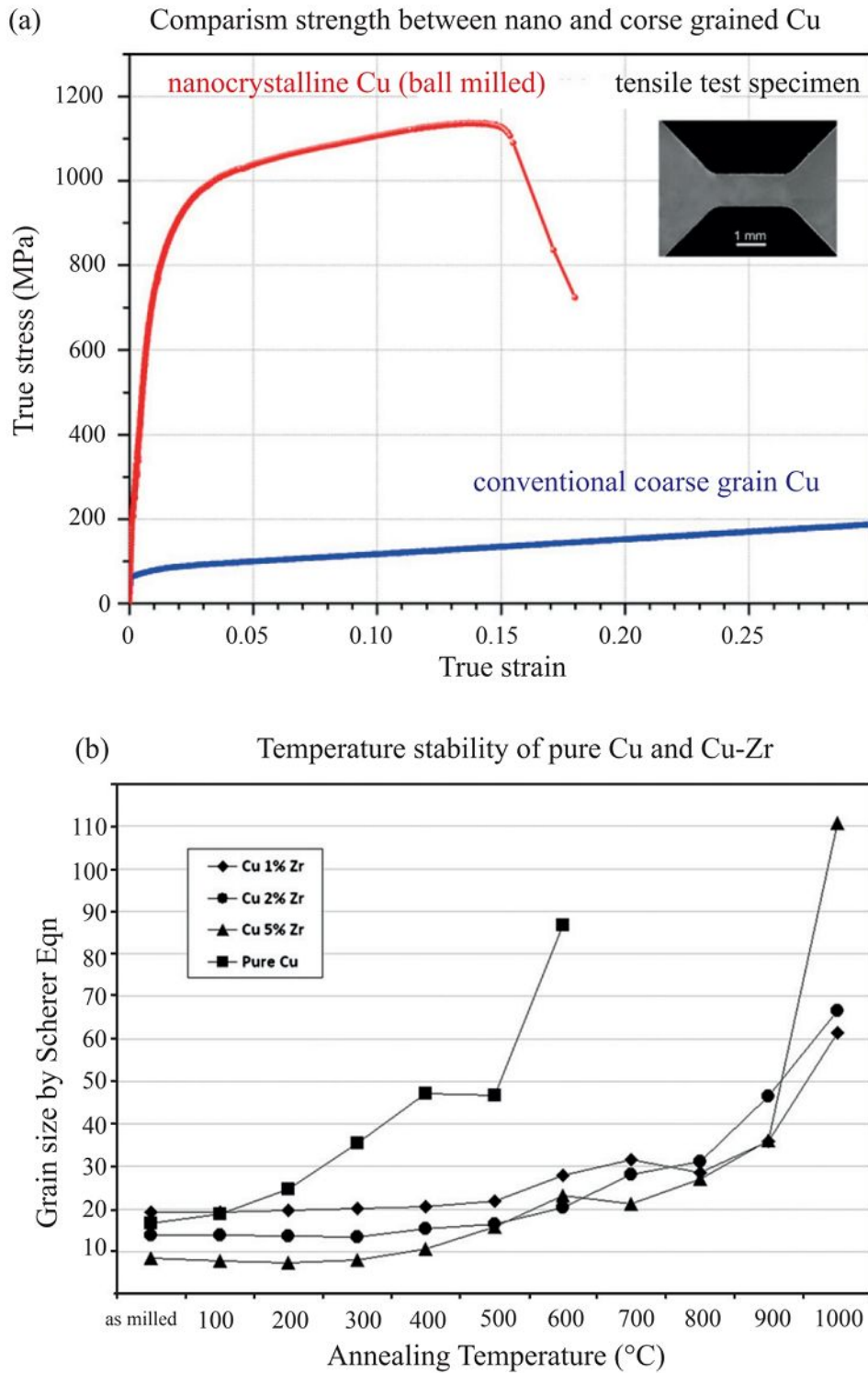
Fig. 5.3.: Mechanics and stability of nanocrystalline Cu: (a) shows the mechanical strength of ball milled nanocrystalline Cu compared to a conventional coarse grained Cu. The improvement in strength is of the order of 10. This figure belongs to [111]. (b) shows the temperature stability of pure Cu compared to three different Cu-Zr alloys. Each alloy was annealed for $1\,h$ at each temperature and the corresponding grain size was determined by X-ray diffraction. The plot belong to Ref. [113]

stabilizes nc Cu was already shown by Atwater et al. [113] by adding $1-5\,at.\%$ Zr to the nc Cu. The corresponding stability measurement is shown in 5.3 (b), where the grain size is stable up to temperatures of $\sim 800°C$. They related the stabilization to the formation of small scale intermetallic phases and Zirconia (ZrO_2) at GBs for the alloy containing $1\,at.\%$ Zr. However, a detailed high resolution study of the interfaces is missing. This was addressed a few years later experimentally by the study of Khala-jhedayati et al. [120] and theoretically by Pan, Rupert et al. [121]. They focused on the Zr segregation induced structural transition and reported on the formation of amorphous intergranular films (AIFs) or on Zr rich GBs depending on the cooling rate of the alloys. Their TEM study is shown in Fig. 5.5 (b) and (c) for the AIFs and the segregated GBs. They state that the AIFs reduce the GB energy and therefore the driving force for GB migration.

The binary phase diagram of Ta and Cu shows that the solubility of Ta at temperatures below $1000°C$ is negligible and that also no intermetallic phases exist (see Fig. 5.4 (b)) [122]. Furthermore, it was reported that also the diffusion of Ta at temperatures well below $1000°C$ is basically zero [123]. Therefore, the production of these alloys is already challenging and the most common techniques found in literature is ball milling [123, 124]. The formation of nano-scale Ta clusters and precipitates in nc Cu has been shown to increase the strength and stability of the microstructure, referred to as kinetic approach [124]. The hardness was found to increase by more than a factor of 2 compared to pure Cu with comparable grain size [123, 124]. TEM studies have already proofed the existence of Ta precipitates in theses alloys [123, 124] and is presented in Fig 5.6 (a) and belongs to the study of Darling et al. [124]. The Ta particles have a size distribution from $100\,nm$ down to a few nm. Their location is within the grains as well as at the GBs. Corresponding molecular dynamic (MD) simulations showed that the alloys suffered less from grain growth due to Ta cluster located at the GBs [123]. The results from Frolov et al. are presented in Fig. 5.6 (c-f). It shows that the grain size remains stable close to the melting temperature and it was found in a different study, that the Cu matrix still maintains its excellent electrical and thermal properties [125, 126]. However, a detailed experimental image on the microstructure evolution during the Zener pinning effect is still not resolved yet.
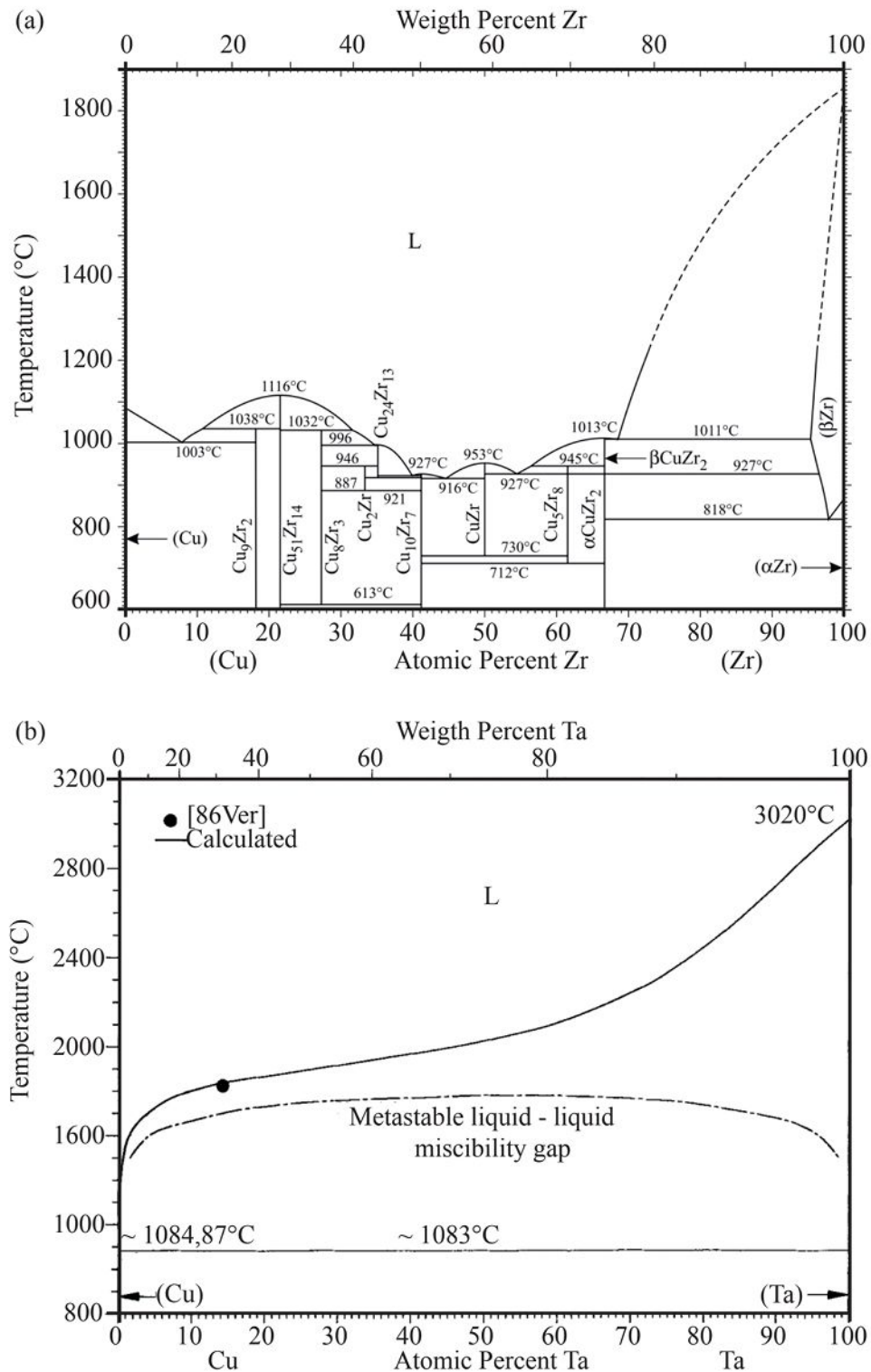
Fig. 5.4.: Binary phase diagrams of Cu-Zr and Cu-Ta: (a) Binary phase diagram of the Cu-Zr system taken from [119]. (b) binary phase diagram of Cu-Ta taken from [122]
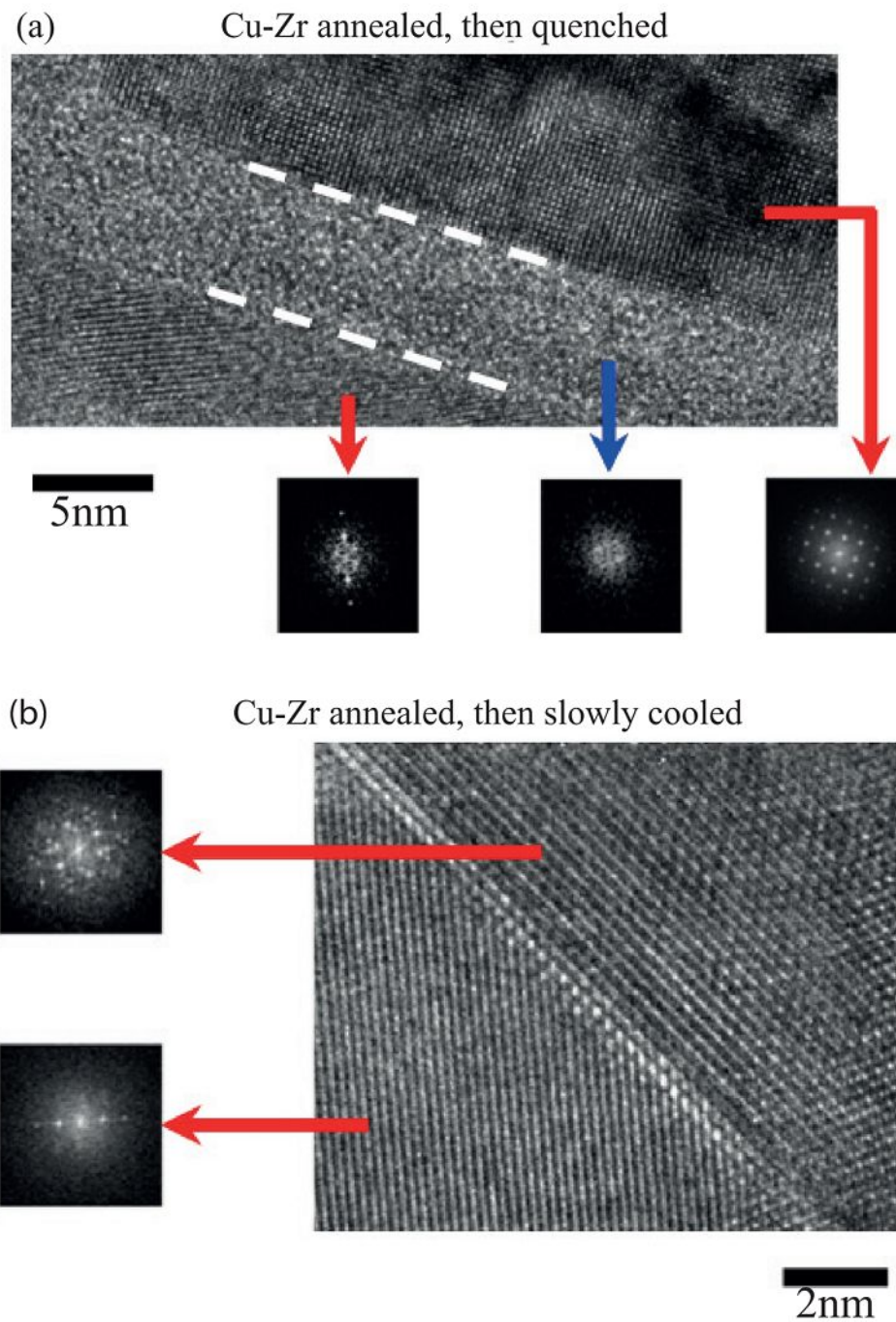
Fig. 5.5.: High resolution TEM study Cu-Zr GBs: High resolution TEM study, showing the formation of AIF (a) due to quenching of the alloy and the formation of Zr enriched GBs (b) due to slow cooling of the alloy. The insets show fast Fourier transformations of the regions indicated by the arrows and reveal the crystallographic orientation of the grains and the amorphous nature of the interface in (a). The images are taken from [120]

Fig. 5.6.: High resolution TEM and MD study of a Cu-Ta system: (A) shows a bright filed image of a nc Cu alloy with $10\,at.\%$ Ta. (B) and (C) show HRTEM image of the Ta particle distribution. The arrows indicate positions of small size Ta particles. The blue dots indicate Ta cluster at the GBs. (D-G) show MD simulations at different temperatures, showing that grain growth can be prevented by Ta clusters. The TEM image was taken from [124] and the MD simulations from [123]

5.3. The Cu-S system

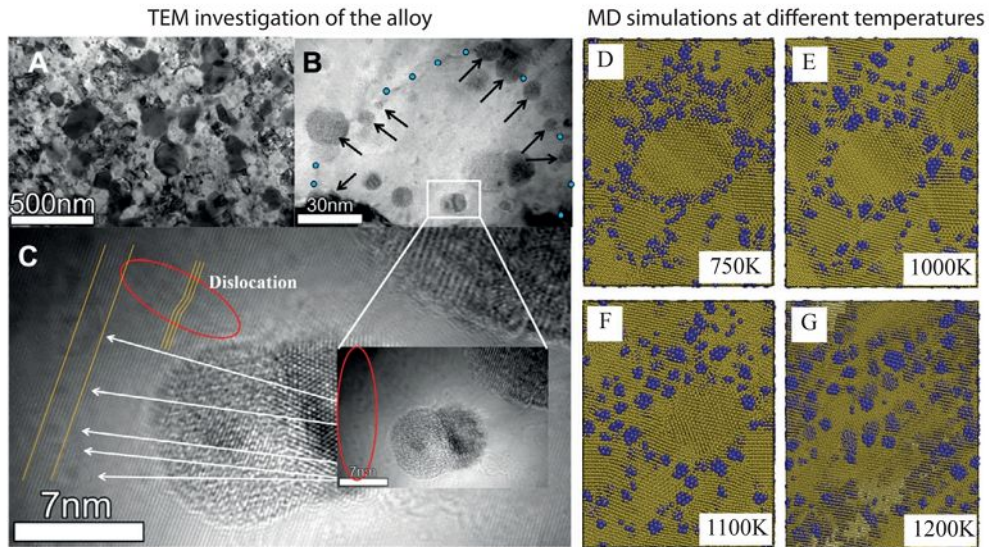Cu has a wide field of application, especially in microelectronic devices, due to its outstanding electrical and thermal properties, and is of special interest in many industrial application. However, Cu in its pure form always contains very small concentrations of impurities. Even though these concentrations can be lowered to orders of several atomic parts per million (ppm), one specific element can still cause dramatic failure of pure Cu, namely S. S induces intergranular embrittlement of Cu and is a longstanding problem since more than 100 years with an enormous impact on its mechanical durability and functionality [19]. The fundamental, atomistic mechanisms of embrittlement still remain elusive up to date and are commonly related to the segregation of S to GBs [9, 15, 19, 127, 128]. The detrimental effect of S on the mechanical properties was observed in high and ultra-high purity Cu [129, 130]. The reduction in fracture elongation occurs from room to intermediate temperatures and is influenced by the fracture mode, as well as the S content of the alloys. In these alloys it is proposed that S has a strong tendency to segregate to the GBs or to form stable

Cu-S compounds specifically at GBs [129, 130]. Since the equilibrium solubility of S in Cu is only 9 wt. ppm at $600°C$ [131], the mechanical properties of Cu reduce already at a S concentration as low as a few at. ppm. Fujiwara and Abiko showed a loss in ductility in high-purity Cu with 7.25 at. ppm at room temperature compared to alloys with lower S contents, such as 0.025 at. ppm and is shown in Fig. 5.7 (a) (the figure belongs to [129]). They proposed that the drop in ductility is related to the nucleation of cavities at the GBs, but also to the recrystallization behavior at elevated temperatures, which strongly depends on the purity of the Cu alloy and especially on the S content. However, the microstructural origins and the effect of S were not resolved and hence no direct proof of the embrittlement mechanism was ever provided.

The redistribution of S in high-purity Cu needs to be considered, since S is one of the elements with the highest diffusion rates in bulk Cu and at GBs [132]. The diffusion of S in Cu is described to be anomalous and at high temperatures it was found that the S diffusion coefficient is even higher than the self-diffusion coefficient of Cu [133, 134]. Another important aspect to consider is the formation of Cu-sulfides. From the Cu-rich side of the equilibrium phase diagram of Cu-S the formation of Cu_2S-type compounds can be established. These Cu(I)-sulfides can exist in three different crystal structures, known as low chalcocite (monoclinic), high chalcocite (hexagonal) and high digenite (cubic), as a function of temperature [135]. It was experimentally shown that Cu_2S easily forms an off-stoichiometric phase $Cu_{2-x}S$ with a lower coordination number compared to the Cu matrix and, therefore, leads to a faster diffusion of Cu in Cu_2S [132]. Furthermore, Surholt and Herzig [136] reported that S reduces the self-diffusion of Cu at the GB, which is explained by a strong interaction of S impurities with excess vacancies. This favors the formation of S vacancy pairs, which then segregate to GBs and dislocations. The high mobility of S at defects [137] leads to an accumulation of these S-vacancies pairs and the formation of copper sulfides by incorporating Cu atoms [132]. The formation of Cu_2S-type compounds, with its polymorphic temperature dependent structural transformations and its own brittle behavior, are a possible explanation for the intergranular embrittlement of Cu [131]. In addition, segregation of solutes to GBs can also favor embrittlement as was suggested by Briant and Messmer [138]. Their quantum mechanical cluster calculations in the Ni-S system showed that segregating impurities with higher electronegativity as
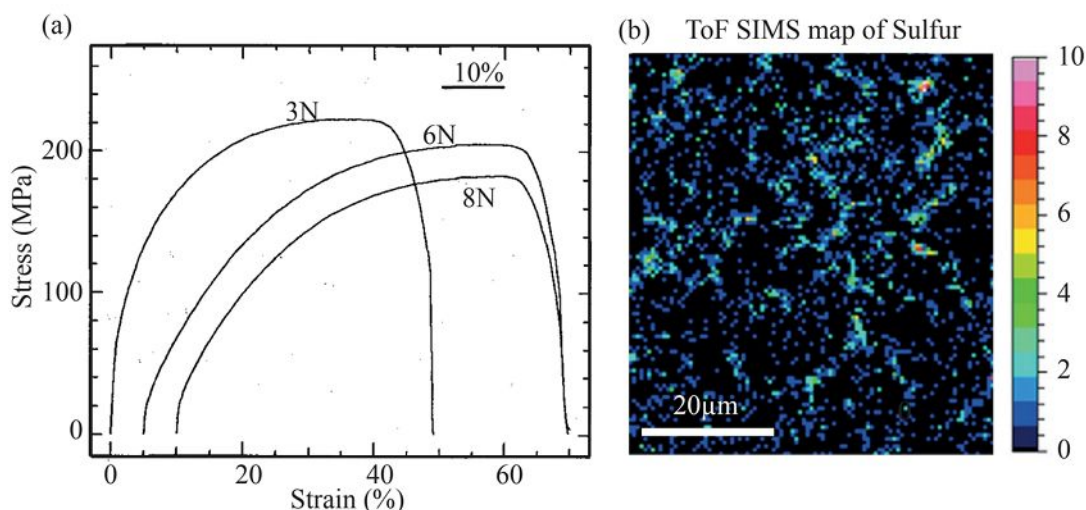
Fig. 5.7.: Effect of S in ultra pure Cu alloys: (a) stress-strain curve of three ultra pure Cu alloys at room temperature with a strain rate of $4.2 \cdot 10^{-5}$. The alloys have different S concentration: 3N contains 7.25 at. ppm S, 6N contains 0.027 at. ppm S and 8N contains 0.025 at. ppm S. Also other impurity elements are present in similar concentrations. The measurement is taken from [129]. (b) Typical time of flight SIMS measurement of fractured GB surfaces taken from [19].

the host metal draw charges of the metal and weaken the metallic bonds. They proposed from these results that this weakening is responsible for embrittlement. Since the electronegativity of Cu, Fe and Ni are very similar, this assumption should be valid for Cu as well.

Prominent techniques, which have been used for investigating the GB composition, are Auger electron spectroscopy (AES) and secondary ion mass spectroscopy (SIMS). At the fractured GB surfaces in Cu alloys an enrichment of S was detected [19, 131, 139, 140]. However, the main drawback of these techniques is the poor lateral resolution and the fact that the GB region has to be fractured. The fracturing of GB, can introduce structural and chemical defects that obstruct the detection of impurities. The lateral resolution is in the $100 \, nm$ range, making it impossible to draw conclusion on the atomic arrangement of solutes at the interface [15, 19]. An example of such a map is demonstrated in Fig. 5.7 (b), which shows a time of flight (ToF) secondary ion mass spectroscopy (SIMS) map of S and is taken from [19]. It becomes clear that these kind of measurements cannot provide chemical and structural information down to the atomic scale and atomic resolved TEM studies on unfractured GBs needs to be employed.

6. Experimental observations of grain boundary phase transitions unveiled by atomistic simulations

In this chapter, congruent phase transitions in pure, symmetric and asymmetric Cu GBs are presented. The combination of high resolution STEM and atomistic simulations revealed that the GBs undergo first order transitions. Due to the presence of a line defect, both GBs structures can coexist in the experiment and be observed simultaneously. The work presented here is based on the publication by T. Meiners, T. Frolov, G. Dehm and C.H. Liebscher [32] Note that the atomistic simulations and the machine learning algorithm were performed by T. Frolov. He also wrote parts of the publication with equal contributions.

6.1. Introduction

Novel predictive capabilities and simulation techniques have provided a completely new sight on the phase behavior of interfaces and multiple computational studies have shown that GB transitions can occur in a multitude of material systems [25, 48, 49, 98, 141]. First-order GB transitions are of special interest, since they are characterized by a discontinuous change in interfacial properties, such as segregation, diffusion behavior or mobility, and thus affect materials properties significantly. The exploration of their atomic scale origins becomes essential to distill fundamental thermodynamic properties and to establish strategies in utilizing these transitions for ma-

terial design. GB transitions have been further categorized into transitions involving faceting or dissociation into different orientations or congruent transitions, where two planar boundary phases of same composition transform into each other without a change of plane orientation [6, 12, 13]. Faceting transitions and their effect on interface properties have been investigated intensively in the past experimentally and by atomistic simulations [30, 92, 142–145]. Congruent transitions, where two planar boundary phases of the same composition transform into each other without a change of plane orientation [6, 12, 13], were thought to occur less frequently and only at high symmetry boundaries, but prevailing atomistic predictions indicate that they are a common feature of GBs influencing their segregation behavior, irradiation tolerance or self-healing capabilities [24, 25, 48, 49, 96, 141, 146–148].

In this work, we develop strategies to correlate atomic resolution STEM with GB structure prediction and atomistic simulations to discover the underlying nature of GB phase transitions at symmetric and asymmetric tilt GBs in pure copper (Cu). We make use of aberration-corrected HAADF-STEM (Z-contrast) [67] imaging to directly determine the atom positions at $\Sigma 19b\,[11\bar{1}]$ tilt GBs with different GB plane inclinations. The experimental observations are complemented by GB structure prediction using evolutionary search and clustering [25, 149, 150]. The predictive power of this algorithm allows to search for stable and metastable GB structures of the experimentally studied $[11\bar{1}]$ tilt GBs. Unsupervised machine learning is applied to discover novel ground state structures and to identify the intrinsic properties of the experimentally observed GB structures. The predicted GB phases are used as input for STEM image simulations to intimately link experiment and simulation. The GB phase coexistence and transitions are further explored by finite temperature MD simulations.

6.2. Results

6.2.1. Atomic resolution observations of GB phase transitions

The $[11\bar{1}]$ tilt GBs have been obtained by thin film deposition of Cu on (0001) oriented Sapphire substrate. Under these conditions a film with a strong $[11\bar{1}]$ texture develops with an average grain size of $\sim 100\,\mu m$. Hence, this template based approach exclusively obtains defined $[11\bar{1}]$ tilt GBs ideally suited for atomic structure observations. The majority of GBs in the film are twin and low angle GBs (up to 70%), but also e.g. $\Sigma 7$, $\Sigma 19b$, $\Sigma 37c$ and corresponding asymmetric boundaries.

In this study, we focus on $\Sigma 19b, [11\bar{1}]$ tilt boundaries. Fig. 6.1 shows two variants of congruent GB phase transitions imaged at atomic resolution. The phase transition illustrated in Fig. 6.1 (a) and (b) occurs at a near symmetric GB, the one shown in Fig. 6.1 (c) in a vicinal boundary. In both cases, two sets of characteristic structural units, referred to as pearl (blue) and domino (red) structures, are coexisting. The near symmetric boundary (6.1 (a)) has a measured misorientation angle of $\sim 48°$ and the GB plane inclination deviates $\sim 1°$ from the perfect symmetric orientation. A $\sim 11\,nm$ long domino structure (red) segment is embedded between two pearl segments (pearl) and it is seen that the GB follows a slight curvature leading to local deviations of the GB plane orientation of $\sim 5°$. However, facet formation is not observed. The magnified view of the right transition is shown in Fig. 6.1 (b). The domino structure is composed of double-square units changing successively in inclination, as also shown in Fig. 6.1 (d). The structural unit of the pearl segment is characterized by an alternation of a curved and square-type segments (see also 6.1 (e)). Both structures are separated by a line defect whose line direction is perpendicular to the image plane.

The same GB phase transition is observed for a vicinal $[11\bar{1}]$ tilt GB with an inclinational deviation of $\sim 5°$ as shown in Fig. 6.1 (c). The structural units of the domino and pearl structures are nearly identical to the symmetric boundary of Fig. 6.1 (a) and
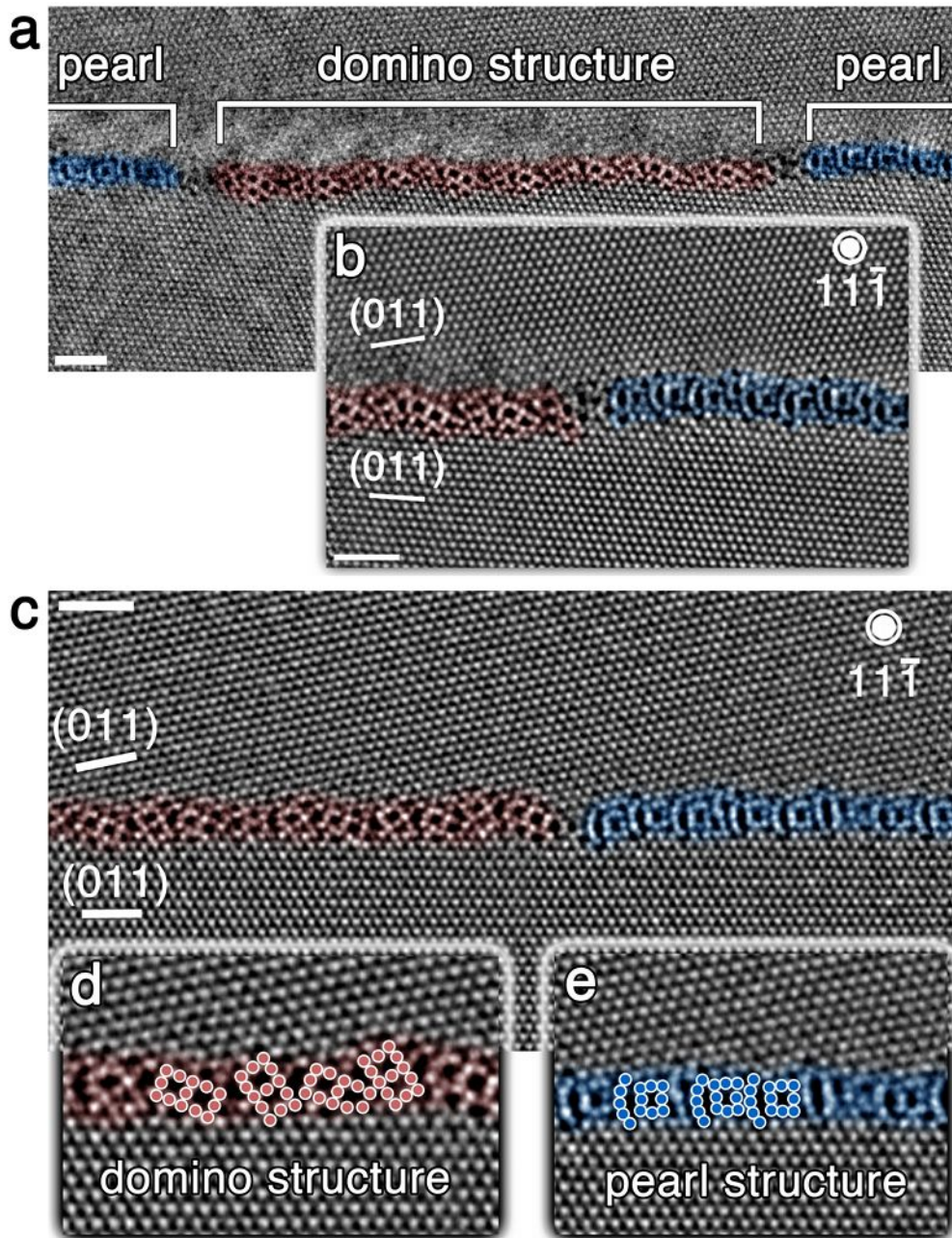
Fig. 6.1.: HAADF-STEM images of two congruent GB phase transitions: (a) Overview image of the transition at a near symmetric $\Sigma\,19b\,[11\bar{1}]$ GB with (178) boundary plane. The domino and pearl structures (or GB phases) are highlighted in red and blue, respectively. The overall misorientation of the GB is $\sim 48°$ with a deviation in inclination from the symmetric orientation of $\sim 1°$. (b) Magnified view of the right GB transition highlighting the differences in structural units of both boundary segments. (c) Congruent GB phase transition at a vicinal $\Sigma\,19b\,[11\bar{1}]$ GB with $\sim 47°$ misorientation and boundary planes of (011) lower grain and (279) upper grain. (d) and (e) illustrate close-up images of the domino and pearl structure of the vicinal boundary, respectively. The scale bar is $1\,nm$ in all images.

their detailed atomic arrangement is highlighted in Fig. 6.1 (d) and (e). A closer inspection of the domino structure of Fig. 6.1 (d) reveals that the double-square units show a similar alignment and sequence as compared to the symmetric boundary of Fig. 6.1 (a) and (b). In both cases, the regular order of the domino units is interrupted by irregular or disordered regions. The sequence of base structural units of the pearl structure, curved and square segments, is interrupted by curvy or linear subunits as shown in Fig. 6.1 (b) and (e). A deeper investigation of the GB inclination on the atomic structure is presented in the appendix A.2. The observations reveal that two GB phases coexist at a symmetric and asymmetric GB without change in GB plane orientation and composition, carrying all the ingredients of a congruent GB phase transition. Although the atomic structure is resolvable with unprecedented precision in an aberration-corrected STEM, the underlying thermodynamic origins and 3D structure of the GB phases remain unseizable.

6.2.2. Grain boundary structure prediction with evolutionary search and clustering

To investigate the structure and properties of the domino and pearl GB phases and model the structural transformations revealed by the experiment we perform GB structure search using atomistic calculations. The $0\,K$ GB structure search was performed using the evolutionary algorithm based on the USPEX code [25, 149, 150]. Following the evolutionary approach, the algorithm samples a diverse population of different GB structures, while improving them over many generations based on the energy minimization criterion. During the search, the structures change due to heredity and mutations, atoms are inserted and removed from the GB core to identify structures with different atomic densities. The search also changes the GB periodic dimensions to also sample large area reconstructions of the GB. The details of the method are described in Ref.[25].

The results of evolutionary search and clustering analysis for $\Sigma 19b\,[11\bar{1}]\,(178)$ GBs is illustrated in Fig. 6.2. The GB energy of hundreds of generated structures is plotted as a function of the number of inserted atoms $[n]$ measured as a fraction of the bulk (178)
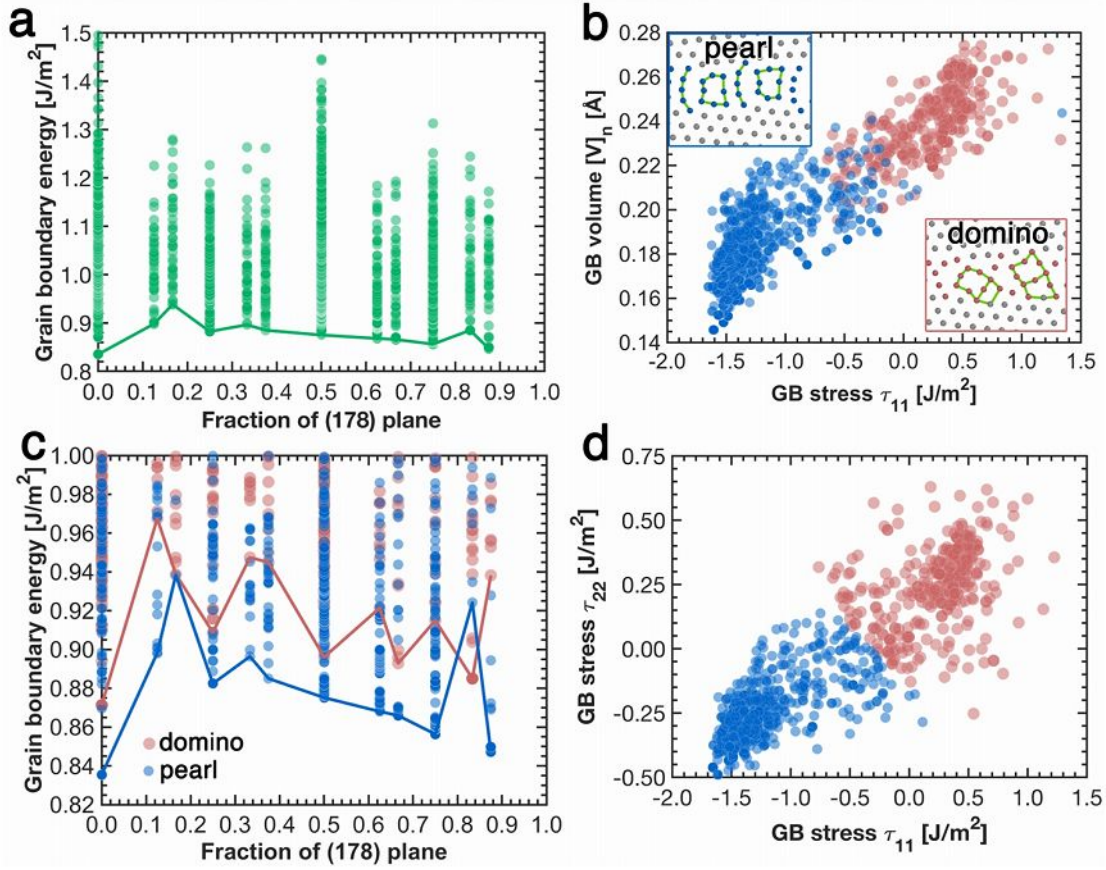
Fig. 6.2.: Evolutionary search and k-means clustering predict GB phases for $\Sigma 19b\,[11\bar{1}](178)$ **GBs:** (a) GB energy plotted versus the number of atoms in fraction of the (178) GB plane of all predicted GB structures. The solid line connects the lowest energy structures. (b) Unsupervised k-means clustering analysis of two GB phases according to similarities in their excess GB volume and stress τ_{11}. The lowest energy structures of domino and pearl are given as insets. (c) Plot of GB energy versus the number of atoms in fraction of the (178) plane after clustering analysis. (e) GB excess stress τ_{22} plotted against τ_{11}. The blue data points represent pearl, the red domino phases.

plane parallel to the GB as shown in Fig. 6.2 (a). The lowest energy configuration predicted by our search is identified as the pearl structure, similar to that observed in the experiment. Its structure is shown in 6.3 (a) and (b). This ground state is located at $[n] = 0$, which means that the insertion or removal of atoms is not necessary. No other minima with different $[n]$ are present, suggesting the absence of competing GB phases with higher atomic density. To identify possible metastable states, we performed clustering analysis following the methodology proposed in Ref. [25]. In this approach, the excess thermodynamic properties are used as descriptors to cluster similar GB structures and separate distinct GB phases that are expected to have different properties. Fig. 6.2 (b) shows the excess GB volume $[V]_n$ plotted against one

of the components of the excess GB stress τ_{11}. The plot reveals two clusters that we automatically labeled using the K-means clustering algorithms. These two clusters can also be identified in 6.2 (d), showing two components of the GB stress τ_{11} and τ_{22}. The blue cluster contains the ground state, as seen in the inset of 6.2 (b), and corresponds to pearl-like structures, while the red cluster represents metastable GB phases relative to pearl. The examination of structures in the red cluster established that they belong to the domino phase family and the inset of 6.2 (b) shows their lowest energy configuration. By re-plotting the GB energy of the clustered data as a function of inserted atoms, it becomes apparent that the lowest energy configuration within the domino-like structures has the same number of atoms $[n] = 0$ as the pearl phase ground state, which is indicated by arrows in 6.2(c). This analysis gives a strong indication that the structural transformation between pearl and domino GB phases is expected to be diffusionless, since it is not limited by the supply of vacancies or interstitials.

Although the two GB phases have the same number of atoms with energies differing only by $\sim 4\%$ ($\gamma_{pearl} = 0.835\,J/m^2$, $\gamma_{domino} = 0.871\,J/m^2$), they can be clearly distinguished by other thermodynamic properties. The excess volumes per unit area of the lowest energy pearl and domino GB structures differ by $\sim 36\%$ with $[V]_{n,pearl} = 0.14\text{Å}$ and $[V]_{n,domino} = 0.22\text{Å}$! This difference suggests that an imposed tensile stress is capable of stabilizing the metastable domino phase. The GB stress of the two phases is not only different, but even has an opposite sign with $\tau_{11,pearl}$ of $-1.66\,J/m^2$ and $\tau_{22,pearl} = -0.46\,J/m^2$, with respect to $\tau_{11,domino}$ of $0.25\,J/m^2$ and $\tau_{22,pearl} = 0.29\,J/m^2$. The different structures and the corresponding excess properties suggest that the experimentally observed transition is of first order.

The structural units of the lowest energy pearl and domino phases projected along the $[11\bar{1}]$ tilt axis are illustrated in Fig. 6.3(a) and (c). Similar to the experimental observations, the structural unit of the pearl phase is characterized by an alternation of a curved and rectangular subunits. A full structural unit is then composed of a mirror symmetric arrangement of two subunits, as highlighted in Fig. 6.3(a). The domino phase motif shown in Fig. 6.3 (c) shows a unique arrangement of inclined double rectangular subunits separated by irregular segments, which are also observed

in experiment (see Fig. 6.1 (b) and (d)). Viewing perpendicular to the tilt axis along [5$\bar{3}$2] reveals that the lattice planes in the upper crystal appear shifted for the pearl phase (6.3 (b)), but remain continuous without shift for the domino phase (6.3 (d)). The shift translation vector is 1/6 [920], which is inclined with respect to the image plane.

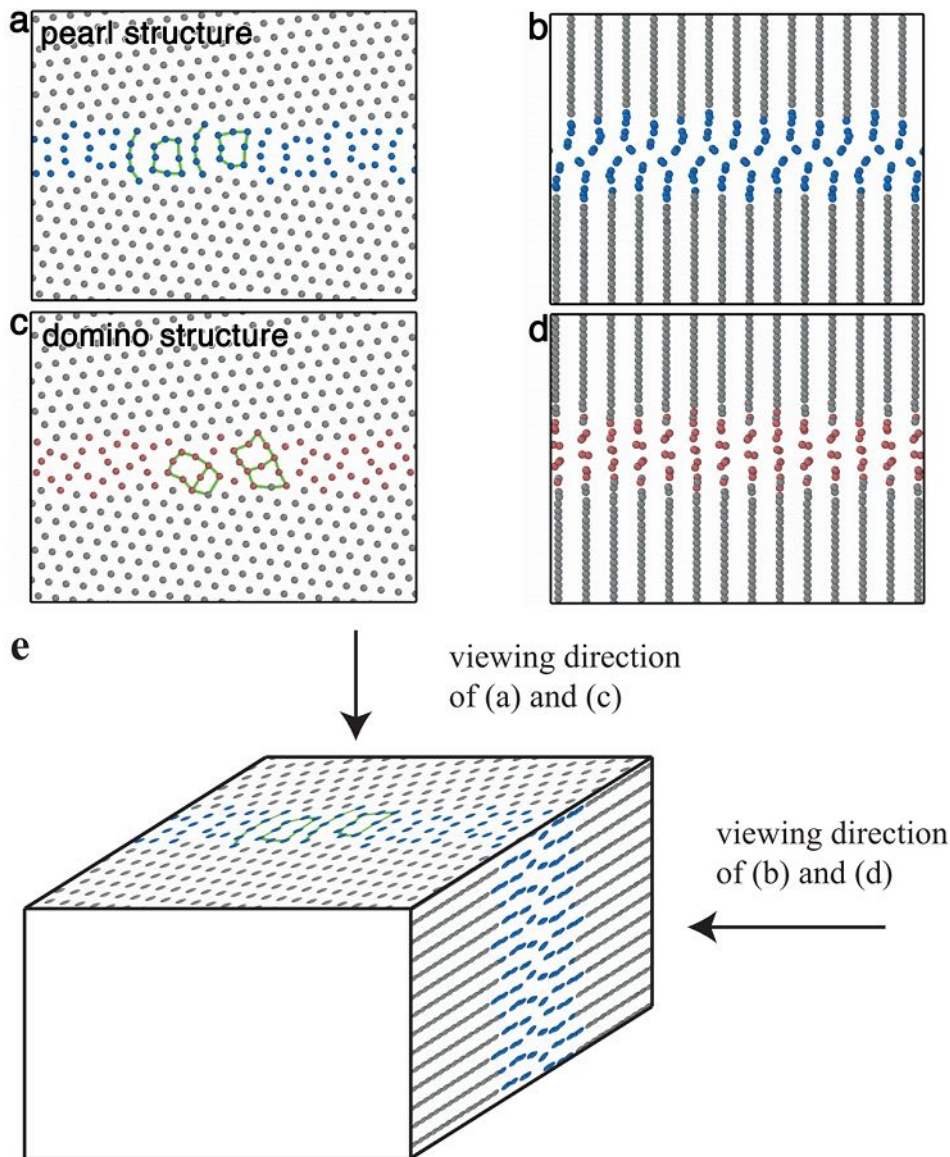**Fig. 6.3.: Lowest energy GB structures predicted by evolutionary search at** $0\,K$: (a) and (c) show projections along the [11$\bar{1}$] tilt axis of the pearl and domino phases, respectively. (b) and (d) visualize the GB structures perpendicular to the tilt axis viewed along [5$\bar{3}$2]. Repeat units of both structures are highlighted by green lines. (e) emphasizes the two different viewing directions more clearly.

6.2.3. Linking structure prediction and experimental observations

Intimately linking atomistic predictions and atomic resolution observations enables to uniquely quantify the discrete nature of the boundary types present in experiment. Multi-slice STEM image simulations [30, 77, 84] directly provide interpretable contrast from the predicted GB structures under similar conditions used in the experiment. An atomic resolution STEM image of the symmetric pearl structure and its
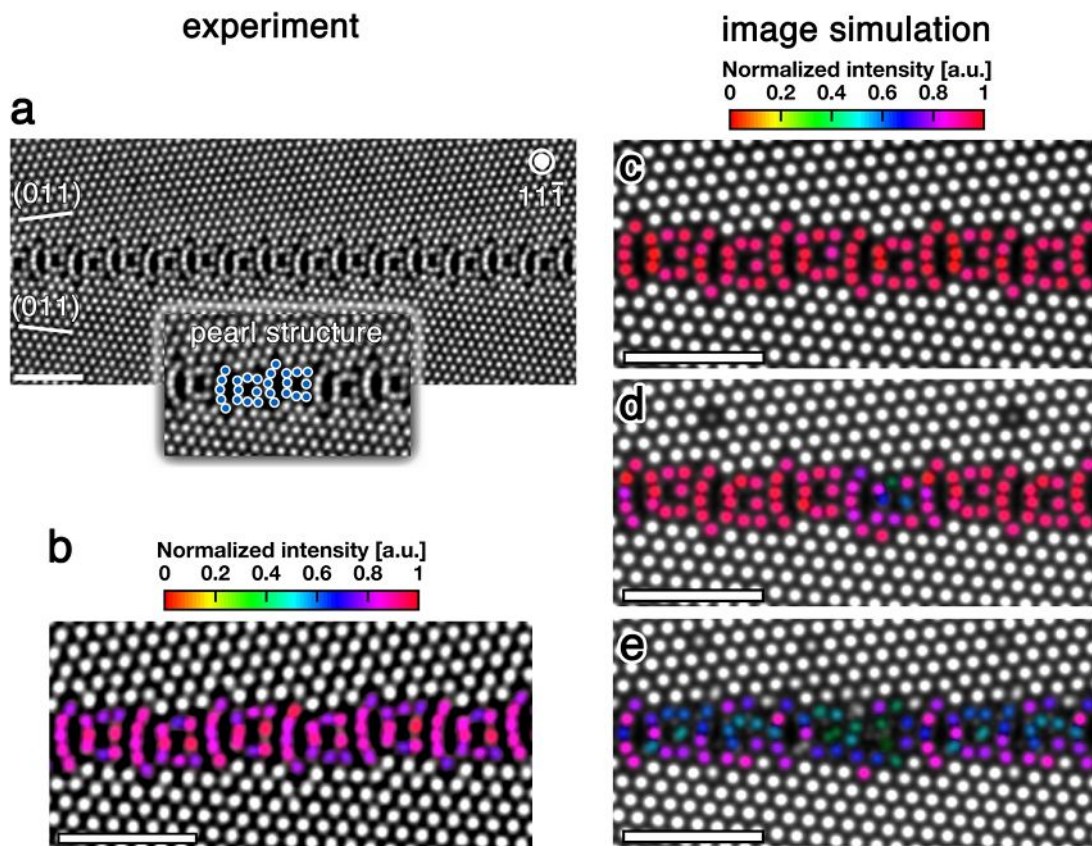
Fig. 6.4.: Linking atomic resolution observations and structure prediction: (a) Aberration corrected HAADF-STEM image of the symmetric $\Sigma 19b\,[11\bar{1}](178)$ pearl phase. Its structural unit is highlighted in the inset. (b) Color coding of the experimental GB structure based on atomic column peak intensities. (c-e) Simulated STEM images of predicted GB structures for sample thickness of 22 nm. The same color coding as in (b) was applied. (c) Lowest energy structure as shown in 6.3 (a) with GB energy of $835\,mJ/m^2$, (d) medium energy GB with $932\,mJ/m^2$ and (e) high energy GB with $1023\,mJ/m^2$. The scale bar is $1\,nm$ in all images.

structural unit are illustrated in Fig. 6.4 (a). The plain visual inspection reveals an excellent agreement with the predicted lowest energy state of the pearl phase presented

in Fig. 6.3 (a). Metastable GB structures are typically characterized by a high degree
of atomic disorder of the GB core or an increased number of GB defects. The result-
ing atomic displacements have a direct consequence on the atomic column intensity
and can hence be used to quantify the GB character. In Fig. 6.4 (b), only the peak
intensities at the GB core are colored based on normalized intensities.

The comparison with simulated STEM images of different grain structures shown in
Fig. 6.4 (c) reveals the best agreement with the lowest energy pearl structure (Fig. 6.4
(c)). An inhomogeneous intensity distribution in a square type subunit is observed
for the medium energy structure shown in Fig. 6.4 (d), which is not seen in the ex-
periment (Fig. 6.4 (b)). A high energy structure shown in Fig. 6.4 (e) is characterized
by strongly distorted structural subunits resulting in large scatter of atomic column
peak intensities. The corresponding projected GB structures are illustrated in the Ap-
pendix A.1. The atomic scale quantitative interlinking of experiment and simulations
shows excellent agreement and clearly reveals that the experimentally observed GB
structures resemble low energy states.

6.2.4. Grain boundary phase transition at finite temperatures

The evolutionary search produces zero-temperature structures and we now turn to
finite-temperature MD simulations to investigate the high-temperature GB behavior
and GB phase transitions. Our goal here was to reproduce the experimentally ob-
served transition between the pearl and domino GB phases and to gain new insights
into the kinetics of the transformation to explain the room-temperature stability of
the two-phase states found experimentally in both the symmetric and asymmetric
boundaries. We simulated pearl and domino GB structures separately at temper-
atures ranging from 300K to 900K using simulation blocks with periodic boundary
conditions along the GB as well as blocks with boundaries terminated at an open
surface (see in Appendix A.1). The open-surface simulation methodology was intro-
duced in Ref. [48] to allow for supply or outflow of atoms to the GB in case it is nec-
essary for achieving the ground state. Our simulations demonstrated that at ambient
pressure the pearl structure remained the ground state at all temperatures studied.

The domino structure was metastable and transformed into pearl by nucleation and growth, characteristic of first-order transitions. In agreement with the predictions of the $0\,K$ search, these simulations confirmed that the number of atoms at the GB does not change upon the transformation, i.e. the transformation is diffusionless. Fig. 6.5 (a) shows the simulation block after an initially uniform domino GB phase was annealed for several nanoseconds. The pearl GB phase nucleated at both open surfaces and grew inwards transforming the parent domino GB phase. The two structures are separated by a GB phase junction: a line defect that separates the two structures as highlighted in Fig. 6.5 (b). The two-phase structure shown in Fig. 6.5 (c) closely resembles the experimentally observed GB transition illustrated in Fig. 6.5 (d).
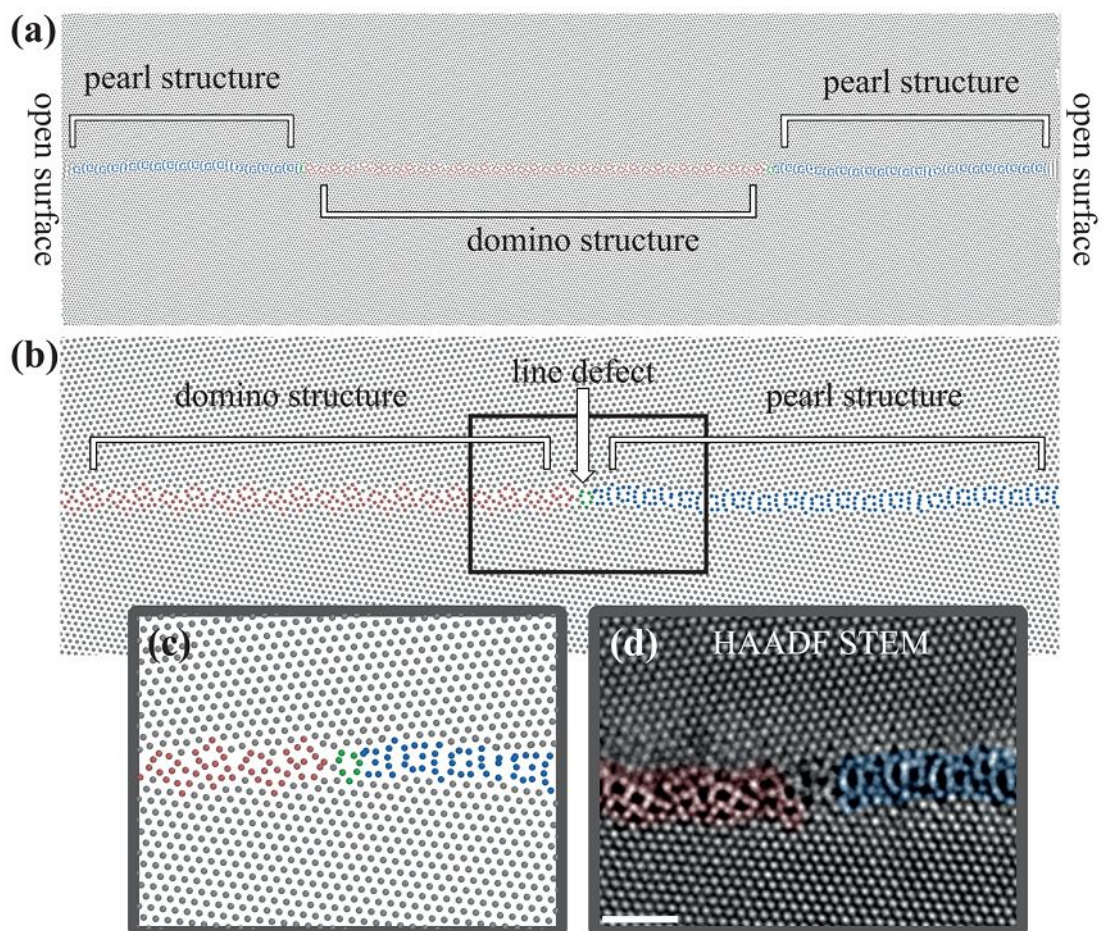
Fig. 6.5.: GB phase transition at finite temperatures: (a) MD simulation cell with open surfaces of a $\Sigma\,19b\,[11\bar{1}](178)$ tilt GB viewed along the tilt axis. The domino phase is highlighted in red, the pearl phase in blue. (b) Close up of the right phase transition with indication of the line defect (green), separating the two GB phases. (c) Magnified view of the line defect and phase coexistence of domino and pearl phase. (d) Experimental HAADF-STEM image of the symmetric GB phase transition. The scale bar is $1\,nm$.

In these simulations the pearl phase continued to grow until the entire GB is transformed. However, we also found that the velocity of the GB phase junction, which determines the rate of the transformation, strongly depends on the temperature and the defect length along the periodic dimension y, the $[11\bar{1}]$ tilt axis. At relatively high temperatures, such as $650\,K$, a complete transformation of the GB structure (Fig. 6.5) can occur within few tens of nanoseconds. Further simulations (see in Appendix A.1) with different sizes of the simulation block indicate that the motion of the GB phase junction is length dependent, suggesting that it migrates by a kink nucleation mechanism, similar to dislocations. The nucleation barrier of this thermally activated process is apparently high enough to kinetically trap the two-phase coexisting state on the MD time scale. When the length of the GB phase junction exceeds a few nanometers, we observe no migration of the junction at temperatures of $500\,K$ and below. It is expected that this trapping effect is even more pronounced at lower annealing temperatures.

Our atomic scale experimental discovery of phase transitions at symmetric and asymmetric tilt GBs in a pure metallic system remained so far unexplored. Atomic resolution imaging uniquely reveals the abrupt transition of $[11\bar{1}]$ tilt GBs with complex atomic arrangements. The two coexisting phases are clearly distinct by their differing structural repeat units. In contrast to assumptions based on thermodynamic concepts [12], the transition also occurs at an asymmetric GB. This indicates that GB phase transitions in pure systems can also emerge at more general boundaries and with this largely influence materials properties. The underlying nature of the observed coexisting GB phases was uniquely explored by novel GB structure prediction based on evolutionary algorithm and clustering analysis. Only the intimate link of atomic scale observations and structure prediction discovers that the GB phases differ in excess volume and stress. This transition is therefore of first order and will largely influence their segregation, diffusion and migration behavior, which in turn impacts the microstructural evolution [24, 25, 48, 148].

Our GB structure search predicts both experimentally observed pearl and domino GB phases. In the model, the domino phase is metastable with respect to the ground state pearl structure. Interestingly, both GB phases have the same number of atoms, sug-

gesting that they transition without the need to supply atoms by diffusion. The transformation is of first order, since the thermodynamic excess properties of the pearl and domino phases differ. This implies that they transform rapidly and their experimentally observed coexistence at room temperature is a surprise.

Another aspect to consider affecting the GB phase coexistence is the GB phase junction separating the pearl and domino GB phases. Our high temperature MD simulations of the GB phase transition at $650\,K$, similar to the annealing temperature of the thin film, perfectly reproduce the experimentally observed transformations (see 6.1 and 6.5). The strong dependence of the transformation rate on temperature and the GB phase junction length observed in our simulations suggests that the motion of GB phase junctions may require the nucleation of kink pairs. Their nucleation barriers at low temperatures may become too high impeding the transformation. As a result, the two phase GB states can be kinetically trapped on the experimental time-scale by cooling to room temperature.

The experimental observation of the GB phase transformation at room temperature can thus be rationalized in terms of GB phase coexistence at the annealing temperature and retarded transformation kinetics of the domino to the pearl GB phase. Both pearl and domino GB phases coexist during the annealing treatment and the stabilization of the domino phase is favored by internal stresses in the material. Subsequently, the domino GB phase starts transforming into the pearl phase while cooling from $673\,K$ to room temperature. The steadily decreasing mobility of the GB phase junction eventually freezes isolated domino GB phase regions down to room temperature, making their observation possible in the experiment.

Conventional phase transitions in the bulk control many materials properties. Much of materials science involves the delicate interweaving of thermodynamics and kinetics, using phase transitions to sculpt advantageous microstructures. While GB kinetics have long been understood to be key to attaining favorable grain structures, the possible role of GB phase transitions has been neglected. They have not been studied in metals since none had been observed. The recent suggestions of modeling [25, 48, 49] and now the discovery of GB phase transitions in a relatively simple elemental metal opens the door to new strategies for materials design. The combination of

STEM imaging and atomistic simulation enabled by evolutionary search provides a path to understanding GB phase transition in great detail. It has revealed GB transitions at an asymmetric boundary, something not considered possible.

6.3. Conclusion

Our experimental discovery of GB phase transitions in a pure Cu unveiled by evolutionary search and atomistic simulations greatly expands our understanding of the phase behavior of interfaces. The importance of segregation induced GB transitions impacting interfacial and defect properties has recently been evidenced in a broad number of material systems [31, 120, 151, 152]. Our intimate link of atomic resolution imaging and structure prediction enabled us to decipher the atomistic and thermodynamic nature of GB phase coexistence and transformation at a clean interface. Moreover, the transition at an asymmetric boundary was not even considered possible. This signifies that interfacial transitions can emerge even at general GBs and with this affect the microstructure evolution and properties in numerous material systems.

7. Impurity-induced structural transitions at complex $[111]$ tilt grain boundaries in copper

In this chapter, the influence of Ta and Zr to defined $\Sigma 19\,b$ [111] tilt GBs is investigated. The atomic structure of the pure GBs is directly compared to the GBs containing the alloying elements. The aim of the study is to get an understanding of the microstructure stabilization mechanisms in nanocrystalline Cu alloys by adding Zr and Ta. It is based on the manuscript T.Meiners, J.M Duarte, G. Richter, G. Dehm and C.H. Liebscher and is accepted by *Acta Materialia*.

7.1. Introduction

In chapter 1 it was outlined that nc Cu has gained an enormous interest in the past because of excellent mechanical properties. But since nc Cu suffers from strong grain growth at elevated temperatures, it is frequently alloyed with Ta and Zr in order to stabilize the microstructure. The atomistic mechanism of the stabilization, however, is still an open question. The effect of Ta and Zr on the atomic structure is investigated at defined [111] tilt GBs in Cu thin films, which are produced by MBE. Thus, a systematic study of pure and alloyed/segregated GB structures is performed. The representative GBs in this work are two symmetric $\Sigma 19\,b$ and corresponding asymmetric variants, with deviations of maximum ~ 6° from the symmetric orientation. The GBs exhibit long period structural units, which further decompose into sub-units. Even

though only the GB inclination changed by 30°, the two GBs show strongly differing atomic structures, which do not agree with the SU model as will be shown in the following. The Cu films are alloyed by sputter depositing Ta and Zr thin films at room temperature followed by a subsequent post-deposition annealing treatment and it is shown that GB diffusion is fast enough to introduce large amounts of Ta and Zr into the GBs. The effect of both impurity elements on the atomic structure is investigated by aberration-correct (S)TEM. It is shown that nano-scale Ta precipitates at GBs form, which act as local GB pinning points by bending the GB plane locally. The segregation behavior of Zr is observed to occur in two different ways. At a planar asymmetric GB, Zr homogeneously decorates the GB and causes a strong disordering of its atomic structure. Confined Zr segregation to GB steps is observed for a nano-faceted GB, where the steps are more disordered compared to GB steps in pure Cu GB. At the symmetric GB facets structural transitions are observed and compared to the structural units of GB facets in the clean GB.

7.2. Results

7.2.1. Global thin film grain boundary structure

EBSD reveals that the Cu films grow with a [111] fiber texture, as shown by the inverse pole figure map in Fig. 7.1. The film's grain structure is shown in the image quality map. The grain size can be determined to $\sim 100\,\mu m \pm 50\mu m$. The large error in average grain size results from a strong scatter in the grain size distribution, which includes grains with diameters of $\sim 300\,\mu m$ down to $\sim 10\,\mu m$. The grain size distribution is shown in Fig. 7.1 (c). Most grains exhibit a cylindrical shape, which translates to continuous changes in GB inclination along each grain boundary. Up to 80% of the GBs are low angle and twin boundaries ($\Sigma 3$). The remaining ones are different low Σ boundaries, such as $\Sigma 7$ ($\sim 1\%$), $\Sigma 9$ ($\sim 0.3\%$), $\Sigma 19b$ ($\sim 7\%$), $\Sigma 31a$ ($\sim 2.5\%$), $\Sigma 37c$ ($\sim 8\%$). The most frequent GBs are highlighted by colored lines in Fig. 7.1. The white/black regions in the center of the two EBSD maps illustrate positions from where TEM specimens were extracted by FIB. This procedure ensures that each TEM

specimen only contains specific, pre-selected types of CSL boundaries; in the present case a $\Sigma 19\,b$ GB.
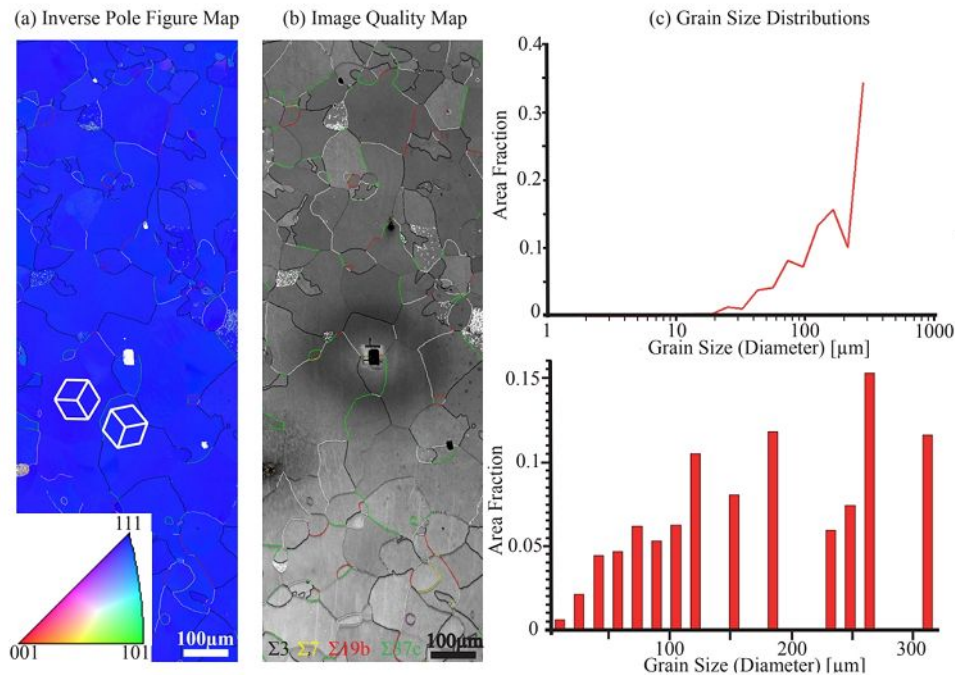

Fig. 7.1.: EBSD results of the Cu thin film grown on Sapphire: (a) The inverse pole figure map shows a [111] texture of the Cu film. The colored lines indicate the different GBs species in the film. The two white dices show the orientation of the cubic unit cell, further supporting the [111] orientation with different rotations around [111]. (b) The image quality map shows the microstructure of the film and also the color coded GBs. The most prominent GBs are low angle GBs (white lines), $\Sigma 3$ twin boundaries (black lines), $\Sigma 7$ GB (yellow lines), $\Sigma 19 b$ GBs (red lines) and $\Sigma 37 c$ GBs (green lines). (c) These two graphs present two different visualizations of the grain size distribution.

7.2.2. Atomic structure of pure $\Sigma 19 b$ grain boundaries

The atomic structure of four different GBs is depicted in Fig. 7.2, Fig. 7.3 and Fig. 7.4. Two are symmetric $\Sigma 19\,b$ with a misorientation of $\sim 47°$ and GB habit planes $(2\bar{5}3)$ (Fig. 7.2) and $(1\bar{8}7)$ (Fig. 7.3), which corresponds to a change in boundary plane inclination of $30°$. The other two GBs are asymmetric variants of the two symmetric GBs with different GB plane orientation resulting in small angular deviation between $\sim 2-6°$ (Fig. 7.4 (a) and (d)).

The $\Sigma 19\,b\,(2\bar{5}3)$ in Fig. 7.2 (a) is a straight and flat GB, which remains in the symmetric orientation for a length of $\sim 100\,nm$. It is difficult to observe longer segments of these

79

GB orientations, since the grains have mostly a cylindrical shape and therefore the GBs are often stepped or faceted. In between these segments, the same symmetric structural units can be consistently observed. The common description of CSL GB structures is obtained by characteristic SU [34, 38]. The full SU of the $\Sigma 19\,b\,(2\bar{5}3)$ can be divided into two sub-units as highlighted by red and green circles in the magnified view of the yellow rectangle of Fig. 7.2 (b). The filled red circle marks the CSL positions at this GB. The red sub-unit exhibits a square shape formed by 8 atomic columns followed by the green sub-unit, a trapezoid consisting of 4 columns. According to the nomenclature of the SU model, the GB structure can be written as $|\,ST\cdot ST\,|$, where S represents the red, squared and T the green, trapezoidal sub-unit. According to [34], the vertical lines " $|$ " represent one GB period along the GB plane and the dot " $\cdot$ " means that the sub-units are shifted along the GB by a half period. In the whole GB segment these two sub-units alternate and form the GB and disruptions of this sequence at the symmetric segments were not observed. With respect to its appearance, this GB structure is termed zipper structure in the following.

The $\Sigma 19\,b,\,(1\bar{8}7)$ shows a very different atomic structure (see Fig. 7.3 (a)). This boundary also remains straight over a length of $\sim 100\,nm$, but its SU appear completely different to that of the zipper structure. The red box highlights the region of the GB from where the SU are displayed in magnified view in Fig. 7.3 (b). Also here, two characteristic sub-units, marked by green and red circles, are observed. A particular arrangement of four of these sub-units builds up the repetitive unit of the GB. The green sub-unit consists of one "pearl chain" type arrangement (5 atomic columns) and one distorted rectangle (red), similar to the red sub-unit of the zipper structure. The total SU is composed of a combination of these two sub-units, which are mirrored with respect to the grain boundary plane, as is indicated in Fig. 7.3 (b) by the SU model notation. Here the SU notation is $|\,RP\cdot\text{Яꟼ}\cdot RP\cdot\text{Яꟼ}\,|$, where R represent the distorted rectangle (red), P the pearl chain (green) and the Я and ꟼ the mirror operation of the two sub-units with respect to the GB plane. It is obvious that this GB exhibits a longer period structure, since 4 sub-units build up a full SU. Also here, no deviation from this arrangement was observed for the symmetric boundaries. The filled red circles show CSL positions switching periodically from the left to right side of the GB due to the mirror operation of the sub-units. This GB structure is termed
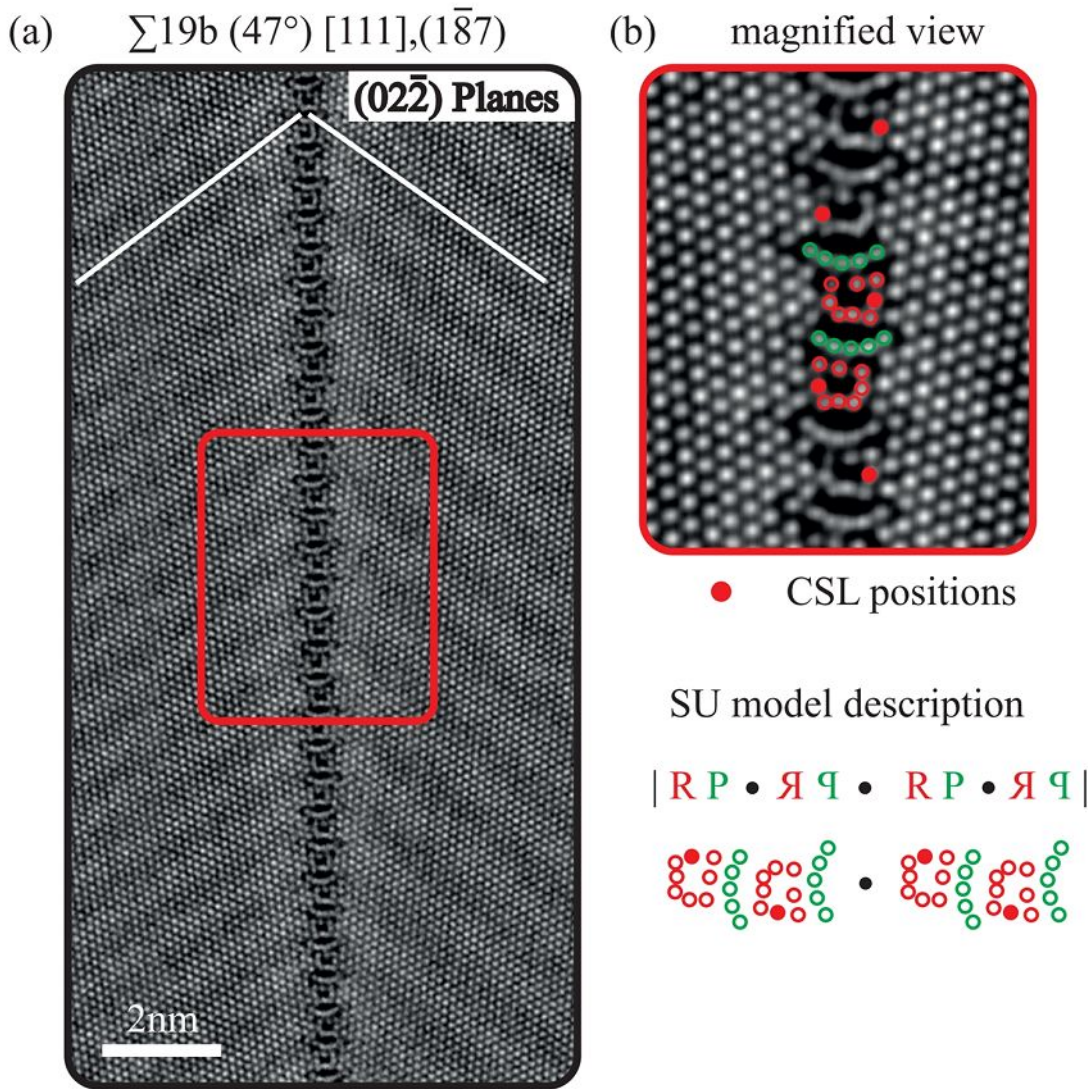
Fig. 7.2.: HAADF STEM micrograph of the symmetric $[111] \Sigma 19b, (2\bar{5}3)$: (a) shows the structure of the symmetric $\Sigma 19b, (2\bar{5}3)$. The white lines indicate the $(00\bar{2})$ planes and the colored boxes indicate the magnified view on the GB structure, depicted in (b). The green and red dots represent the structural subunits and the filled dots represent the coincide site lattice positions. On the bottom of (b) the respective SU model notation is visualized.

pearl structure in the following.

Asymmetric GBs with a small deviation of $\sim 2-6°$ from the symmetric orientation are frequently observed for both $\Sigma 19 b$ boundaries when tracing the GBs. For each GB one example is illustrated in Fig. 7.4 (a) and (c). Interestingly, both GBs show a different way of compensating for the asymmetric inclination of the GB habit plane.

(a) $\Sigma 19b\ (47°)\ [111], (1\bar{8}7)$ (b)   magnified view

(02$\bar{2}$) Planes

2nm

● CSL positions

SU model description

$|\text{R P} \bullet \text{Я Ⴁ} \bullet \text{R P} \bullet \text{Я Ⴁ}|$

Fig. 7.3.: [HAADF STEM micrograph of the symmetric $\Sigma 19b, (1\bar{8}7)$: (a) demonstrates the structure of the symmetric $\Sigma 19b, (1\bar{8}7)$ GB. The white lines represent again the $(00\bar{2})$ planes and the colored boxes the magnified view on the GB structure in(b). The green and red dots represent the structural sub-units and the filled dots the coincide side lattice positions. On the bottom of (b) the respective SU model notation is visualized.

In case of the zipper structure, the GB dissociates into $\sim 4\,nm$ long symmetric $(2\bar{5}3)$ facets that are regularly interrupted by steps as illustrated in Fig. 7.4 (a)). The magnified view, indicated by the purple rectangle in Fig. 7.4 (b), highlights a GB step and shows an extended, disordered core structure. The CSL lattices of the single symmetric facets still fit nicely together (not shown here) so that the step seems to be a shift along the CSL lattice. The facet length, and hence the number of steps, as well as the step height of $\sim 0.5\,nm$ adjusts in such a way as to compensate for the overall devia-
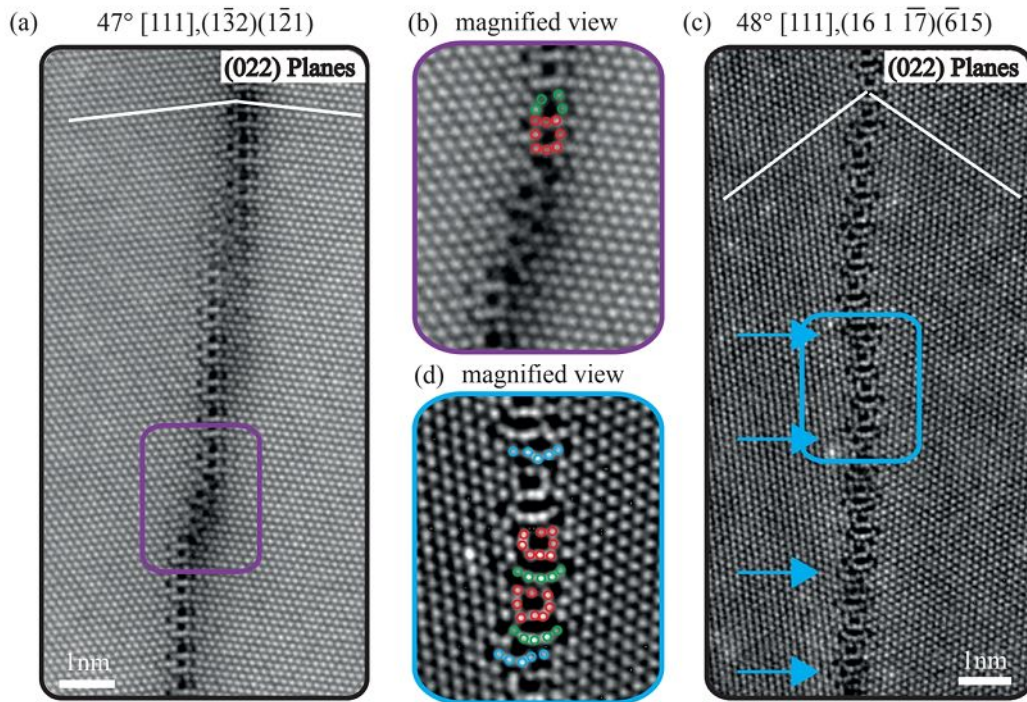
Fig. 7.4.: HAADF STEM micrographs of two asymmetric variants of the $\Sigma 19b$, GBs: (a) and (c) show asymmetric variations of the GBs shown in Fig. 7.2 and 7.3. The image depicted in (b), as indicated by a purple box, shows a magnified view on the GB step of (a). In (d), the magnified view in the blue box shows additional structural sub-units of (c), which are also indicated by the blue arrows.

tion in grain boundary plane inclination from the symmetric orientation of $\sim 5°$. For the pearl structure, a different scenario is observed, as demonstrated in Fig. 7.4 (d). Instead of decomposing into facets and steps, here, the asymmetric GB plane remains straight and incorporates additional sub-units to compensate for the asymmetric inclination, as indicated by blue arrows (Fig. 7.4 (c)). The blue box (see Fig. 7.4 (c)) shows a magnified view of the area highlighted, as depicted in Fig. 7.4 (d). These sub-units appear similar to the "pearl chain" (green sub-unit) of the symmetric case and their repeat distance depends on the magnitude of angular deviation. In the present GB, this deviation is $\sim 3°$ and the repeat distance of the extra units is $\sim 2\,nm$.

7.2.3. Tantalum segregation and grain boundary pinning

Fig. 7.5 shows CTEM and HRTEM images of a cross-sectional specimen of the Cu film alloyed with Ta. The Sapphire substrate is located at the bottom, the Cu thin film con-

taining a GB in the central region and the $50\,nm$ Ta film is located in the top part of the BF TEM image of Fig. 7.5 (a). The length of the GB was measured to $\sim 975\,nm$ and its overall appearance is straight. However, the region highlighted by a blue box, reveals a step towards the right grain, as shown in the HRTEM image in Fig. 7.5 (b). The step size is measured to $\sim 6.4\,nm$. Along the GB three of these steps can be observed, as illustrated by the blue arrows in Fig. 7.5 (a) so that the total step height between the top and bottom part of the GB adds to $\sim 18\,nm$. Therefore, it can be assumed that the GB migrated towards the right during heat treatment. Furthermore, a spherical Ta precipitate with $\sim 14.4\,nm$ in diameter is observed roughly in the middle part of the GB, directly in front of the step (see Fig. 7.5 (b)). A particle found in the upper GB region (red box) is illustrated in the BF image of Fig. 7.5 (c). It shows a more elliptical shape with a size of $\sim 12.4\,nm$ and $9.1\,nm$ and is directly located besides the GB, while the image contrast reveals that it is still connected to the GB. The high resolution TEM image of Fig. 7.5 (d) shows that the right grain is in [011] zone axis orientation, while the left grain is off zone axis and only the ($\bar{2}$00) lattice planes can be resolved. We observe that the grain boundary still adheres to the particle and that the right grain in front of the particle is extended into the region of the left grain, twisting the GB plane. It appears that the GB moved across the precipitate, but was not able to detach from its backside. A STEM-EDXS measurement in the same region and magnification as Fig. 7.5 (d) identifies the particle as a Ta precipitate. An elemental map of the Cu-$K\alpha$ and Ta-$L\alpha$ map is shown in Fig. 7.6 (a) and the corresponding X-ray spectra, one from the Cu matrix (red) and one from the particle (blue), in Fig. 7.6 (b). Additionally, a pronounced oxygen peak is observed in the region of the Ta-particle indicating that the particle could be oxidized. However, it should be mentioned that this might also be a result of the FIB sample preparation process and more likely, exposure of the specimen to air during sample handling. From the high resolution image in Fig. 7.5 (d), the particle appears amorphous. Investigating the fast Fourier transform (FFT) of HRTEM images in other orientations and different particles did also not reveal any indication that the particles are crystalline. An example of an FFT obtained only from the Ta-particle is shown in the inset of Fig. 7.5 (d).
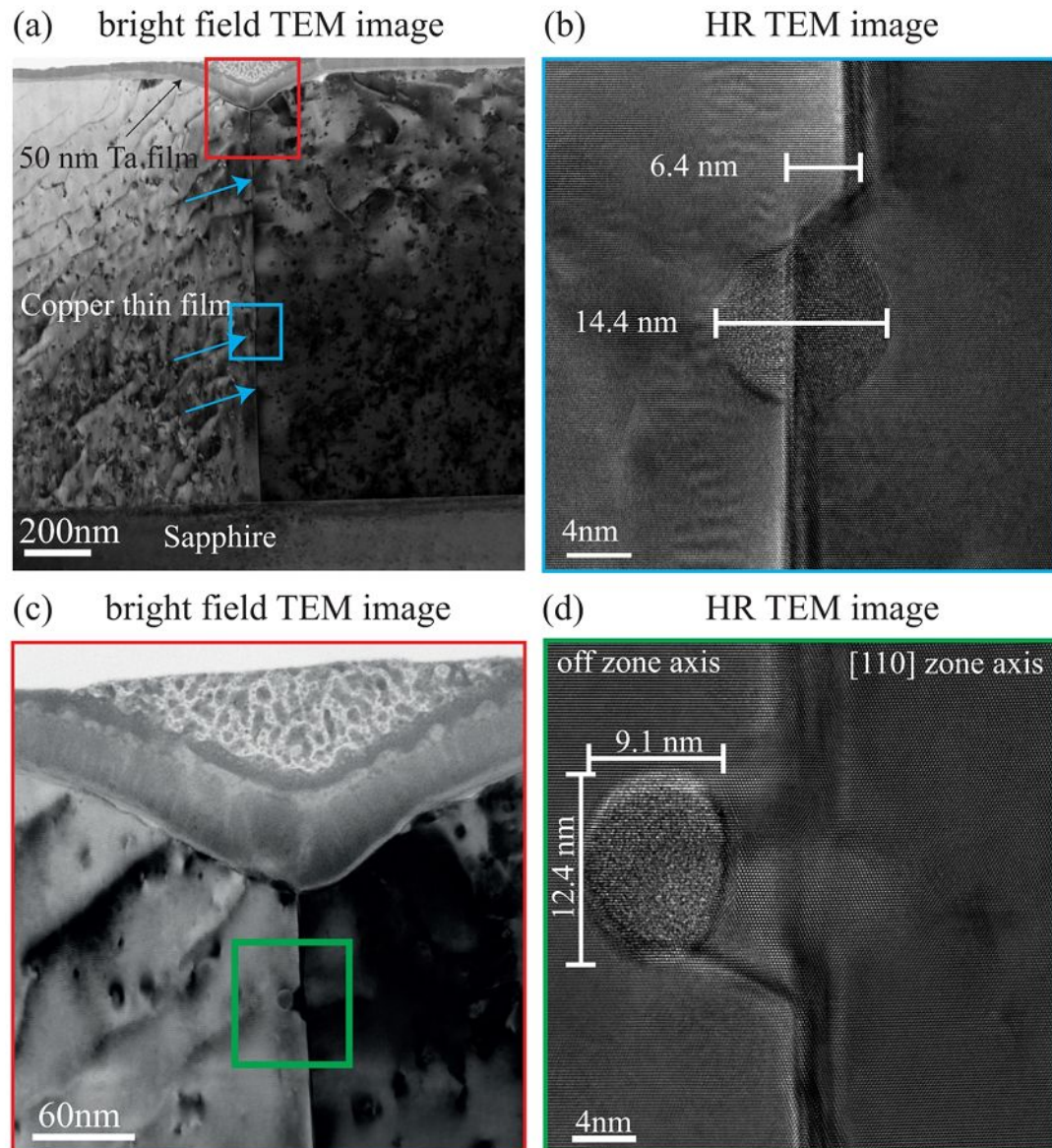
(a)   bright field TEM image   (b)   HR TEM image

50 nm Ta film

Copper thin film

6.4 nm

14.4 nm

200nm   Sapphire

4nm

(c)   bright field TEM image   (d)   HR TEM image

off zone axis   [110] zone axis

9.1 nm

12.4 nm

60nm

4nm

Fig. 7.5.: TEM investigation of the Cu-Ta film system: (a) Conventional bright field (BF) image of a cross-section specimen showing the Alumina substrate, the Cu thin film with the GB being perpendicular to the substrate and the Ta thin film. The blue inset (b) shows a spherical particle (HRTEM image) sitting directly on the GB and right in front of a step. The red inset in (c) shows a BF image of another particle sitting next to the GB, which is pinned to the GB. (d) illustrates the atomic structure at that position in a HRTEM micrograph.

7.2.4. Zirconium segregation and grain boundary disordering

Adding Zr to the thin film reveals a different segregation behavior than for Ta. The results for an asymmetric $\sim 49°\,[111], (1\bar{6}5)\backslash(1\,\bar{1}6\,15)$ GB with the pearl structure is shown in Fig. 7.7 (a). The planes deviate from the symmetric $(1\bar{8}7)$ plane by $\sim 2.3°$
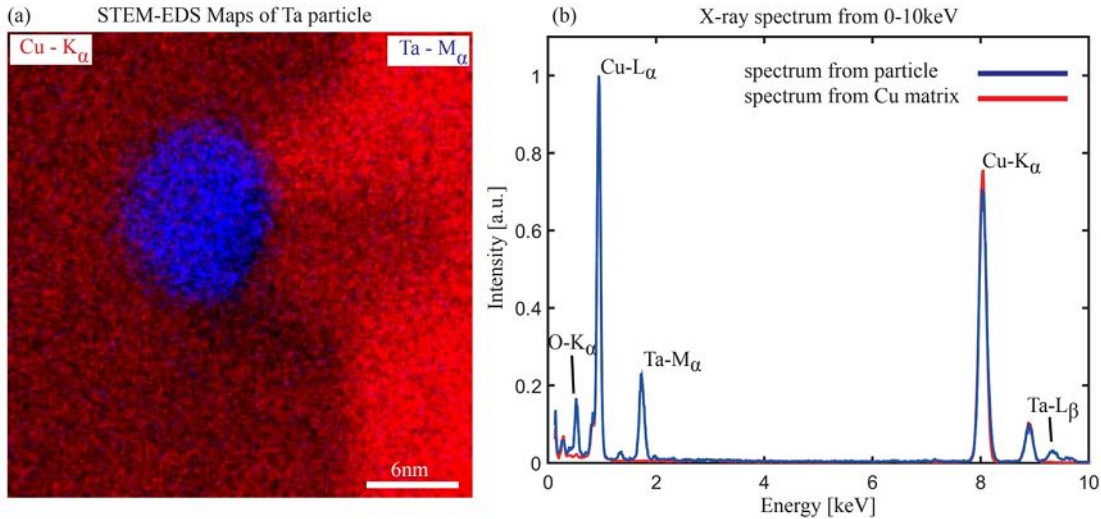
Fig. 7.6.: STEM-EDXS analysis of a Ta particle at the Cu GB: (a) depicts a STEM-EDXS maps of the particle using the Cu-K_α (red) and Ta-L_α (blue) edges at the exact position from Fig. 7.5. In (b) two X-ray spectra are plotted together belonging to the pure Cu grain (red) and to the particle (blue).

and ~ 3.4°. In the STEM micrograph, the GB appears dark under HAADF conditions and the identification of structural motifs is barely possible. This contrast is observed almost entirely along the GB. A magnified view of the atomic structure is illustrated in the insets of regions highlighted by purple and red rectangles in Fig. 7.7 (a). A strong high pass Fourier filter was applied in order to emphasize the structure. Despite the weak atomic column contrast, similar structural units, indicated by green and red dots, as in the pure Cu GB of Fig. 7.4 (d) can be identified in the purple region. But as shown in the area marked by a red box in Fig. 7.7 (a), distorted or even disordered variants of the structural motifs are observed. The blue colored atomic columns show additional sub-units resulting from the asymmetry of the GB. In the upper region only one line of extra atomic columns is visible, while two extra lines are found in the lower part. The STEM-EDXS maps of the Cu-L_α and Zr-L_α X-ray lines taken in the purple region of Fig. 7.7 (a) are illustrated in Fig. 7.7 (b) and clearly reveal that the GB is strongly decorated with Zr. The corresponding X-ray spectra, taken from the grain interior (red) and at the GB (green) are shown in Fig. 7.7 (c). The inset in the spectrum, indicated by a dashed box, illustrates the intensity modulation of Cu, Zr and O by taking a line scan across the GB. No clear sign of O enrichment at the GB is observed in the line scan, although a slight oxygen (O) peak is present in the GB spectrum of Fig. 7.7 (c)). All together, Zr leads to a strong disordering of the GB struc-

ture, which leads to displacements of atomic column positions perpendicular to the viewing direction. This in turn, leads to de-channeling of the electrons, which leads to an effective reduction of the atomic column intensity in the HAADF images.
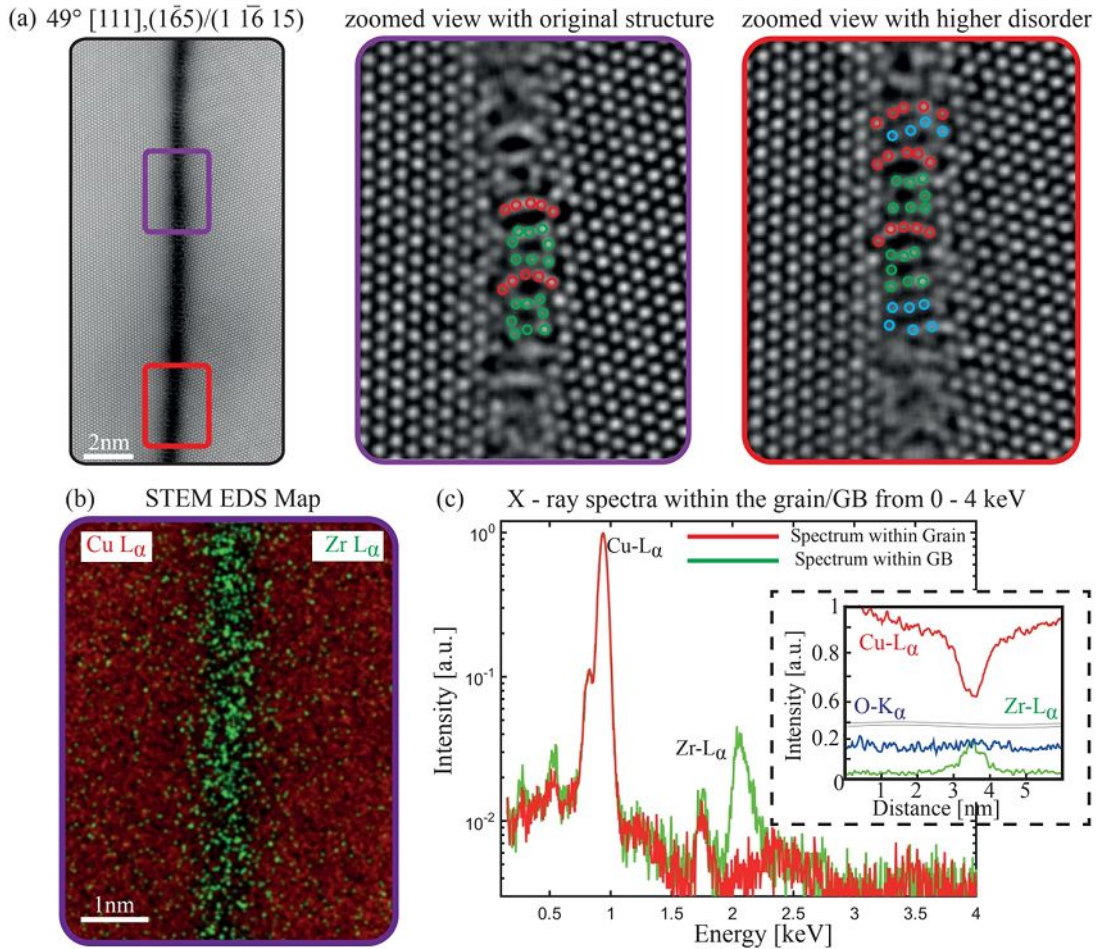

Fig. 7.7.: STEM and EDXS characterization of the Zr segregated pearl structure: (a) HAADF STEM image of an asymmetric $\sim 49°\,[111], (1\bar{6}5)\backslash(1\,\bar{1}\,\bar{6}\,15)$ alloyed with Zr. The insets show two different magnified views of the atomic structure using a strong high pass Fourier filter to highlight the atomic columns. The purple inset shows a region with the original GB structure and the red region with some deviations, as indicated by the colored dots. (b) STEM-EDXS measurements, containing a map with the Cu-K_α (red) and Zr-L_α (green). The graph in (b) shows the spectra (in log scale of the y-axis) taken from the grain and the GB, showing an increased Zr concentration at the GB. A concentration profile is depicted in the dashed inset of (c), showing the Cu, Zr and O intensity across the GB.

In the case of an asymmetric $\sim 49°\,[111], (12\bar{3})\backslash(\bar{2}11)$ GB, adapting the zipper structure, we observe an inhomogeneous segregation of Zr, which appears as dark contrast regions at the GB steps as seen in the HAADF image of Fig. 7.8 (a) (marked by the white arrows). The corresponding STEM-EDXS measurements reveal that these regions are
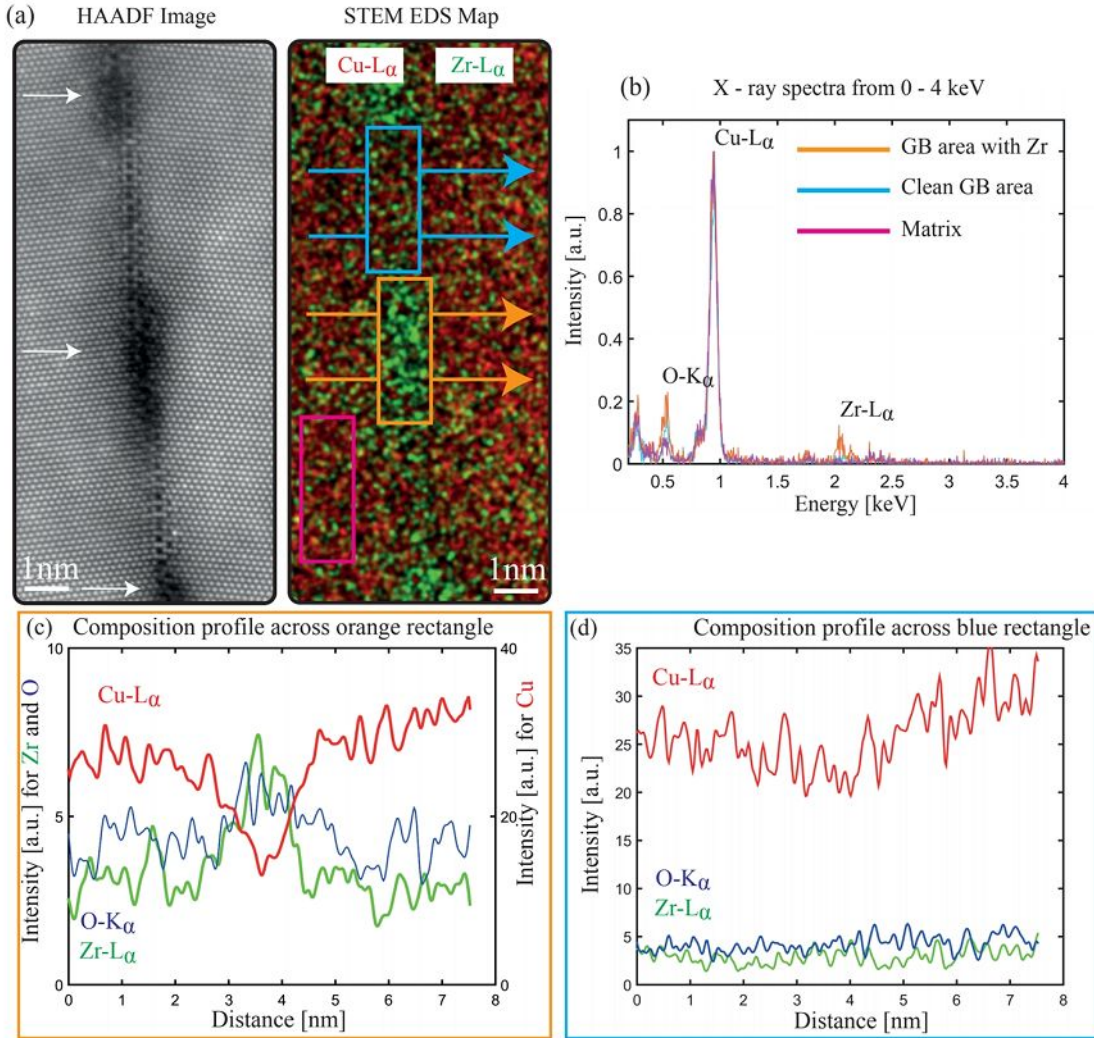
Fig. 7.8.: STEM and EDXS characterization of the Zr segregated zipper structure: (a) HAADF-STEM micrograph and STEM-EDXS map (Cu-K_α (red) and Zr-L_α (green)) of an asymmetric variant of the zipper structure showing Zr segregation to the GB steps. The colored boxes in the EDXS map indicate the positions where the spectra in (b) were taken from. The plot in (b) compares the X-ray spectra from the GB step, the GB between the steps and the grain. The arrows represent the concentration profiles in (c) and (d).

Zr and O rich, as can be seen from the corresponding X-ray spectrum extracted from the orange rectangle in Fig. 7.8 (b). The Zr signal disappears almost entirely at the symmetric GB facets (blue rectangle) and within the Cu matrix (magenta rectangle). This observation is further supported by two intensity profiles extracted across the GB and the GB step, as indicated by arrows. A drop in Cu signal at the GB step is observed, while both Zr and O intensities increase (Fig. refpic:fig5 (c)). The O intensity increase may be a result of oxidation of Zr in the GB step, but in view of the APT measurements on a fully Zr decorated GB shown in Fig. 7.10, a complete Zr-oxide formation is un-

likely. The detection of O in each location of the specimen indicates that the surface of the TEM specimen was oxidized. The large Zr rich regions are mainly located at the steps between symmetric segments, but also smaller Zr rich regions in the clean symmetric segments are observed rarely (seen also as black contrast), as illustrated in Fig. 7.9 (a) in the green rectangle. A $0.5\,nm$ wide dark spot can be seen in the middle of the clean symmetric facet, indicating that also here small amounts of Zr could be located in such confined regions. While the facets of the clean GB show a homogeneous length distribution, the facet length in the Zr segregated case varies between $1\,nm$ (first facet in Fig. 7.9 (a)) and $6\,nm$ (facet in the image center in the green box). This can either be induced by the Zr segregation or could also be due to the local GB curvature. Such a behavior was not observed for a clean GB, but the statistics on these observations are low. Furthermore, the steps differ in contrast with respect to each other, suggesting that the amount of Zr differs for each step.

Since the quantification of STEM-EDS data obtained under strong channeling conditions used here is limited, more precise information on the GB composition was obtained by APT shown in Fig. 7.10. As EBSD measurements were not successful, because of the remaining Zr film on top of the Cu, it is not known what kind of GB was investigated here. But it still gives very good and detailed information about the elemental distribution and the amount of Zr segregated to the GBs. To directly relate the GB structure and the chemistry, one need to do correlative TEM and APT measurements. The reconstruction in Fig. 7.10 (a) shows all Cu atoms as red and Zr atoms as green dots. Zr is segregated homogeneously along this GB and its accumulation can be better approximated in the concentration profile (see Fig. 7.10 (b)). In the corresponding mass spectrum, no significant amount of oxygen was found within the detection limit. It is concluded that pure Zr is located at the GB core and no intermetallic Cu-Zr phases or a Zr_xO_{1-x} were formed, as intended by the annealing treatment. The solute atomic excess of Zr at the GB was calculated following ref [153, 154] with an average of $2.76 \pm 0.24\,\frac{at}{nm^2}$. The absence of oxygen signal in the APT data supports that variations in the oxygen signal of the STEM-EDS data are mainly related to surface oxidation.

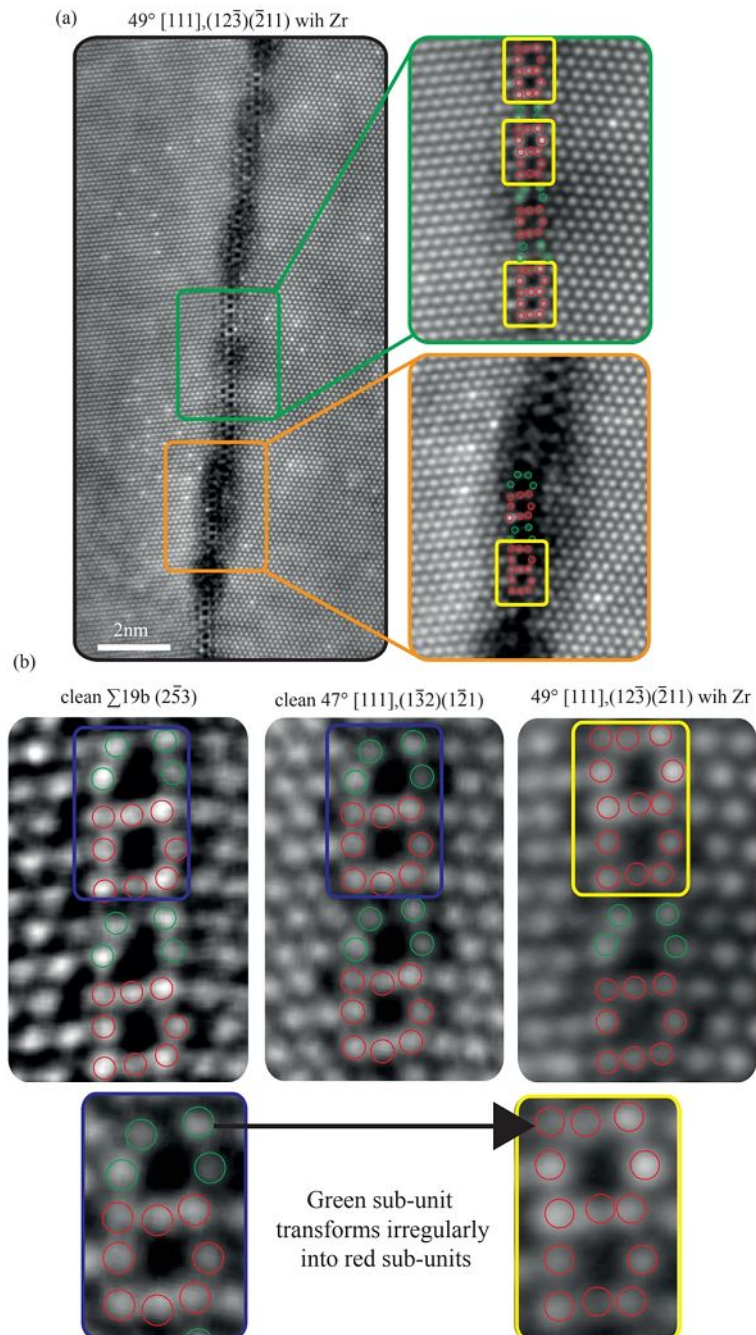Looking deeper into the atomic structure of the symmetric, Zr free appearing facets,

Fig. 7.9.: Zr-induced structural transitions at symmetric GB facets: (a) HAADF-STEM image of an asymmetric 49.2° [111], (12$\bar{3}$)\($\bar{2}$11) alloyed with Zr, showing dark contrast at all GB steps. The green and orange rectangle show two regions in higher magnification. The green box shows a symmetric facet of the GB. The red and green dots represent the structural sub-unit configuration. In the orange box the disordered structure of a step is shown. (b) HAADF-STEM image of the clean GBs (symmetric and asymmetric) (see also fig. 7.1). The blue windows marks one structural unit of the GB. Below, the structural units in the yellow, red and blue boxes are compared.

an influence of Zr on the structural sub-units can be observed. Such regions are marked by a green and orange rectangle (facet and step region) and its magnified views are illustrated as an inset in Fig. 7.9 (a)). The atomic structure of the Zr decorated steps (orange box) is strongly disordered (compared to the clean step from Fig. 7.4 (b)), which also explains the decrease in contrast despite the segregation of an atomic species with higher atomic number than Cu. In certain locations, the SU observed at clean symmetric and asymmetric GBs (Fig. 7.2 (a) and Fig. 7.4 (a)) appear to undergo slight structural transitions upon Zr segregation. Locations of these structural modifications are indicated by yellow rectangles in the insets of Fig. 7.9 (a). In contrast to the original SUs, the modified units are only composed of rectangular building blocks (red sub-units) leading to a disruption of the periodicity of GB structural units. In Fig. 7.9 (b), the structure of the clean symmetric and asymmetric GB are compared with the Zr influenced symmetric facet. The blue and yellow boxes show the SU of the clean and Zr induced GBs. On the bottom of Fig. 7.9 (b) the structural transition is visualized. The transformation can be described by adding one atomic column to the green, trapezoidal SU, which transforms it into the red, rectangular SU. This seems to occur without any periodicity/ordering along the GB facets so that the overall periodicity and order is decreased.

7.3. Discussion

In the first part of this discussion the complexity of the two $\Sigma 19b$ GBs, investigated here, will be discussed with respect to the SU model. To the authors knowledge, there are no other experimental studies on the atomic structure of [111] tilt GBs in fcc metals, but only theoretical calculations, for example from Frost et al. and Wang et al. [20, 21] . Afterwards, the influence of Ta and Zr on the atomic SU of the GBs is discussed in detail. Furthermore, the results are compared with recent studies on similar material systems and conclusions on how this is related to the microstructure stabilization of nanocrystalline Cu are drawn.
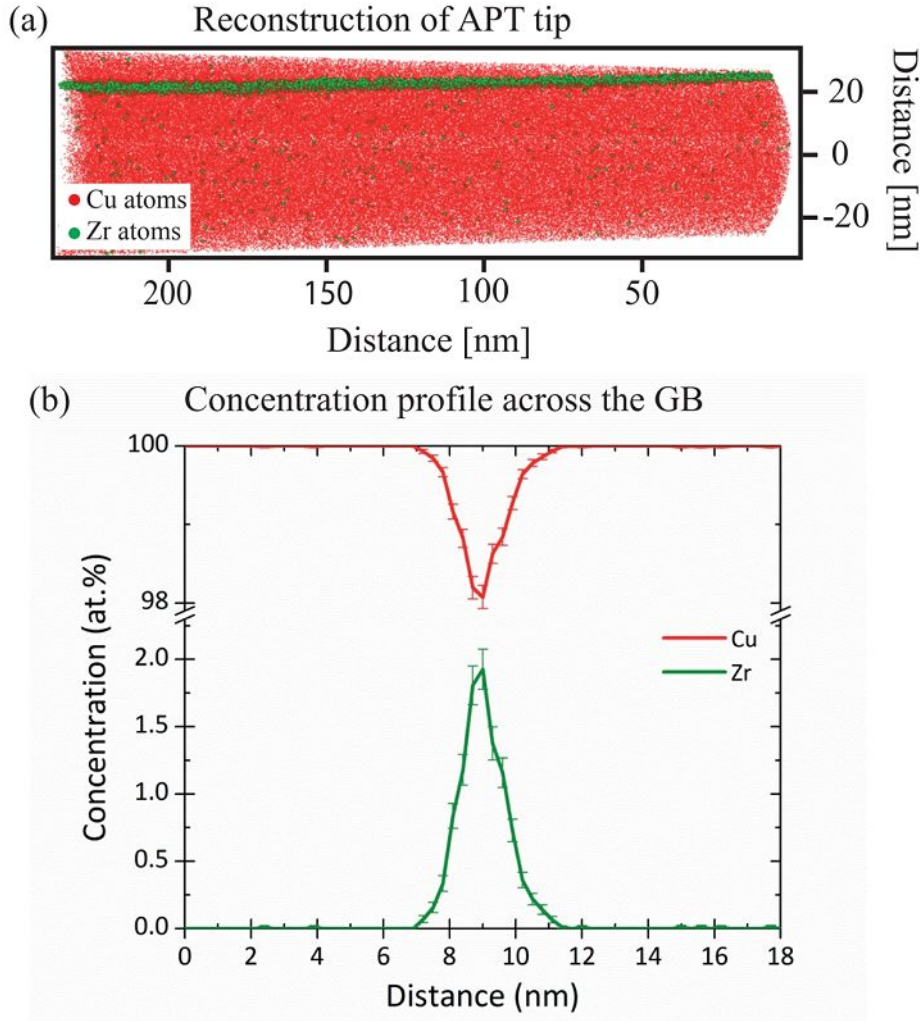
Fig. 7.10.: APT characterization of a Zr enriched GB: (a) Reconstructed specimen showing Cu atoms in red and Zr atoms in green. A concentration profile of across the GB, showing the concentration of Cu in red and Zr in green, is presented in (b).

7.3.1. Pure $\Sigma 19b$ [111] tilt GB structures

Both experimentally observed $\Sigma 19b$ GBs exhibit the same grain misorientation and only differ in habit orientation leading to a significant change in their structural sub-units. In total, 4 different structural sub-units, S,T,R and P, could be assigned to fully describe the structure of the GBs. Originally it was proposed that each GB with a specific misorientation can be constructed by the structural units of two delimiting boundaries (with respect to misorientation) [38]. This model is not applicable to the present GBs even though we do not know the SU from the delimiting GBs. Since a delimiting boundary is supposed to consist of only one SU [34], according to the SU

model there exist only two SU, e.g. one from the 0° and on from the 90° GB, in order to build up other GBs (as it is done for the $\Sigma 5\,[001]$) [34]. But the two $\Sigma 19b$ GBs here already revealed 4 different SUs so that two delimiting boundaries would be not enough to describe both $\Sigma 19b$ simultaneously. Therefore, the extended model by Han et al. [34] could be considered, since it also takes meta stable GB structures as possible delimiting GBs into account and thus the number of available SUs is increased. This is not investigated in great detail nowadays so that it cannot be discussed further. Deviations from the SU model have been also found by other theoretical studies in different symmetric tilt GBs [34, 39, 40].

[111] tilt GBs in fcc metals are much less studied than [001] or [011] tilt boundaries, except the $\Sigma 3$ twin boundary. To our knowledge, only two theoretical studies exit reporting on the structure of several of the [111] tilt GBs [20, 21]. Frost et al. estimated the structure and properties of different low Σ GBs by a simple hard sphere model [36]. Comparing their predicted structures to the ones observed in experiment here reveals a fundamental difference in the structural units of both $\Sigma 19b$ boundaries. This indicates that the hard sphere model is not capable of predicting the structure of [111] tilt GB. A similar conclusion is found by comparing the experimentally obtained structures here with the calculated ones of Wang et al. [21]. They describe the structure of the $\Sigma 19b\,(2\bar{5}3)$ with the SU model notation $|\,EFF\cdot EFF\cdot EFF\,|$ by using the $\Sigma 1\,(1\bar{1}0)$ and $\Sigma 3\,(121)$ as delimiting GBs. E represents a special unit of the $\Sigma 1$ and F of the $\Sigma 3$ boundary. It is obvious that their notation/structure does not fit to the experimental observations in the present study $|\,ST\cdot ST\,|$ and $|\,RP\cdot \text{Яꟼ}\cdot RP\cdot \text{Яꟼ}\,|$.

7.3.2. Cu-Ta system

The formation of spherical, nanometer sized Ta-rich particles is only observed at or near GBs, leading to the conclusion that GB diffusion is the dominant process, while diffusion into the grains is not possible at this temperature. This is not surprising since Ta diffusion tends to zero in bulk Cu below $1000°C$ and the annealing treatment here was performed at $600°C$ [123]. Apparently, diffusion of Ta along the entire $\sim 1\,\mu m$ long Cu tilt GBs occurred during the heat treatment for $24\,h$ at $600°C$. Ta dis-

tributes along the GBs during annealing, but does not diffuse into the grains since the bulk solubility of Ta in Cu is essentially zero below $\sim 1038°C$ [122]. During cooling, the solubility of Ta at the GB decreases and excess Ta atoms accumulate to form spherical particles. In total, three steps are observed and the GB moved in total $\sim 18\,nm$, which would correspond to an average velocity of $2 \cdot 10^{-4}\,\frac{nm}{s}$ to the right side (considering a constant movement for $24\,h$). It can be assumed that while Ta homogeneously distributes along the GB it lowers its mobility at $600°C$ due to the solute drag effect [155]. During cooling, Ta precipitates out at the GB and the mobility of the Ta lean parts increases. It seems that the GB groove at the film surface acts as a step nucleation site first promoting the motion of the upper part of the GB. Subsequently, this part of the boundary starts migrating and sweeps across the Ta precipitates and gets pinned at its backside. The exerted backstress of the particle impedes GB migration. This pinning of GBs by particles was discussed in theoretical studies before and is known as Zener pinning [55]. The Zener model describes grain growth of a particle containing matrix, where the driving force for GB migration is counteracted by a pinning pressure between the surface of the particle and the GB plane [54, 114]. Depending on the direction of GB migration and the position of the particles, they can either exert an attractive or repelling force on the GB. It is proposed that the particles induce a local curvature in the GB, which then leads to a driving force towards the particle. This is schematically depicted in Fig. 7.11 (a), adapted from [114]. Applying this force balance to our experimental observations allows to estimate the fraction of local pinning force on the GB for a given particle radius r, even though the local surface tension γ between GB and particle is not known:

$$F_z = 2\pi\, r\gamma \sin(\theta) \cos(\theta) \tag{7.1}$$

In equation 7.1, θ defines the contact angle between the average surface of the GB plane and the point where it crosses the particle [54]. The force on the GB is at its maximum (attracting or repelling) for an angle of $45°$. In the experimental image, the GB does not follow a smooth curvature but appears discontinuous and deviates strongly from the exact model (see Fig. 7.11 on the right the white line). This makes it difficult to precisely determine the correct contact angle. But here, two variants can be calculated and it can be assumed that the real value lies in between these two. First,

the angle between the particle center and the kink (marked in red in the figure) can be measured to an angle of $\sim 45°$, which means that maximum force is pulling on the GB in the observed configuration. Secondly, one can measure from the particle center to the point of contact (marked in green) an angle of $\sim 25°$, which leads therefore to $\sim 77\%$ of the maximum force. Since the GB moved to the right side considering the GB steps from Fig. 7.5(e), the particle is exerting a repelling pinning force on the GB at this moment. A single nano-sized particle is in principle not enough to pin a whole GB, but with a higher particle density the Zener model predicts a limited grain size.
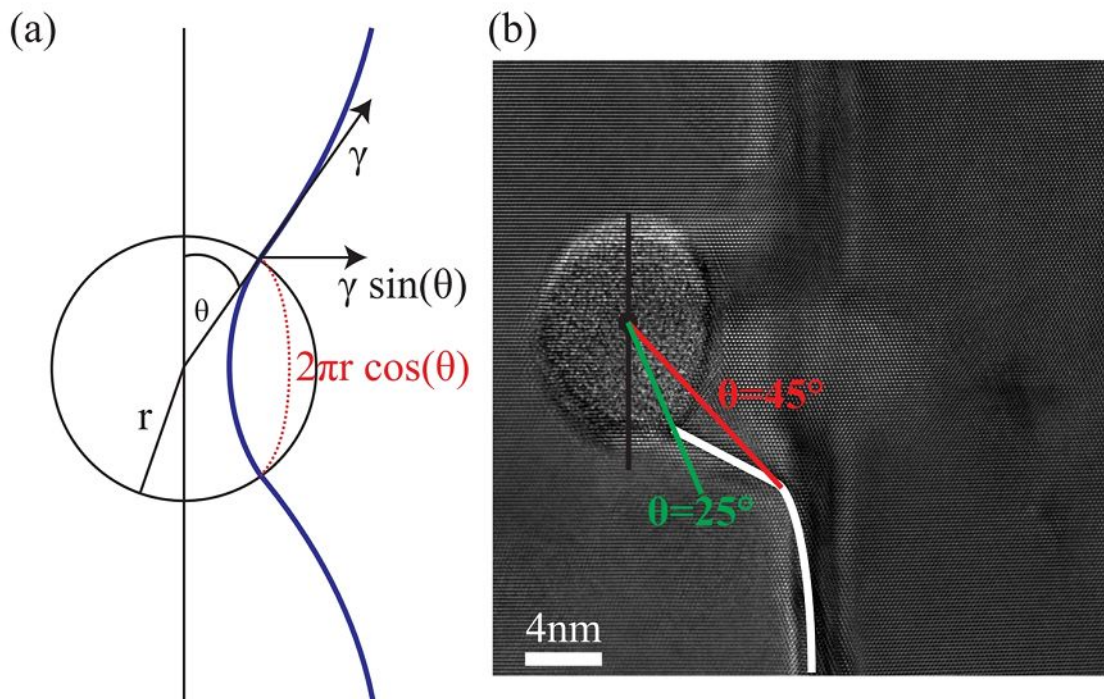

Fig. 7.11.: Comparison of the Zener model and experimental TEM image: Sketch of the Zener pinning adapted from ref. [114] (a) in comparison with an experimental HRTEM image (b).

The atomic resolution images clearly reveal the Zener effect of Ta particles at Cu GBs. The observations are in excellent agreement with theoretical studies [55, 123, 156, 157] and the proposed Zener model [54, 114]. Hence, the segregation of Ta to Cu GBs and the associated GB pinning by Ta particles can be associated to the kinetic approach for stabilizing microstructure.

7.3.3. Cu–Zr system

A recent study by Khalajhedayati et al. shows that adding Zr not only leads to a stabilization of the microstructure of nanocrystalline Cu-Zr alloys, but also increases the strength while conserving partly the ductility of polycrystalline Cu [120]. In their study, they presented that either AIFs form at the GB or that Zr homogeneously decorates the GB, depending on the processing route of the material. They propose that the AIFs reduce the GB mobility and ductility is partly retained, while homogeneous Zr decoration only reduces GB mobility and leads to embrittlement. However, direct atomic scale correlation of the presence and effects of Zr on the GB structure (with EDXS for example), also compared to clean GBs in their material, are missing in the study [120]. In a different publication, however, they presented some EDXS analysis in lower magnification in similar samples and showed a slightly inhomogeneous Zr segregation and a Zr concentration as high as $\sim 7\,at.\%$ [158]. Another study of Pan et al. [121] deals with atomistic calculations of the Zr segregation behavior at different GBs considering several Zr concentrations and annealing temperatures. They found that AIF formation depends on the Zr concentration, the GB structure and annealing temperature. Low Zr concentration and low annealing temperature lead more to defined segregation and a crystalline GB structure, while increasing both leads to amorphization. The concentration and temperature for the transition also depends strongly on the GB structure. In the present study, considering the two different $\Sigma 19b$ variants observed, three different phenomena can be observed:

1. The $\Sigma 19b\,(1\bar{8}7)$ reveals a homogeneous decoration of Zr, which induces a high degree of structural disorder at the GB core, but still remaining partly the crystalline structure of the original GB. The observed segregation layer at the GB was found to be pure Zr with an average solute atomic excess of $2.52 \pm 0.24\,\frac{at}{nm^2}$ by APT. The structural disorder indicates that in addition to Zr segregation, the grain boundary energy is further reduced by an increase in the GB entropy. This observation supports the two studies of Khalajhedayati et al. [120] and Pan et al. [121], since also a strong disordering occurs. Furthermore, such a disordering of the GB by Zr will also have a strong effect on the plastic behavior, in particular the dislocation nucleation, as was shown by molecular dynamics simulations

[159]. The overall picture on the results can be interpreted as a reduction of the GB free energy by solute segregation and disordering of the atomic structure [15, 17].

2. An asymmetric variant of the $\Sigma 19b\,(2\bar{5}3)$ shows high Zr segregation to GB steps. The steps are incorporated to compensate for the asymmetric inclination of the GB and it was shown that the steps Burgers vector is $[01\bar{1}]$ with pure edge character. Zr was observed to preferentially segregate to these GB steps instead of decorating the planar symmetric GB segments as was found in the pearl structure. Similar to the planar GB, the core structure of the step appears more disordered upon Zr segregation. Such an anomalous segregation behavior was revealed at faceted GBs in silicon and was associated to the core structure and strain of the GB facet junctions [92]. An indication of minor Zr segregation to the symmetric facets is found indirectly by the occurrence of partially disordered structural units. These observations indicate that Zr segregation is strongly affected by GB topology.

3. As shown in Fig. 7.9, minor structural transitions at the symmetric facets are observed. The green sub-unit, or T unit, transforms irregularly to the red, S sub-unit leading to a disruption of the periodicity of the GB structural unit arrangement. This chemically-induced effect is assumed to be related to Zr incorporation in the GB. It implies that different degrees of disordering can be introduced in a GB depending on Zr concentration, as also suggested by atomistic simulations [121]. The SU might transform due to local chemical changes and rearrange in order to minimize the GB free energy.

These atomic scale observations directly confirm the atomistic origins of Zr segregation to different [111] tilt GBs in Cu. Overall, Zr induces disordering of the structural units as well as the core structure of GB steps, strongly affecting the GB properties. The preferential segregation of Zr to GB steps can have important implications in nc materials since their nano-scale grain size implies a high density of such GB defects [120]. The observations for Zr indicate that it contributes to the microstructure stabilization through the above introduced thermodynamic approach, which is described by a reduced GB energy and thus, a lower driving force for grain growth.

7.4. Conclusion

In this paper, a systematic study of the atomic scale GB structure and related segregation-induced effects by Ta and Zr on the same GB are investigated. The chosen GBs are two symmetric $\Sigma 19b$ and its slightly asymmetric variants. The employed high resolution microscopy techniques revealed the following conclusions:

1. The two symmetric $\Sigma 19b$ exhibit very complex structures with different structural sub-units and periodicity and cannot be described by the structural unit model. Slightly asymmetric variants of the two GBs reveal a different behavior in compensating the asymmetry. While the $\Sigma 19b, (2\bar{5}3)$ includes steps into the structure, the $\Sigma 19b, (1\bar{8}7)$ includes additional structural sub-units in a periodic manner.

2. Ta segregation was achieved by GB diffusion during an annealing treatment at $600°C$. The formation of nanometer sized Ta precipitates is observed at or close to the GBs. One specific Ta precipitate was found to pin the GB via Zener Pinning by locally distorting the GB plane, which exerts an attractive force on the GB.

3. Zr is found to segregate to the GBs in different ways, depending on the local atomic structure of the GB itself. For an asymmetric variation of the $\Sigma 19b, (1\bar{8}7)$, a homogeneous formation of a pure Zr layer was observed. The presence of the Zr induced a higher disorder in the GB core and transformed some structural units, by distorting them or removing atomic columns. On an unknown GB with homogeneous Zr segregation, a Zr concentration of $\sim 1.6\,at.\%$ was measured with APT. The asymmetric variation of the $\Sigma 19b, (2\bar{5}3)$, revealed inhomogeneous Zr segregation to its steps, while the symmetric facets are mainly free of Zr. The segregated steps show a much higher disorder compared to the clean steps. Furthermore, small structural transitions of sub-units are observed inhomogeneously along the facets and close to the steps.

4. Interpreting the results with respect to the microstructure stabilization of non-crystalline materials it can be concluded that Ta stabilizes via the kinetic ap-

proach. This study supports the Zener pinning by Ta particles. The stabilization mechanism of Zr, however, can be explained by the thermodynamic approach. Due to the Zr induced disorder and structural transitions, the GB free energy is lowered. With that the driving force for GB migration is lowered and the microstructure is more stable.

8. Sulfur-induced embrittlement of high-purity, polycristalline Copper

This chapter investigates the atomistic mechanisms of the embrittlement effect of Sulfur in high purity Cu. The different materials come from different recycling steps of the company Brixlegg and represent a real life engineering material. The GBs in this material are random low and high angle GBs instead of being low Σ symmetrical tilt GBs (as in the previous chapters), which is usually the case in applied materials in daily life. Therefore, it is also important to extend the microstructural investigations to these material classes. In this study, macroscopic investigations are coupled with high resolution (S)TEM techniques and APT in order to determine the origin of sulfur in random GBs. Three different alloys are investigated, with different sulfur concentrations; S14 (14ppm), S27 (27ppm) and S7920 (7920 ppm). This chapter is based on the publication in the journal **Acta Materialia** [18].

8.1. Introduction

In this study, we establish a connection between the mechanical properties, with a focus on embrittlement tendency, and a detailed microstructural characterization of two high purity Cu alloys with 14 and 27 at. ppm S and a Cu-S alloy with a 7920 at. ppm S concentration. Considering the low solubility of S in Cu and results from former studies, we focus on a high resolution observation of relevant microstructural features such as random GBs. The aim is to explore the formation of Cu-sulfides and GB composition to discover the microstructural based origins of S-induced embrittle-

ment in Cu. The global grain structure of the alloys is characterized by SEM and EBSD. Specimen for TEM and APT were extracted in the vicinity of GBs by FIB. In the high purity Cu alloys (14 and 27 ppm S) neither sulphide precipitates nor S enrichment at GBs was found by TEM techniques and APT. Even in an annealed sample with 27 ppm S, no Cu-sulfide formation or increased S concentration at GBs was observed. The formation of nano- and micro scale Cu_2S particles is confirmed by electron diffraction and analytical STEM in the S-rich sample with 7920 ppm S. The impact of S on the macroscopic mechanical properties and the influence on the grain structure are discussed in detail.

8.2. Results

8.2.1. Tensile Tests

The mechanical properties of the three alloys are established by macro-sized tensile tests. The corresponding stress-strain curves of sample S14, S27 and S7920 tested at $20°C$, $200°C$ and $400°C$ with a strain rate of $10^{-3}\,s^{-1}$ are presented in Figure 8.1 (a)-(c). The UTS of S7920 exceeds with $190\,MPa$ at RT and $150\,MPa$ at $200°C$ both S14, with 130 and $100\,MPa$, and S27, with 160 and $100\,MPa$, respectively. At $400°C$ all samples are similar with UTS of $60 - 80\,MPa$. The ductility drops significantly with increasing S content and with increasing temperature. A S increase from 14 ppm to 27 ppm leads to a reduction in ductility of 28% at RT and 66% at $400°C$. Between 14 and 7920 ppm S the reduction in strain to failure amounts to 56% at RT and 63% at $400°C$. In literature, this temperature effect is referred to intermediate temperature embrittlement due to intergranular failure [129].

8.2.2. Macro-/Microstructure

OLM studies show no differences of the global surfaces of S14 and S27 (see Fig. 8.2 (a)-(c)). Both appear smooth and show a few etch pits or voids, which are most likely stemming from sample preparation and casting. In S7920 a dendritic microstructure
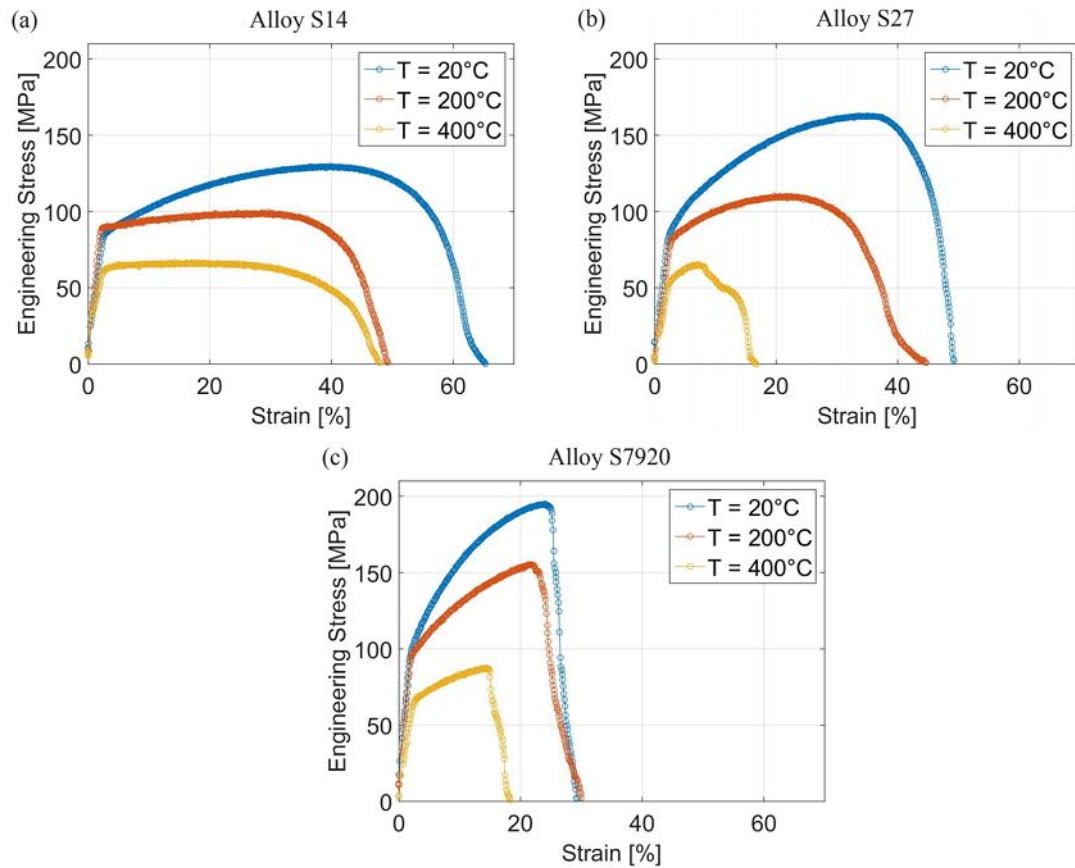
Fig. 8.1.: Tensile testing of the Cu-alloys: Stress-strain curves of the three Cu alloys at room temperature (blue), at 200° (red) and 400° (yellow) at a strain rate of $10^{-3}\,s^{-1}$.
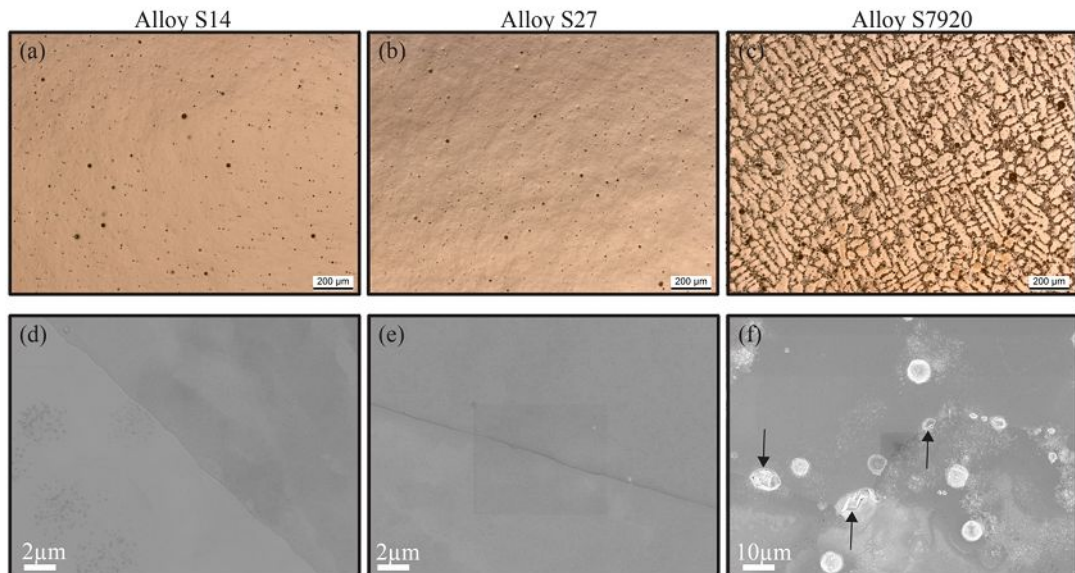

Fig. 8.2.: OLM and SEM characterization: (a)-(c) OLM images of the electro-polished surfaces of the three copper alloys containing 14 ppm (a), 27 ppm (b) and 7920 ppm (c) sulfur impurities. In (d)-(f) the accompanying SEM micrographs (secondary electron contrast) of the electro-polished surface from the three alloys are presented.

is found, where the dendrites are mainly free of precipitates, whereas in the interdendritic region large spherical precipitates have formed as demonstrated in the inset of Fig. 8.2 (c).

A closer look into the microstructure using SEM shows a particle free surface and slightly curved GBs for S14 and S27 as illustrated in Fig. 8.2 (d) and (e)). From these observations, no indication for precipitate formation in S14 and S27 is detected. The strongly increased S concentration of S7920 leads to the formation of $10 \mu m$ large precipitates (see Fig. 8.2 (f)). The precipitates are located in the interdendritic regions and it seems that they are surrounded by smaller precipitates. The shape of precipitates at GBs is mostly lenticular while the precipitates within the grains have a spherical shape. The dendritic regions show particle-free surfaces comparable to S14 and S27, but also a much rougher surface. This increase in surface roughness most probably results from electro-polishing with different etching rates for particles and matrix. The precipitates are frequently disconnected from the GB and appear fractured at the phase boundaries as indicated by the arrows in Fig. 8.2 (f). Using EPMA-WDXS the precipitates are identified as copper-sulfides. The same technique was used in S14 and S27, but the lateral resolution of EPMA is too low to resolve a sub-micron sulfides.

SEM-EBSD was used to obtain information about the grain structure, size distribution and the GB character and on the other hand to select GBs for TEM investigations (see Fig. 8.3). The grain size in all three alloys is $2-4 \, mm$ and mostly random low and high angle GBs are present, without a common zone axis for both grains. Furthermore, the grain structure appears slightly textured. The EBSD map of S7920 reveals a curvy nature of the GBs resulting from the dendritic structure, which is apparent in the other two samples. Thus, it seems that the GBs follow the interdendritic regions.

8.2.3. Nanostructure and chemistry

In order to investigate the segregation and precipitation of S at GBs we prepared several TEM specimens containing different GBs of each alloy. We investigated general GBs, including HAGBs and LAGBs with different misorientations and random
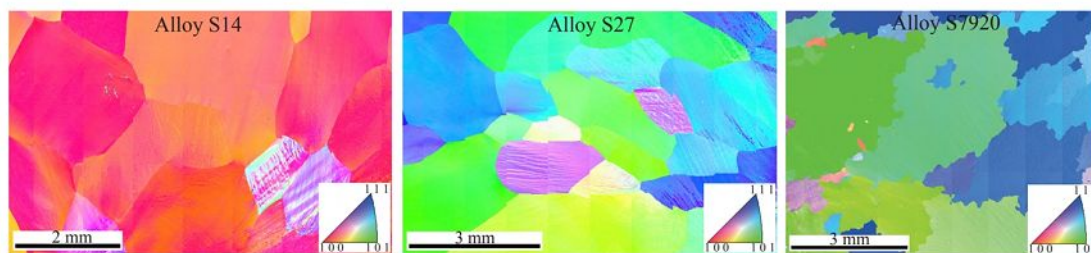
Fig. 8.3.: EBSD characterization: EBSD scans of the three alloys with a step size of $1\,\mu m$. Each scan consists out of several single EBSD scans, which were finally aligned for a single image. The insets show the corresponding inverse pole figures. Color code: [100] red, [101] green, [111] blue.

GB plane inclinations. Even though segregation to LAGBs is unlikely and rarely observed, there are examples in literature which showed different results for S in Fe and for boron and carbon in ferrite and martensite [9, 160]. For example, Ainslie et al. [9] showed that S can induce a formation of dislocation networks in α-iron and postulate that S segregation to dislocation cores is possible. Therefore, we investigated the compositions of LAGBs and HAGBs with different GB character to compensate for a possible anisotropic segregations [15]. In the following we will only show representative results of one GB per alloy, a HAGB in alloy S14 and S7920 and a LAGB in alloy S27.

Overview and atomically resolved STEM images of random GBs for each of the three alloys are illustrated in Fig. 8.4. Due to the random orientation relationship of the two adjacent grains, the complete structure of the GBs cannot be resolved since only one grain can be tilted to a zone axis orientation at a time. The GB in S14 is a high angle GB with one grain in [110] zone axis orientation and the GB plane slightly inclined with respect to the electron beam (see Fig. 8.4 (a)). We do not observe any structural changes of the GB or the presence of a second phase induced by S. The TEM specimen prepared from S27 (Fig. 8.4 (b)) shows a low angle GB with one grain in [112] zone axis orientation and the second grain with small twist and tilt components with respect to the other grain. The GB is composed of regularly spaced dislocations at every fifth lattice plane in order to compensate for a 6° misorientation of both grains. From Fig. 8.4 (a) and (b) it is difficult to draw any structural conclusions about the segregation of S to the GBs, but it can be established that no nanoscale sulfides are formed at such GBs.

105

With STEM-EELS and EDXS, no S enrichment is found at the GBs in S14 and S27, indicating that there is no clear sign for S segregation within the detection limits of these techniques. Exemplary, the $S-K_\alpha$ STEM-EDXS map at the GB from S27 in Fig. 8.4 (b) is analyzed by the spatial difference method (see Fig. 8.5). In (a), the $S-K_\alpha$ elemental map is overlaid with the HAADF image of the GB. The red, black and green rectangles indicate the area from where the spectra in (b) were taken. The EDXS spectra of the two grains (green and red) and the GB (black) show no $S-K_\alpha$ peak or it is at least within the noise level. Therefore we plotted a differential spectrum by averaging the spectra of the two grains and subtracting the spectrum of the GB. But still no $S-K_\alpha$ peak is visible, indicating that no S is present at the GB within the detection limits for EDXS. We also performed STEM-EELS measurements at the same GB. Again, no S enrichment could be measured, but only a thickness change between the grains and the boundary from $55\,nm$ in the grains to $35\,nm$ at the GB. These findings are further supported by APT, a technique that provides highest chemical sensitivity since it relies on mass spectroscopy [72, 161]. Fig. 8.6 presents an APT measurement obtained from a GB of S27 (the one shown in Fig. 8.4 (b)). Both, the TKD map (Fig. 8.6 (a)) and the detector density maps (Fig. 8.6 (c)), confirm the presence of the GB within the apex of the needle shaped specimen. No distinct S segregation is observed at the GB, as shown in the 3D atom map of Fig. 8.6 (b).

Here, both O and S atoms are highlighted as black spheres. The time-of-flight of S and O ions are similar and hence difficult to differentiate. As we can see from the mass spectrum in Fig. 8.7 (a), the possible ionic species containing S are S^{2+} and S^+. Zoom-in views of the mass spectra sections for these two ions, colored in light blue and light green respectively (see Fig. 8.7 (b)). According to the natural abundance of the S and O [161], there is a strong overlap between the mass peaks of S^{2+} (marked in red) with that of O^+ (marked in cyan). The mass peaks of S^+ (marked in black) also extensively overlap with the main mass peaks of O^{2+} (marked in green). Comparing the probabilities of different peaks being associated to either of the two elements, listed in Table 8.1, we may distinguish S from O through the peaks at 17 Da and 34 Da, since the vast majority of the ions in these two peaks should belong to S^{2+} and S^+ respectively. Considering these two peaks are minor peaks, we applied here the methodology outlined in reference [162], whereby additional information from the single-particle detector
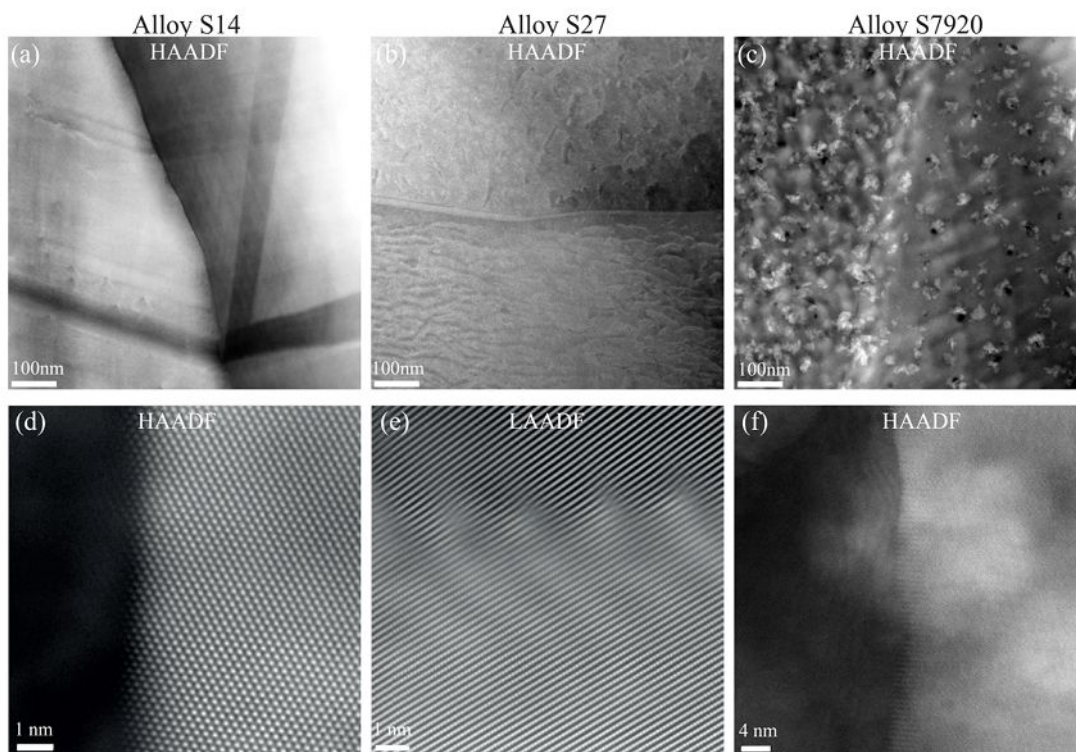
Fig. 8.4.: High resolution STEM investigation of GBs from the alloys]: (a)-(c) Overview HAADF-STEM images of random GBs from all three alloys. (d)-(f) High resolution STEM resolving the GB morphology.

is used to discriminate between ions detected individually (single detection events) and ions detected as part of a burst of ions emitted by the specimen (multiple detection event). It proved to be an efficient way to observe the minor peaks covered by the background in the overall mass spectrum. As shown in Fig. 8.7 (a), the mass spectrum colored in black corresponds to single detection events while the red is for multiple detection events. As we can see that commonly the background consists of mostly single detection events [162], therefore, from the mass spectrum for multiple events, some minor peaks may be observed. Here, there are no clear peaks at 17 Da and 34 Da in both spectra, which means that the S content is very limited and the proportion of S ions in the peak 16 Da and 32 Da is also limited. The two peaks mostly consist of O ions. Thus, most black spheres shown in the 3D atom map (Fig. 8.6 (b)) represent O atoms at the surface of the specimen which may originate from adsorbed O on the specimen surface during sample transfer in air.

In addition, no precipitates are found at these GBs or within the grains of S14 and S27 with TEM and APT. In the discussion section below, we will discuss the detection
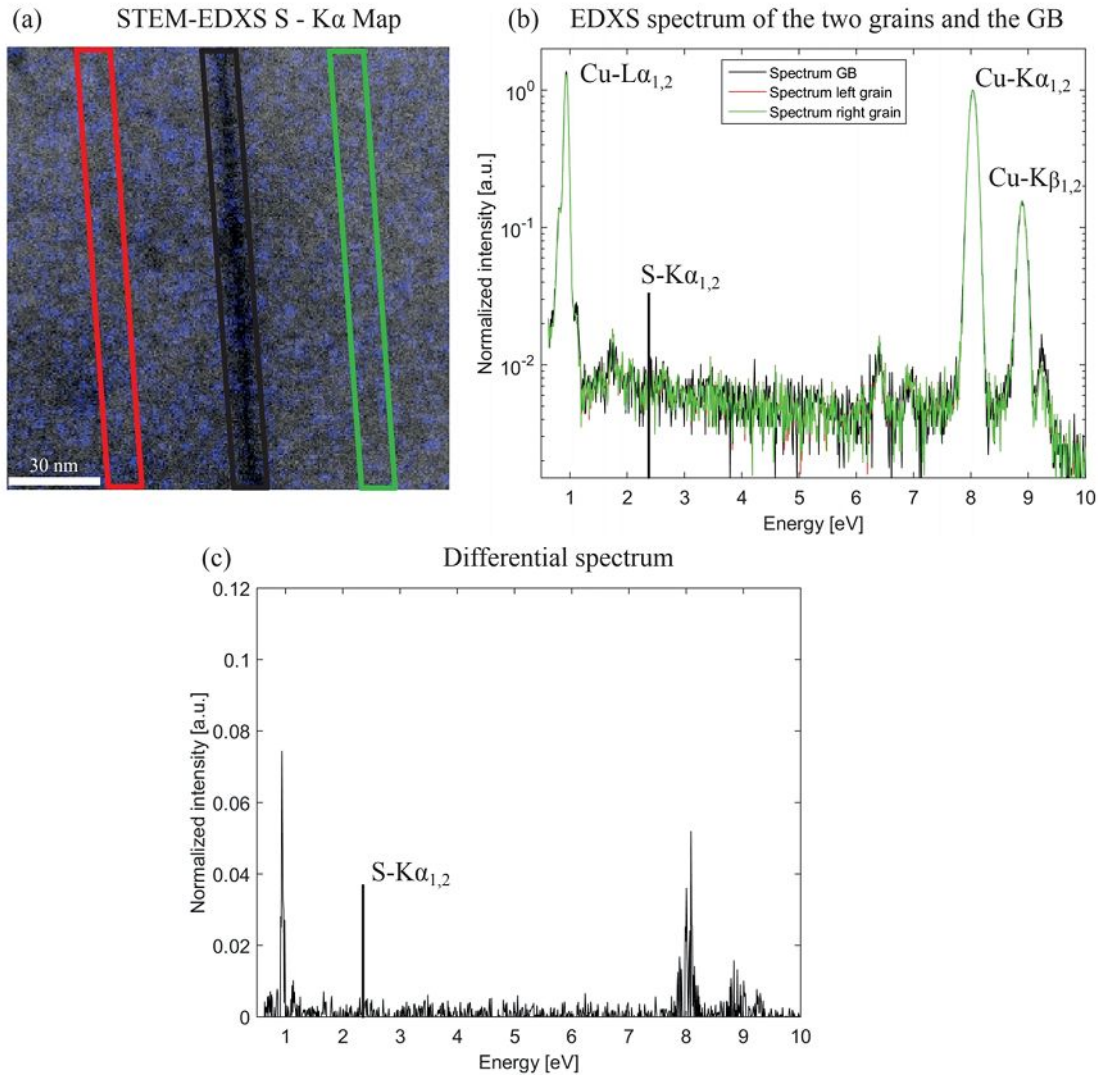
(a) STEM-EDXS S - Kα Map

(b) EDXS spectrum of the two grains and the GB

(c) Differential spectrum

Fig. 8.5.: EDXS of a GB from alloy S27: (a) shows the annular dark field image of the STEM-EDXS area containing a GB and overlaid with the elemental S map. (b) shows three EDXS spectra belonging to the two grains and one to the GB as indicated by the rectangles in (a). (c) shows a differential spectrum governed by subtracting the average spectrum from the grains from the grain boundary spectrum.

limits of EELS and EDXS with respect to S in more detail.

From S7920, two TEM specimens were cut out of the sample with a focused ion beam. Conventional sample preparation was not successful since the copper sulfides drop out of the samples during electro - polishing. The first specimen was taken from a GB region between two of the large precipitates of Fig. 8.3 (c), named $S7920_1$ here. The second specimen was directly extracted from one of the large precipitates located at a GB and is named $S7920_2$. STEM imaging in $S7920_1$ shows precipitates with diameters

Table 8.1.: Natural abundances (%) of different S and O isotopes [163] and molecular ions.

DA	16	16.5	17	18	
O	$^{16}O^+$	–	$^{17}O^+$	$^{18}O^+$	
%	99.757	–	0.038	0.205	
S	$^{32}S^{2+}$	$^{33}S^{2+}$	$^{34}S^{2+}$	$^{36}S^{2+}$	
%	94.99	0.75	4.25	0.01	

DA	32	33	34	35	36
O	$(2^{16}O)^+$	$(^{16}O^{17}O)^+$	$(^{16}O^{18}O)^+$ $(2^{17}O)^+$	$(^{17}O^{18}O)^+$	$(2^{18}O)^+$
%	99.515	0.076	0.409	0.0002	0.0004
S	$^{32}S^+$	$^{33}S^+$	$^{34}S^+$	–	$^{36}S^+$
%	94.99	0.75	4.25	–	0.01
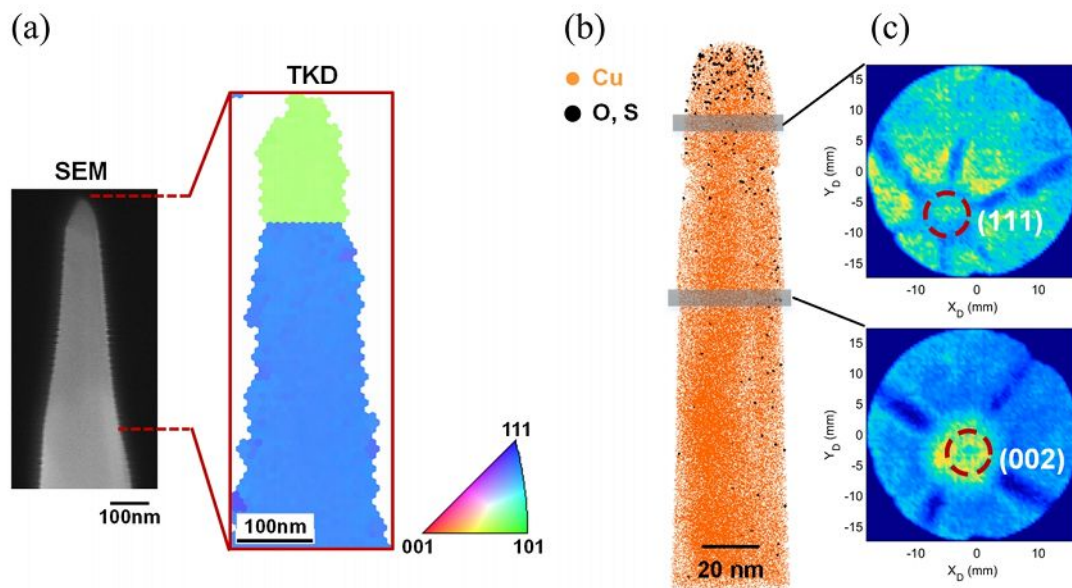
Fig. 8.6.: APT investigation of a GB from alloy S27: (a) SEM image and corresponding TKD map of an APT specimen fabricated from the grain boundary of S27 (from Fig. 8.4 (b)). (b) Corresponding APT measurement (LEAP 3000X HR) with detector hit maps from the two grains. Here, small orange dots mark Cu atoms and big black dots mark the O and/or S atoms.

ranging from ~$5 - 50\,nm$ within the grains and at the GB (see Fig. 8.4 (c)). At high resolution (Fig. 8.4 (f)), the structure of the precipitates cannot be resolved, because they are not oriented with respect to the matrix. In Fig. 8.8 (a) and (b), STEM-EDXS
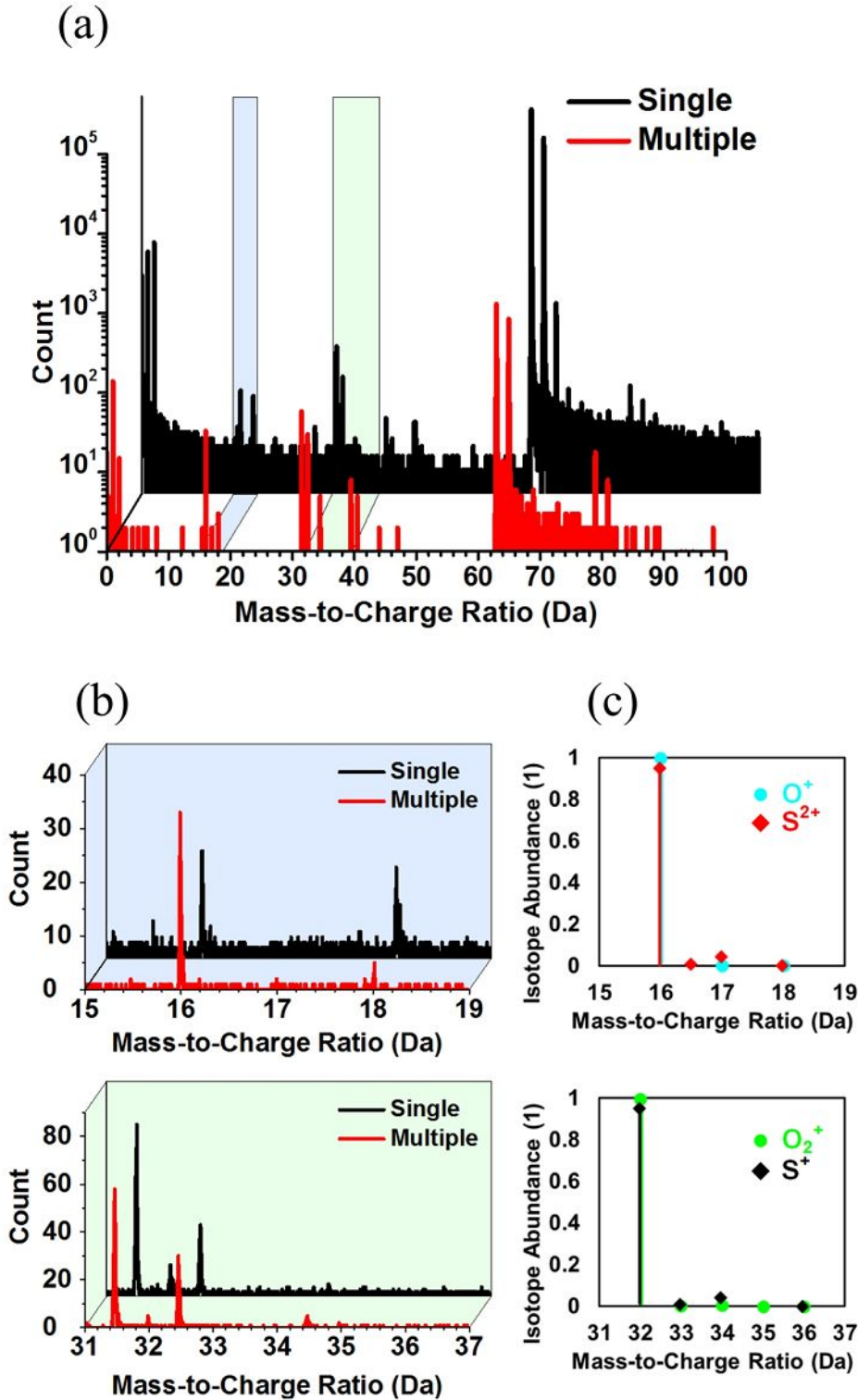
Fig. 8.7.: Mass spectra and natural abundance of the corresponding isotopes of the APT measurement: (a) Separate mass spectrum for single detection events and multiple detection events. (b) A zoom-in view of the section from 15 Da to 19 Da and 31 Da to 37 Da. For comparison, the natural abundance of different O^+ (cyan), S^{2+} (red), O^{2+} (green) and S^+ (black) isotopes are shown on the right side in (b). As one can see, all possible ions of O and S overlap strongly.

maps of the $S - K_\alpha$ signal are overlaid on the corresponding images of Fig 8.4 (c). It clearly confirms that the small precipitates are copper sulfides while no S enrichment at the GB can be detected between these particles. This is demonstrated with the help of the two EDXS spectra, taken from the small particle and a part of the GB as indicated by the blue circle and the red rectangle in Fig. 8.8 (b). In the spectrum, the $S - K_\alpha$ peak appears only in the particle and not at the GB. This implies that none of the alloys reveals S GB segregation or that the S concentration is below the detection limit of STEM-EDXS.
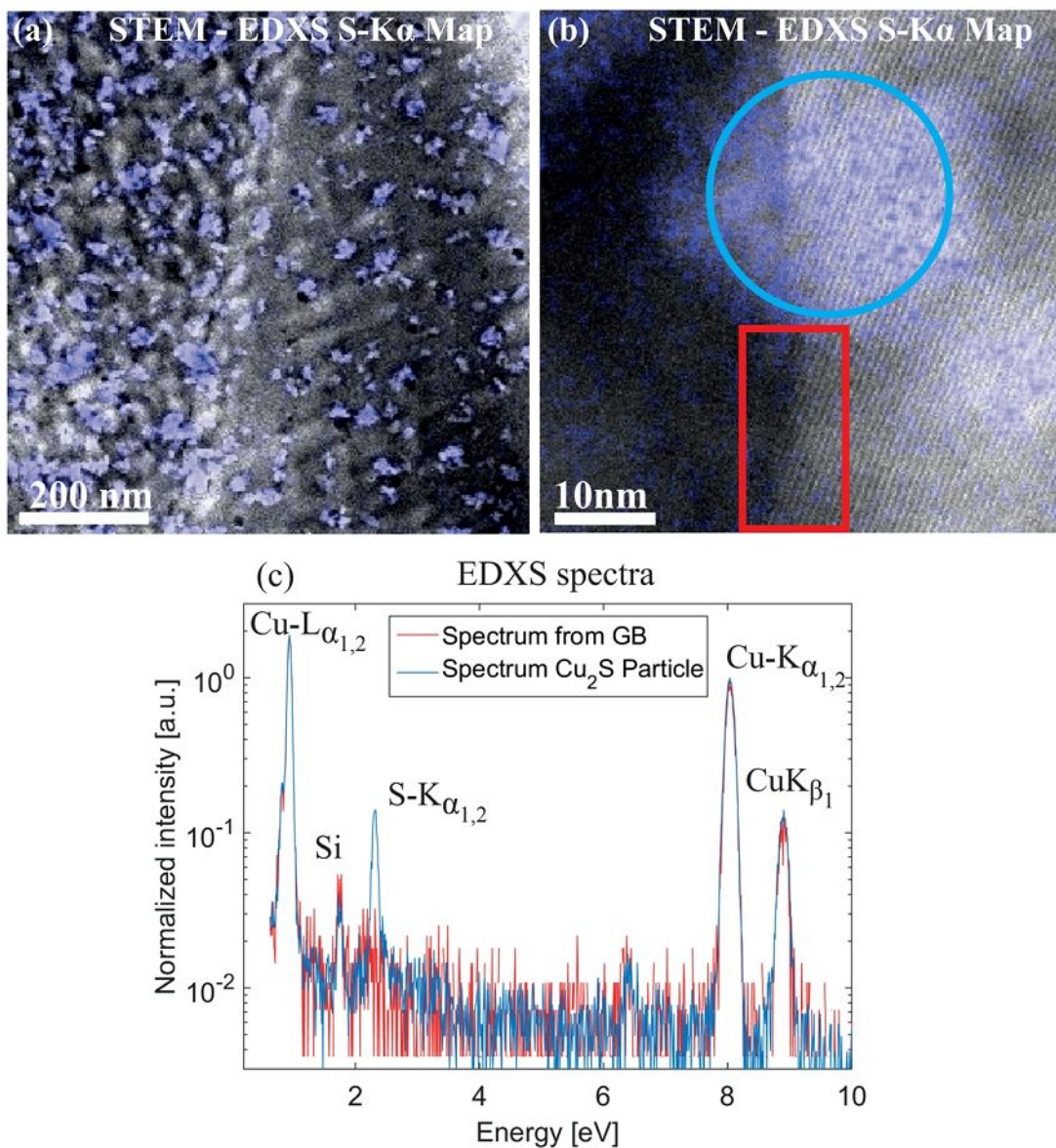

Fig. 8.8.: EDXS of the small Cu_2S particles: (a,b) STEM-EDXS maps with the $S - K_\alpha$ signal overlaid in blue with the HAADF images from fig. 8.4 (c) of S7920$_1$ and (c) accompanying spectrum of a small particle compared to the GB region indicated by the blue circle and red rectangle in (b).

STEM investigations of S7920$_2$, containing a large, lenticular precipitate located at a GB are presented in Fig. 8.9. The contrast difference between the Cu matrix and the sulfide stems from different milling rates in the FIB that translates into a thickness difference at the phase boundary (see Fig. 8.9 (a) and (b)), while the long stripes in Fig. 8.9 (b) come from curtaining during FIB milling. One phase boundary was investigated in different crystallographic orientations (as an example the matrix in [011] orientation is shown in Fig. 8.9 (c)), but no evidence for a special orientation relationship was found indicating an incoherent phase boundary. The crystal structure of the precipitate was explored using high resolution STEM imaging, shown in Fig. 8.9 (d) and (e), SAD and image simulation with JEMS [164]. The structure was determined as low chalcocite Cu_2S with monoclinic-prismatic structure mP144 P21/c and is predicted to be a stable compound at RT [135].
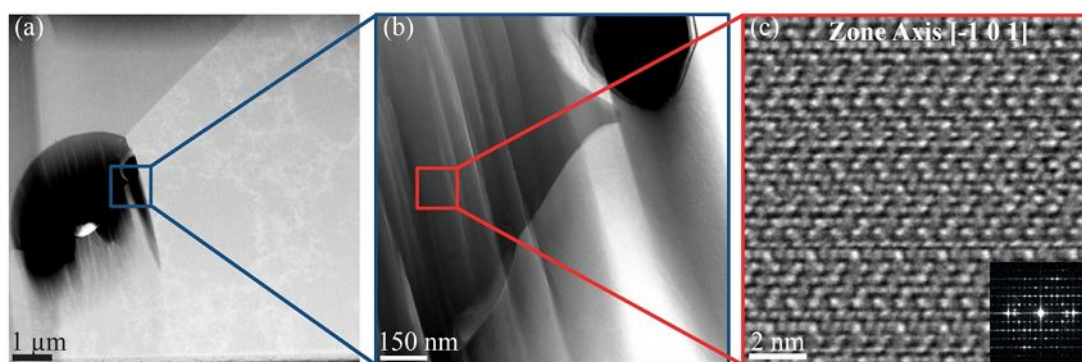

Fig. 8.9.: High resolution STEM investigation of the large Cu_2S particle: (a) HAADF-STEM image of a large, lenticular Cu_2S precipitate embedded at grain boundary. (b) and shows the phase boundary between the precipitate and the lower grain with the [110] direction parallel to the beam. (c) High-resolution STEM image of the precipitate imaged along [1$\bar{0}$1] and the corresponding FFT match the monoclinic crystal structure of low chalcocite Cu_2S.

A STEM-EDXS map of the phase boundary from Fig. 8.9 (b) is illustrated in Fig. 8.10 (a) and the corresponding spectrum in (b). The $S-K_\alpha$ peak appears in the precipitate and not in the matrix. Phosphorous (P), is only detectable in the Cu_2S particle and the broad peak at ~3 keV that may be related to silver. The iron and cobalt signal results from spurious X-rays from the interior of the microscope. The quantification with the standardless Cliff-Lorimer method [57] obtained a stoichiometry of 2.7 : 1 (Cu:S) and is, therefore, overestimated compared to Cu_2S. This discrepancy originates from copper redeposition while thinning the specimen with Ar+ ions and also from the

TEM grid, which was made out of copper.

The $S - L_{2,3}$ EEL spectra of the large Cu_2S particles are compared with the EEL spectra of the small precipitates from S7920$_1$ (see Fig. 8.11 (a) and (b)). The EEL spectrum was taken from a precipitate located close to the vacuum. The $S - L_{2,3}$ edge is well pronounced in both samples and shows a small shoulder at $165\,eV$ in a steep slope of the edge, followed by a plateau at $\sim$175 eV and a second shoulder at $\sim$182 eV. The similarities between both edges indicate a similar electronic structure and hence crystal structure between the large and small precipitates. The $S - L_{2,3}$ edge of the surrounding matrix region of the small particle (Fig. 8.11 (a)) is zero in the whole spectrum. This is different for the surrounding region of the large precipitate. The $S - L_{2,3}$ edge shows an increasing signal with a small slope well before $165\,eV$ energy loss. This signal arises from oscillations of the plasmon peak and the $Cu - M_1$ edge due to a thickness of $56\,nm$. This feature is absent in S7920$_1$ with a thickness of $22\,nm$. In reference measurements we found that these oscillations become significant at sample thicknesses of $> 30\,nm$.

The $Cu - L_{2,3}$ edges of the Cu matrix and the Cu_2S particle exhibit a different shape (Fig. 8.11). Inside the matrix, the signal shows no white lines due to the filled 3d band [165]. Instead, there are two small peaks visible, stemming from Van-Hove singularities in the density of states [107]. In addition, a chemical shift of $\sim$3 eV is revealed due to the change in Cu oxidation state.

The GB chemistry of sample S27 after annealing at $500°\,C$ for $4\,h$ shows no difference compared to the former results. WDXS reveals no enrichment at different GBs, and no precipitates were found in a large region surrounding the GB area (not shown here). We also performed 6 APT measurements at a random GB. TKD was used to confirm that all 6 APT specimens contained the GB, as detailed in Fig. 8.6. A representative APT reconstruction and the corresponding concentration profile of S and O across the GB are illustrated in Fig. 8.12. Once again here, no S enrichment at the GB is observed.
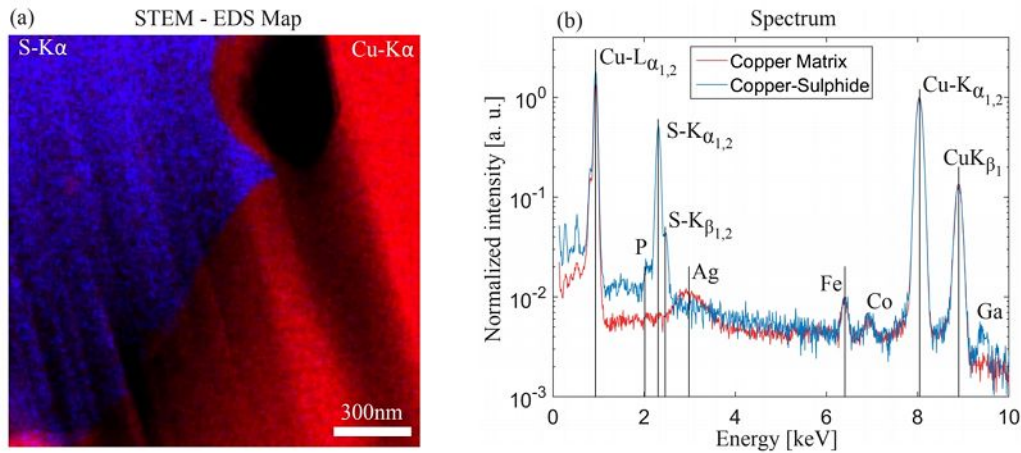
Fig. 8.10.: EDXS of the large Cu_2S particle: (a) The STEM-EDXS Map with $S - K_\alpha$ and $Cu - K_\alpha$ signal of the phase boundary from Fig. 8.8 (b) with corresponding spectrum of the matrix (red) and the precipitate (blue).

8.3. Discussion

Macroscopic investigations of the alloys revealed a grain size of several mm. In the alloy S7920, a dendritic structure was found with a large amount of Cu_2S precipitates surrounding mainly the GBs in the interdendritic regions. The in depth microstructural characterization of the initial alloys S14, S27 and S7920 shows no S enrichment at GBs within the detection limits of WDXS, STEM-EDXS, STEM-EELS and APT measurements. Annealing the alloy with 27 ppm S at $500°C$ for $4\,h$ did not reveal S enrichments at the GBs from APT and WDXS. Furthermore, no precipitates were found in the alloys S14 and S27 within the grains and close to GBs. In the alloy S7920 with 7920 ppm S, monoclinic Cu_2S precipitates were found mainly at the GBs but also within the grains with a size ranging from ~$5\,nm$ up to ~$10\mu m$.

The microstructural observations indicate that the S embrittlement of high-purity Cu is not related to S enrichments at GBs, but a possible cause is the formation of nanoscale, monoclinic Cu_2S precipitates. These brittle precipitates, considered as a GB irregularity, can favor void cavitation along sliding boundaries [166]. As discussed above, S diffusion in copper is anomalous. Moya et al. measured the S the diffusion coefficient in copper for temperatures between 550 and $1000°C$ to $D_{550°C} = 8 \cdot 10^{-12} \frac{cm^2}{s^{-1}}$ and $D_{1000°C} = 7.6 \cdot 10^{-8} \frac{cm^2}{s^{-1}}$ [133]. These values are up to two orders of magnitude higher compared to other elements (e.g. Co, Ni). The formation of Cu_2S is
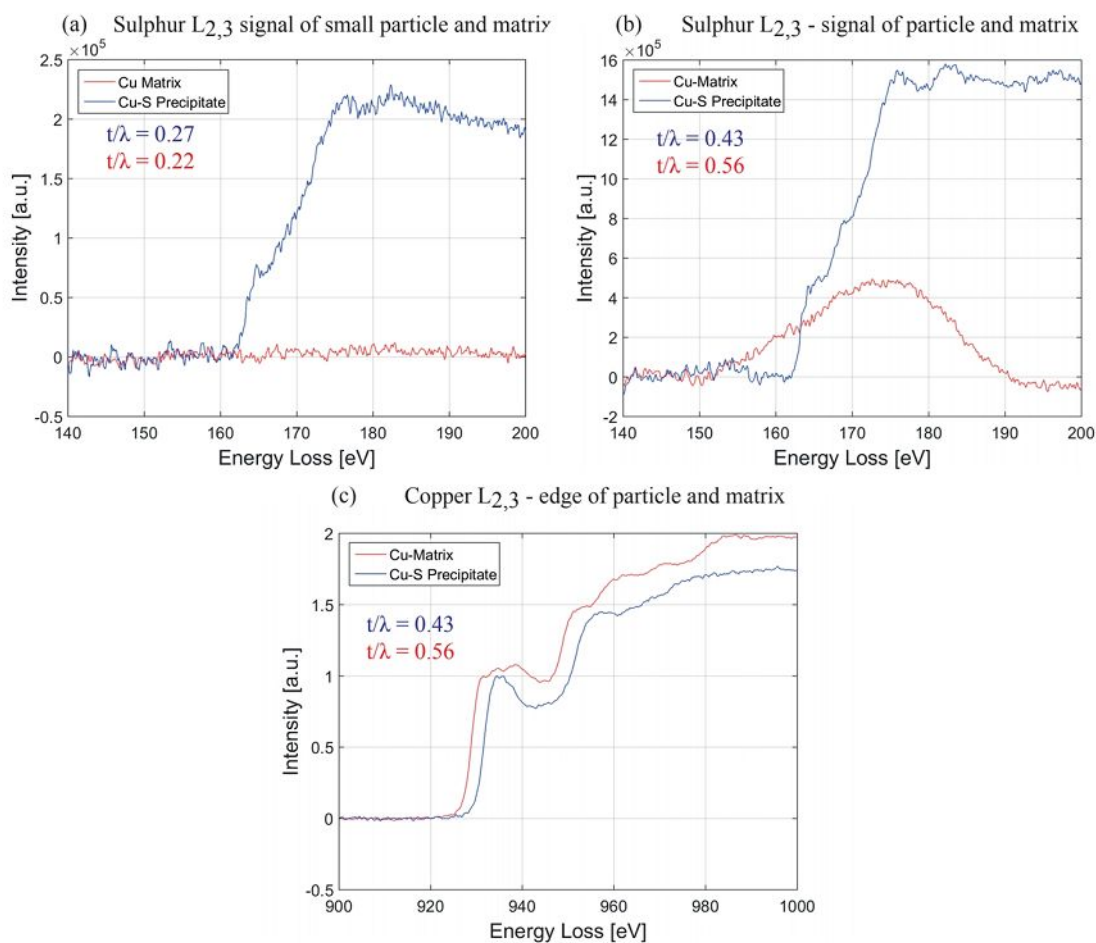
Fig. 8.11.: EELS of the Cu_2S precipitates and the Cu matrix: EEL spectra of the $S-L_{2,3}$ edge of the small (a) and large (b) precipitate and the EEL spectra of the adjacent Cu matrix. The t/λ value corresponds to the thickness of the measured region with λ being the inelastic mean free path in Cu. The blue curve represents the measurement of the particle and the red curve of the accompanying matrix close to the precipitate. Note that the broad peak measured in Cu (b) is not due to S (see text for details) (c) $Cu-L_{2,3}$ edge of the large precipitate and the Cu matrix. Note the chemical shift of ~3 eV and the differences in the near edge fine structure.

described to be very fast so that during slow solidification and cooling (indicated by the large grain size) S atoms diffuse to the GBs and form these sulfides.

In the following we discuss shortly the detection limits of the employed methods and the detection of S in this study. After that we will draw a connection of the microstructure to the mechanical properties of the Cu alloys.
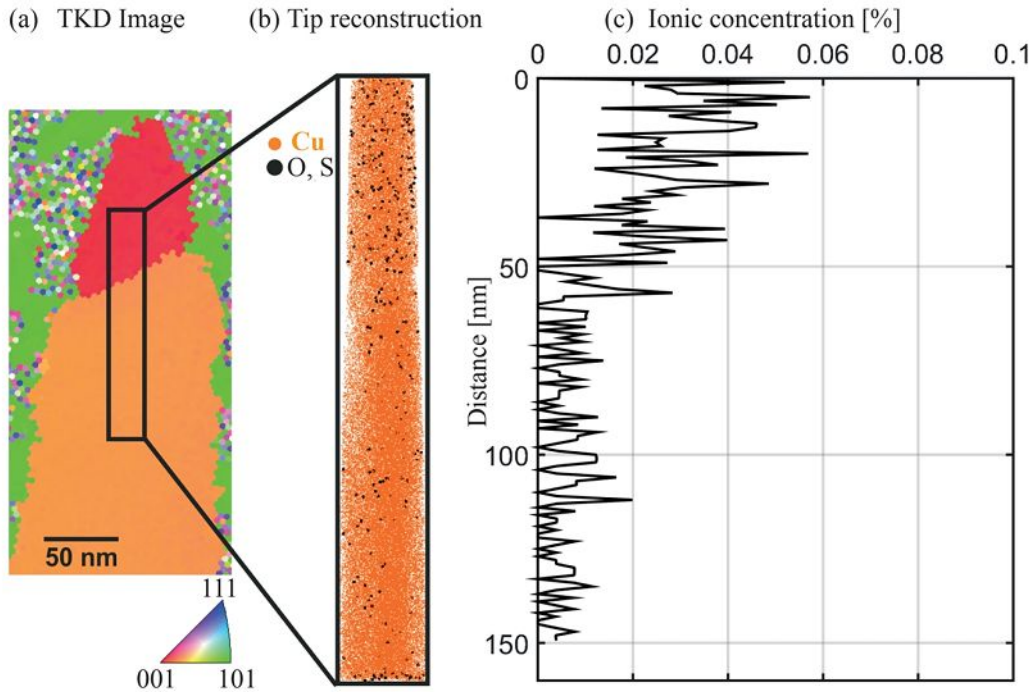
Fig. 8.12.: APT investigation of the annealed S27 alloy: (a) TKD map of an APT specimen, prepared from the GB of alloy S27 after annealing. (b) Corresponding APT reconstruction of the specimen, displaying the Cu as orange and the S^{+2} / O^{+} atoms as black dots. (c) Concentration profile of S^{+2} / O^{+} along the APT specimen (Note that both elements overlap strongly in APT mass spectra).

8.3.1. Detection Limits

The compositional resolution of the employed techniques plays an important role since we are dealing with very low impurity concentrations in S14 and S27, with 14 and 27 at. ppm respectively. In ref. [67] the analytical sensitivity of an uncorrected STEM was determined to ~0.12 wt. % in a Cu-Mn alloy. This study [67] also mentioned that the limit can be increased by a factor of ~3 by using an aberration-corrected microscope. Furthermore, M. Watanabe and D.B. Williams reported on the detection of single atoms in the analysis volume of thin specimen with EDXS [167]. This becomes possible with the use of corrected electron optics, equipped with a field emission gun and the highest possible X-ray collection efficiency. They also show that the specimen thickness plays an important role. They measured single Mn atoms in a $10\,nm$ thick $Cu-0.1\%\,Mn$ foil, whereas a thickness of $30\,nm$ leads to a detection of only 10 Mn atoms. Taking this into account, we can assume that our detection limit of S in a Cu

matrix should be well below 300 ppm and even better in very thin samples. A further description for the detection limit in EDXS can be found in [57].

In EELS, the minimum detectable concentration is in general lower than for EDXS. It is reported that down to 10 ppm for transition metals and down to 20 ppm for Ca in organic specimen are measurable [59]. Therefore, we conclude that the detectable limit for S in Cu is in a similar range depending on the sample thickness and quality. The EELS measurements of S, in our study with specimen thicknesses of $> 30\,nm$ are mainly limited by oscillations from the plasmon peak and also the $Cu - M_1$ edge that obstruct a weak S signal.

8.3.2. Sulfur detection in our study

Assuming a homogenous distribution of S within the samples, the S concentration ranges in S14 and S27 lie below / close to the detection limit of EELS. However, the local S concentration in nanoscale Cu-sulfides or at decorated GBs is expected to be higher than the chemical sensitivity of EELS in the electron microscope. Henderson and Sandstroem reported on the S-induced embrittlement of oxygen-free high conductive copper with a S impurity concentration of ~$6 - 10$ wt. ppm (similar to the alloys S14 (7 ppm) and S27 (14 ppm) here) [130]. They calculated that, in a case where the entire S excess impurities (considering the solubility of S of 5 ppm at $600°\,C$) was to segregate to GBs, an average coverage of $0.36 - 2.2$ monoatomic layers for a grain size between $60\mu\,m$ and $370\mu\,m$ is obtained. Using AES, they found a S concentration of ~2 to 8 at. % at fractured GBs. In order to quantify the S segregation in their case we make use of the GB enrichment factor from the segregation model by McLean, which is defined as the ratio between the S concentration at the GB and the S bulk concentration: $\beta = \frac{X_S^{GB}}{X_S}$ [15, 50, 168]. Applying this model to the numbers from Henderson and Sandstroem [130] translates to a GB enrichment factor of ~$1600 - 4000$ for S in Cu for their alloys. A slightly higher value is reported in literature by Pineau et al., where they found a GB enrichment factor of S in Cu of ~11500 [169]. Furthermore, GB enrichment factors for S in Ni and Fe are reported to be even higher than for Cu of ~20.000 [15]. Assuming GB enrichment factors between 1600 and 11500 with

a minimum bulk S concentration of 5 ppm translates to an average S concentration at the GBs of ~1 to 6 at. % for the alloys S14 and S27. These concentration levels are detectable with all employed microscopic techniques. However, GB segregation can be strongly anisotropic depending on the GB character and chemistry [170–172]. This can also explain the large scatter in GB enrichment factors found in literature. Therefore, we investigated different random high and low angle GBs with different misorientations and GB plane inclinations. Since we never observed any S enriched GBs we conclude that S is trapped in nanoscale Cu_2S precipitates.

According to the equilibrium phase diagram [135], there is the possibility that Cu-S precipitates form even in the samples with low S concentrations, which we were not able to detect in our study. The limitations in measuring trace impurities or extremely small particle densities arises from the detection limits and sampled specimen volume of the employed technique. Assuming that all S atoms contribute to the formation of nanometer sized Cu_2S precipitates (e.g. a few nm to ~$10\,nm$), as described in the introduction, this would translate into a particle density of up to ~20000 particles per mm^3 (or 0.00002 particles per μm^3). With EPMA, an elemental resolution down to a few tens of ppm is accessible while the lateral resolution is ~$1\mu m$, which corresponds to a sampled volume of ~$10^3 \mu m^3$. However, the lateral resolution of EPMA is too low for detecting confined S-rich regions at GBs or small precipitate sizes and densities. TEM and APT have much higher lateral resolution, in the sub-nanometer range, and the detection limit for light elements is ~100 ppm for TEM and a few tens of ppm for APT. However, considering the small specimen volumes of TEM and APT with typically less than ~$1\mu m^3$ and $0.002\mu m^3$, respectively, the probability to observe one particle is extremely low and would require the measurement of thousands of samples to maybe detect only one single particle.

8.3.3. Connection to the mechanical data

Nevertheless, a likely scenario is that S forms small Cu_2S precipitates, with a higher probability at GBs, as described in [132] that are then contributing to the embrittlement of Cu. In the tensile test of Fig. 8.1, we also observe a hardening effect with

increasing S concentration even between S14 and S27. This could be interpreted as precipitation hardening and therefore supports our hypotheses. In S7920, we found precipitates ranging from several nm to several μm in size. They were mainly located in the interdendritic regions at GBs and within the grains. Large precipitates showed a lenticular shape at GBs and a round shape in the grains. The EELS measurements of the small and large precipitates show no difference in the $S - L_{2,3}$ edge indicating that the precipitates have a similar crystal structure. At the same time, we never observed any enrichment of S at GBs with EDXS, EELS and APT, even in the sample with the highest S concentration. These findings are in agreement with the mechanical data, since not only an embrittlement, but also the hardening effect is observed during loading as mentioned before. Furthermore, it also strengthens our hypothesis that there is no pronounced solute segregation in S14 and S27, but most likely precipitation.

The Cu_2S phase itself exhibits a strongly brittle behavior [173] and such precipitates at GBs are a place for crack initiation, because Cu_2S acts as a nucleation site for cavities, as reported by Henderson et al. [130]. The large precipitates in S7920 at the GBs possess incoherent interfaces with Cu. The precipitates at the GB are allotriomorph by showing two symmetrical spheres separated by the GB which translates into a lenticular shape [17]. We assume that these precipitates are responsible for the failure of alloy S7920. In S14 and S27, we assume that small incoherent precipitates ~5 nm (as seen in $S7920_1$) lead to a strengthening during loading, as can be seen in the tensile test in Fig. 8.1, and incoherent precipitates with sizes of $\geq 100\,nm$ serve as crack initiation sites.

The tensile tests also show that with increasing temperature the embrittlement becomes more pronounced (Fig. 8.1). One possible explanation for this behavior is that Cu_2S undergoes a polymorphic transformation by increasing temperature or its stoichiometric varieties (Cu_xS) that then affect the crack initiation [174].

It has to be mentioned that hardening and strain to failure can also be slightly affected by our tensile tests. The grain size, their distribution and orientation to the loading axis also affects our mechanical experiments, since it is in a comparable size range as the test specimen itself (several mm grain sizes compared to 10 mm sample size).

Thus, the arrangement of GBs within the gauge length of the tensile sample can lead to fluctuations in the measured fracture elongation and with this misinterpretation of the mechanical behavior. This may be the case for the $400°C$ measurement in S27 of Fig. 8.1 (b), which seems as brittle as sample C at $400°C$ but with a much lower S content.

8.4. Conclusion

The effect of different levels of S in Cu on the mechanical properties, microstructure and chemistry was investigated. High-resolution STEM and the analytical methods EDXS and EELS and APT are employed in order to explain the reduction in ductility of Cu induced by a variation in S content. Three samples with different S concentrations (14 ppm, 27 ppm and 7920 ppm) consist of a polycrystalline grain structure with an average grain size of $\sim 2-4\,mm$ and mostly random high and low angle GBs. With STEM imaging, STEM-EDXS and EELS no clear evidence for S enrichments at GBs was detected in all three alloys considering the detection limit of the latter methods. These observations are supported by APT studies in the alloy with a S content of 27 at. ppm. In the alloy with 7920 at. ppm S nano- and microsized Cu_2S precipitates, known as low chalcocite, were identified by STEM at GBs as well as within the grains. It is speculated that the incoherent interfaces of the precipitates at the GBs lead to crack initiation under load and are therefore responsible for the embrittling effect in the alloy with 7920 ppm S. The alloys containing 14 and 27 at. ppm show also a loss in ductility at elevated temperatures. While the mechanism was not resolved, we propose that nanometer sized Cu_2S precipitates have formed along the GBs serving as crack initiation sites and thus promote early failure.

9. Summary and final conclusion

In the present thesis, high resolution (S)TEM and its analytical techniques EELS and EDXS, APT and atomistic simulations were used to study the detailed atomic structure and local chemistry of random and special GBs in different Cu alloys.

Cu thin films have been grown on (0001) oriented Sapphire, which results in a polycrystalline, [111] textured thin film, containing mostly perfect tilt GB. The grain size is bimodal and in the range of $\sim 100\,\mu m$ and the grains adopt a cylindrical shape. In this thesis detailed investigation on two different symmetric GBs have been performed, the $\Sigma 19b\,(2\bar{5}3)$ and $\Sigma 19b\,(1\bar{8}7)$ GBs. Due to the cylindrical shape of the grains, asymmetric variations of the GBs are frequently observed. The atomic structure, observed by high resolution STEM, was found to be very complex, with long period structural units. The structures cannot be described by the conventional structural unit model, since too many structural sub-units are needed to form the two boundaries, which cannot be described by two delimiting GBs. Even though the $\Sigma 19b\,(2\bar{5}3)$ and $\Sigma 19b\,(1\bar{8}7)$ differ only in its GB plane inclination by $30°$, the structure changes significantly from the zipper to the pearl structure. Molecular static simulations at $0\,K$ produce the exact same GB structures. In asymmetric geometries, the zipper structure was found to introduce steps in the GB separated by symmetric $(2\bar{5}3)$ facets. The amount of steps seems to scale with the degree of asymmetry. In case of the pearl structure, no facets and steps are formed, but additional structural sub-units are introduced. The higher the asymmetry, the more sub-units are added.

In GBs adopting the pearl structure, congruent GB phase transitions are observed in symmetric and asymmetric cases, where the pearl structure transforms into the domino structure. The experimental observations are complemented by evolution-

ary search and atomistic simulations, which is a powerful combination to unravel the thermodynamic nature of phase transitions of clean GBs and can greatly expand the current knowledge of GB phase transitions. It is found that, due to the line defect separating the two GB phases, both phases can coexist over a wide range of temperatures down to room temperature, even though the domino structure is metastable. A congruent phase transition at an asymmetric, clean GB indicates that these interfacial transitions can also occur at more general GBs, which was not considered up to date.

In addition, the effect of impurity atoms on the atomic structure of the $\Sigma 19b(2\bar{5}3)$ and $\Sigma 19b(1\bar{8}7)$ GBs is investigated. As impurity elements Ta and Zr have been chosen, since these are frequently used in nanocrystalline materials to stabilize the nc grain structure. Ta and Zr thin films ($50 - 100\,nm$ thick) were deposited via sputtering onto the Cu and were annealed in order to activate GB diffusion. With STEM and APT, the atomic structure, structural transition and the chemistry were investigated.

Even though the diffusion of Ta in copper is negligible below $1000°\,C$, diffusion along the GB was activated. Nanometer sized Ta particle were found along the GBs. A special particle was observed, which locally bent the GB plane due to the surface tension between particle surface and the GB plane. This is described by the Zener effect and leads to a pinning of the GB.

Adding Zr to the GBs leads to different results depending on the atomic structure, i.e. for the zipper and the pearl structure respectively. In the pearl structure, the Zr segregates homogeneously along the GB and induces a higher disorder. The GB appears black under HAADF conditions. However, the original structure still can be seen, which shows distortions and missing atomic columns in the sub-units. With APT a Zr concentration of about $\sim 1.6\,at.\%$ was measured at a random tilt GB in absence of oxygen. I.e. pure Zr is segregated at the GBs. At asymmetric GBs with steps and symmetric zipper facets, Zr segregates only to the steps and induces a higher disorder. The symmetric facets seem to be Zr free. However, structural transition are observed from the trapezoidal to the rectangular sub-unit. This indicates that Zr is present, which is just below the detection limit of EDS and EELS. It is assumed that due to Zr segregation the local chemical potential changes and favors structural transitions and lowers in this way the overall GB free energy.

Both, Ta and Zr are promising candidates to stabilize the microstructure of nanocrystalline Cu. Ta pins the GBs with second phase particles and stops GB migration. Zr causes GB disordering, which affects the mechanical behavior and most likely reduces the GB free energy and by this the driving force for GB migration.

The atomic structure of random GBs is hardly accessible by high resolution TEM due to the random orientation of both grains. Nevertheless, it is important to pay also attention to them and investigate their nature deeply. The random GBs were taken from recycled Cu from the company Brixlegg with different S concentrations. The effect of different S concentrations on the mechanical performance, the microstructure and chemistry was investigated. Macro-sized tensile tests showed a reduction in ductility accompanied with a strengthening for increasing S contents. Even though literature predicts solute segregation of S to the GBs, it was never detected by high resolution (S)TEM techniques nor with APT in all three alloys. In the alloys containing most S, however, the formation of nano- and micron- sized Cu_2S precipitates within the grains and at GBs was observed. The structure of these precipitates is known as low chalcocite. Since no other S enrichment could be detected it is assumed that the particles, which have a brittle nature itself, may be responsible for the reduction in ductility and the increase in ultimate tensile strength. Under loading conditions, the incoherent interface at the GBs between the particle and the matrix can lead to crack initiation and can promote early failure.

In summary, this thesis investigates in detail the atomistic origins of GB phenomena in pure Cu as well as alloyed Cu GBs. It becomes clear that GBs are very complex defects which can exist in a large amount of different geometrical and chemical states. Therefore, a lot of effort has to be made to get a generalized picture and understand the atomistic mechanism at all kinds of GBs, since already small structural or chemical transitions can have a large impact on the GB properties and therefore on the macroscopic performance of the material. This thesis shows a ways how this can be studied in detailed and be connected to the properties. It extends greatly the general knowledge of GB segregation and phase transitions and can be effectively used to make progress towards defined GB engineering. Summarizing, the following main point have been achieved in this thesis and go beyond state of the art:

1. This thesis presents the first experimental, atomic structures of symmetric $\Sigma 19b$ GBs and asymmetric near $\Sigma 19b$ GBs (chapter 6 and 7). Furthermore, the first direct experimental proof of congruent GB phase transitions is presented, by using a combination of high resolution imaging and computer simulations.

2. The effect of Ta and Zr on the atomic structure of a well defined GB is investigated in detail and directly connected to the mechanical stabilization mechanism in nc Cu. This work shows that Ta forms nano sized precipitates and pins the GB via the Zener effect. Thus it stabilizes nc Cu via the kinetic approach. Zr induces disorder and structural transitions and depends strongly on the type and atomic structure of the GBs. This lowers the GB free energy and with that the driving force for GB migration and belongs to the thermodynamic approach.

3. The investigation of ultra pure Cu and Cu-S alloys revealed that the embrittlement mechanism cannot be related to homogenous solute segregation of S to the GBs. It is more the formation of nano meter sized Cu_2S, which favor crack nucleation and, thus, embrittlement. The detailed and scale bridging microstructural investigations (from mm to atomic distances) greatly extend the current knowledge of this longstanding and still not understood phenomena.

List of Figures

List of Tables

References

1. Dillon, S. J. *et al.* Complexion: A new concept for kinetic engineering in materials science. *Acta Materialia* **55,** 6208–6218 (Oct. 2007) (cit. on p. 1).

2. Harmer, M. P. The Phase Behavior of Interfaces. en. *Science* **332,** 182–183 (Apr. 2011) (cit. on p. 1).

3. Forsyth, P. J. E. *et al.* Grain Boundaries in Metals. en. *Nature* **158,** 875–876 (Dec. 1946) (cit. on p. 1).

4. Hoagland, R. G. & Kurtz, R. J. The relation between grain-boundary structure and sliding resistance. en. *Philosophical Magazine A* **82,** 1073–1092 (Apr. 2002) (cit. on p. 1).

5. Luo, J. *et al.* The Role of a Bilayer Interfacial Phase on Liquid Metal Embrittlement. en. *Science* **333,** 1730–1733 (Sept. 2011) (cit. on pp. 1, 51, 52).

6. Cantwell, P. R. *et al.* Grain boundary complexions. *Acta Materialia* **62,** 1–48 (Jan. 2014) (cit. on pp. 1, 12, 51, 53, 54, 64).

7. Hu, T. *et al.* Role of disordered bipolar complexions on the sulfur embrittlement of nickel general grain boundaries. en. *Nature Communications* **9,** 2764 (Dec. 2018) (cit. on p. 1).

8. Raabe, D. *et al.* Grain boundary segregation engineering in metallic alloys: A pathway to the design of interfaces. en. *Current Opinion in Solid State and Materials Science* **18,** 253–261 (Aug. 2014) (cit. on pp. 1, 15).

9. Ainslie, N. *et al.* Sulfur segregation at \alpha-iron grain boundaries—II. en. *Acta Metallurgica* **8,** 528–538 (Aug. 1960) (cit. on pp. 1, 59, 105).

10. Hart, E. W. Two-dimensional phase transformation in grain boundaries. *Scripta Metallurgica* **2,** 179–182 (Mar. 1968) (cit. on pp. 1, 11, 12).

11. Hart, E. W. in *The Nature and Behavior of Grain Boundaries* 155–170 (Springer, Boston, MA, 1972) (cit. on pp. 1, 11, 12).

12. Cahn, J. W. TRANSITIONS AND PHASE EQUILIBRIA AMONG GRAIN BOUND-ARY STRUCTURES. *Le Journal de Physique Colloques* **43,** C6–199–C6–213 (Dec. 1982) (cit. on pp. 1, 11, 13, 64, 74).

13. Rottman, C. Theory of phase transitions at internal interfaces. *Le Journal de Physique Colloques* **49,** C5–313 (1988) (cit. on pp. 1, 11, 64).

14. Tang, M. *et al.* Diffuse interface model for structural transitions of grain boundaries. en. *Physical Review B* **73** (Jan. 2006) (cit. on pp. 1, 11).

15. Lejcek, P. *Grain Boundary Segregation in Metals* (Springer Berlin Heidelberg, Berlin, Heidelberg, 2010) (cit. on pp. 1, 2, 7–9, 11, 14, 15, 59, 61, 97, 105, 117).

16. Sutton, A. P. & Vitek, V. On the structure of tilt grain boundaries in cubic metals I. Symmetrical tilt boundaries. *Philosophical Transactions of the Royal Society of London A: Mathematical, Physical and Engineering Sciences* **309,** 1–36 (1983) (cit. on pp. 2, 7, 43).

17. Priester, L. *Grain Boundaries* (Springer Netherlands, Dordrecht, 2013) (cit. on pp. 2, 5–7, 14–16, 97, 119).

18. Meiners, T. *et al.* Sulfur – induced embrittlement in high-purity, polycrystalline copper. *Acta Materialia* **156,** 64–75 (Sept. 2018) (cit. on pp. 2, 45, 51, 101).

19. Wimmer, A. *et al.* Temperature dependent transition of intragranular plastic to intergranular brittle failure in electrodeposited Cu micro-tensile samples. en. *Materials Science and Engineering: A* **618,** 398–405 (Nov. 2014) (cit. on pp. 2, 54, 59, 61).

20. Frost, H. J. *et al.* A catalogue of [100],[110], and [111] symmetric tilt boundaries in face-centered cubic hard sphere crystals. (1982) (cit. on pp. 2, 7, 91, 93).

21. Gui Jin Wang *et al.* A computer simulation study of [001] and [111] tilt boundaries: the multiplicity of structures. *Acta Metallurgica* **32,** 1093–1104 (July 1984) (cit. on pp. 2, 7, 91, 93).

22. Shvindlerman, L. S. *et al.* Grain boundary excess free volume—direct thermo-dynamic measurement. en. *Journal of Materials Science* **41,** 7725–7729 (Dec. 2006) (cit. on p. 2).

23. Duscher, G. *et al.* Bismuth-induced embrittlement of copper grain boundaries. *Nature Materials* **3,** 621–626 (Sept. 2004) (cit. on pp. 2, 51).

24. Frolov, T. *et al.* Effect of Interface Phase Transformations on Diffusion and Segregation in High-Angle Grain Boundaries. en. *Physical Review Letters* **110** (June 2013) (cit. on pp. 2, 13, 52–54, 64, 74).

25. Zhu, Q. *et al.* Predicting phase behavior of grain boundaries with evolutionary search and machine learning. en. *Nature Communications* **9** (Dec. 2018) (cit. on pp. 2, 12, 13, 43, 44, 52, 63, 64, 67, 68, 74, 75).

26. Ikuhara, Y. Grain Boundary and Interface Structures in Ceramics. en. *Journal of the Ceramic Society of Japan* **109,** S110–S120 (July 2001) (cit. on p. 2).

27. Kurishita, H. *et al.* en. in *Silicon Carbide Ceramics—1: Fundamental and Solid Reaction* (eds Sōmiya, S. & Inomata, Y.) 185–211 (Springer Netherlands, Dordrecht, 1991) (cit. on p. 2).

28. Stoffers, A. *et al.* Correlating Atom Probe Tomography with Atomic-Resolved Scanning Transmission Electron Microscopy: Example of Segregation at Silicon Grain Boundaries. en. *Microscopy and Microanalysis* **23,** 291–299 (Apr. 2017) (cit. on p. 2).

29. Medlin, D. *et al.* Defect character at grain boundary facet junctions: Analysis of an asymmetric Sigma 5 grain boundary in Fe. en. *Acta Materialia* **124,** 383–396 (Feb. 2017) (cit. on p. 2).

30. Peter, N. J. *et al.* Segregation-Induced Nanofaceting Transition at an Asymmetric Tilt Grain Boundary in Copper. en. *Physical Review Letters* **121** (Dec. 2018) (cit. on pp. 2, 51, 52, 64, 71).

31. Yu, Z. *et al.* Segregation-induced ordered superstructures at general grain boundaries in a nickel-bismuth alloy. en. *Science* **358,** 97–101 (Oct. 2017) (cit. on pp. 2, 51, 76).

32. Meiners, T. *et al.* Observations of grain-boundary phase transformations in an elemental metal. en. *Nature* **579,** 375–378 (Mar. 2020) (cit. on pp. 2, 45, 51, 63).

33. Read, W. T. & Shockley, W. Dislocation Models of Crystal Grain Boundaries. *Physical Review* **78,** 275–289 (May 1950) (cit. on p. 5).

34. Han, J. *et al.* The grain-boundary structural unit model redux. *Acta Materialia* **133,** 186–199 (July 2017) (cit. on pp. 6, 7, 52, 80, 92, 93).

35. Hornstra, J. Models of grain boundaries in the diamond lattice I. Tilt about I 10. *Physica* **25,** 409–422 (Jan. 1959) (cit. on p. 7).

36. Frost, H. & Spaepen, F. HARD SPHERE MODELS FOR THE STRUCTURE OF GRAIN BOUNDARIES. *Journal de Physique Colloques* **43,** C6–73–C6–82 (1982) (cit. on pp. 7, 93).

37. Sutton Adrian Peter *et al.* On the structure of tilt grain boundaries in cubic metals II. Asymmetrical tilt boundaries. *Philosophical Transactions of the Royal Society of London. Series A, Mathematical and Physical Sciences* **309,** 37–54 (Mar. 1983) (cit. on p. 7).

38. Bishop, G. H. & Chalmers, B. A coincidence Edge Dislocation description of grain boundaries. *Scripta Metallurgica* **2,** 133–139 (Feb. 1968) (cit. on pp. 7, 80, 92).

39. Pawaskar, D. N. *et al.* Structure and energetics of long-period tilt grain boundaries using an effective Hamiltonian. *Physical Review B* **63,** 214105 (May 2001) (cit. on pp. 7, 93).

40. Rittner, J. D. & Seidman, D. N. [110] symmetric tilt grain-boundary structures in fcc metals with low stacking-fault energies. *Physical Review B* **54,** 6999–7015 (Sept. 1996) (cit. on pp. 7, 93).

41. Sutton, A. P. & Balluffi, R. W. *Interfaces in crystalline materials* English. OCLC: 31166519 (Clarendon Press ; Oxford University Press, Oxford; New York, 1995) (cit. on pp. 8, 10, 13, 43).

42. Pond, R. C. & Vitek, V. Periodic Grain Boundary Structures in Aluminium. I. A Combined Experimental and Theoretical Investigation of Coincidence Grain Boundary Structure in Aluminium. en. *Proceedings of the Royal Society A: Mathematical, Physical and Engineering Sciences* **357,** 453–470 (Nov. 1977) (cit. on p. 8).

134

43. Kronberg, M. L. & Wilson, u. F. Secondary recrystallization in copper. *JOM* **1,** 501–514 (1949) (cit. on p. 9).

44. Tschopp, M. A. *et al.* Symmetric and asymmetric tilt grain boundary structure and energy in Cu and Al (and transferability to other fcc metals). en. *Integrating Materials and Manufacturing Innovation* **4,** 11 (Dec. 2015) (cit. on p. 9).

45. Gottstein, G. & Shvindlerman, L. S. *Grain boundary migration in metals: thermodynamics, kinetics, applications* 2nd ed. OCLC: ocn166358378 (Taylor & Francis, Boca Raton, 2010) (cit. on p. 10).

46. Gibbs, J. W. *The scientific papers. Vol. 1, Vol. 1,* English. OCLC: 860879228 (Dover Publications, New York, 1961) (cit. on pp. 10, 14).

47. Cahn, J. W. Adapting thermodynamics for materials science problems. *Journal of phase equilibria* **15,** 373–379 (1994) (cit. on pp. 10, 11).

48. Frolov, T. *et al.* Structural phase transformations in metallic grain boundaries. en. *Nature Communications* **4,** ncomms2919 (May 2013) (cit. on pp. 13, 52, 63, 64, 72, 74, 75).

49. Frolov, T. *et al.* Grain boundary phases in bcc metals. en. *Nanoscale* **10,** 8253–8268 (May 2018) (cit. on pp. 13, 52, 63, 64, 75).

50. Seah, M. P. & Hondros, E. D. Grain boundary segregation. *Proc. R. Soc. Lond. A* **335,** 191–212 (1973) (cit. on pp. 13, 14, 117).

51. Chang, L. *et al.* Grain Boundary Segregation in the Cu-Bi System. *Defect and Diffusion Forum* **156,** 135–146 (Feb. 1998) (cit. on p. 13).

52. Hume-Rothery, W. *et al. The structure of metals and alloys [by] William Hume-Rothery, R.E. Smallman and C W. Haworth.* English. OCLC: 639778957 (Institute of Metals and the Institution of Metallurgists, London, 1969) (cit. on p. 14).

53. McLean, D. *Grain boundaries in metals.* English. OCLC: 565077791 (Clarendon Press, Oxford, 1957) (cit. on pp. 14, 15).

54. Nes, E. *et al.* On the Zener drag. *Acta Metallurgica* **33,** 11–22 (Jan. 1985) (cit. on pp. 16, 54, 94, 95).

55. Koju, R. K. *et al.* Zener Pinning of Grain Boundaries and Structural Stability of Immiscible Alloys. en. *JOM* **68,** 1596–1604 (June 2016) (cit. on pp. 16, 94, 95).

56. Williams, D. B. & Carter, C. B. *Transmission electron microscopy: a textbook for materials science* 2nd ed (Springer, New York, 2008) (cit. on pp. 19, 24).

57. *Transmission Electron Microscopy* en (eds Carter, C. B. & Williams, D. B.) (Springer International Publishing, Cham, 2016) (cit. on pp. 19, 26, 112, 117).

58. Egerton, R. F. *Physical principles of electron microscopy: an introduction to TEM, SEM, and AEM* OCLC: ocm61714990 (Springer, New York, NY, 2005) (cit. on pp. 19, 24, 36).

59. Egerton, R. *Electron Energy-Loss Spectroscopy in the Electron Microscope* en (Springer US, Boston, MA, 2011) (cit. on pp. 19, 24, 48, 117).

60. Goldstein, J. I. *et al. Scanning Electron Microscopy and Xray Microanalysis* en (Springer US, Boston, MA, 2003) (cit. on pp. 20–22, 34).

61. *Handbook of microscopy for nanotechnology* (eds Yao, N. & Wang, Z. L.) (Kluwer Academic Publishers, Boston, 2005) (cit. on p. 22).

62. *Introduction to focused ion beams: instrumentation, theory, techniques, and practice* (eds Giannuzzi, L. A. & Stevie, F. A.) (Springer, New York, 2005) (cit. on p. 23).

63. Born, M. & Wolf, E. *Principles of optics: electromagnetic theory of propagation, interference and diffraction of light* 6th (corr.) ed (Cambridge University Press, Cambridge, UK ; New York, 1997) (cit. on p. 24).

64. Lichte, H. *et al.* Aberration Correction and Electron Holography. en. *Microscopy and Microanalysis* **16,** 434–440 (Aug. 2010) (cit. on p. 24).

65. Watanabe, M. *et al.* Improvements in the X-Ray Analytical Capabilities of a Scanning Transmission Electron Microscope by Spherical-Aberration Correction. en. *Microscopy and Microanalysis* **12,** 515–526 (Dec. 2006) (cit. on pp. 24, 32, 38, 39).

66. *Transmission Electron Microscopy* en (eds Carter, C. B. & Williams, D. B.) (Springer International Publishing, Cham, 2016) (cit. on p. 24).

67. *Scanning transmission electron microscopy: imaging and analysis* (eds Pennycook, S. J. & Nellist, P. D.) (Springer, New York, NY, 2011) (cit. on pp. 24, 64, 116).

68. Kirkland, E. J. *Advanced computing in electron microscopy* Second edition (Springer, New York, 2010) (cit. on pp. 24, 32, 33, 44).

69. Egerton, R. *et al.* Radiation damage in the TEM and SEM. en. *Micron* **35,** 399–409 (Aug. 2004) (cit. on p. 35).

70. Cliff, G. & Lorimer, G. W. The quantitative analysis of thin specimens. en. *Journal of Microscopy* **103,** 203–207 (Mar. 1975) (cit. on p. 38).

71. Krivanek, O. L. *et al.* Progress in ultrahigh energy resolution EELS. *Ultramicroscopy. 75th Birthday of Christian Colliex, 85th Birthday of Archie Howie, and 75th Birthday of Hannes Lichte / PICO 2019 - Fifth Conference on Frontiers of Aberration Corrected Electron Microscopy* **203,** 60–67 (Aug. 2019) (cit. on p. 40).

72. Gault, B. *et al. Atom Probe Microscopy* (Springer New York, New York, NY, 2012) (cit. on pp. 42, 106).

73. Alder, B. J. & Wainwright, T. E. Studies in Molecular Dynamics. I. General Method. *The Journal of Chemical Physics* **31,** 459–466 (Aug. 1959) (cit. on p. 42).

74. Humphrey, W. *et al.* VMD: visual molecular dynamics. *Journal of molecular graphics* **14,** 33–38 (1996) (cit. on p. 43).

75. Plimpton, S. Fast Parallel Algorithms for Short-Range Molecular Dynamics. *Journal of Computational Physics* **117,** 1–19 (Mar. 1995) (cit. on pp. 43, 49).

76. Stukowski, A. Visualization and analysis of atomistic simulation data with OVITO–the Open Visualization Tool. en. *Modelling and Simulation in Materials Science and Engineering* **18,** 015012 (Dec. 2009) (cit. on pp. 43, 49).

77. Ophus, C. A fast image simulation algorithm for scanning transmission electron microscopy. en. *Advanced Structural and Chemical Imaging* **3,** 13 (May 2017) (cit. on pp. 44, 48, 71).

78. Mayer, J. *et al.* TEM sample preparation and FIB-induced damage. *MRS bulletin* **32,** 400–407 (2007) (cit. on p. 46).

79. Li, C. *et al.* An improved FIB sample preparation technique for site-specific plan-view specimens: A new cutting geometry. *Ultramicroscopy* **184,** 310–317 (Jan. 2018) (cit. on p. 46).

80. Thompson, K. *et al.* In situ site-specific specimen preparation for atom probe tomography. en. *Ultramicroscopy* **107,** 131–139 (Feb. 2007) (cit. on p. 46).

81. Babinsky, K. *et al.* A novel approach for site-specific atom probe preparation by focused ion beam and transmission electron backscatter diffraction. en. *Ultramicroscopy* **144,** 9–18 (Sept. 2014) (cit. on p. 47).

82. Urban Knut W. *et al.* Negative spherical aberration ultrahigh-resolution imaging in corrected transmission electron microscopy. *Philosophical Transactions of the Royal Society A: Mathematical, Physical and Engineering Sciences* **367,** 3735–3753 (Sept. 2009) (cit. on p. 47).

83. Scott, J. *et al.* Near-simultaneous dual energy range EELS spectrum imaging. *Ultramicroscopy* **108,** 1586–1594 (Nov. 2008) (cit. on p. 48).

84. Pryor Jr., A. *et al.* A Streaming Multi-GPU Implementation of Image Simulation Algorithms for Scanning Transmission Electron Microscopy. *arXiv:1706.08563 [physics].* arXiv: 1706.08563 (June 2017) (cit. on pp. 48, 71).

85. Tang, M. *et al.* Grain Boundary Transitions in Binary Alloys. *Physical Review Letters* **97,** 075502 (Aug. 2006) (cit. on p. 51).

86. Dillon, S. J. *et al.* Grain boundary complexions in ceramics and metals: An overview. en. *JOM* **61,** 38–44 (Dec. 2009) (cit. on pp. 51, 52).

87. Wang, Z. *et al.* Atom-resolved imaging of ordered defect superstructures at individual grain boundaries. en. *Nature* **479,** 380–383 (Nov. 2011) (cit. on p. 51).

88. Zhou, N. *et al.* Grain boundary complexions in multicomponent alloys: Challenges and opportunities. en. *Current Opinion in Solid State and Materials Science* **20,** 268–277 (Oct. 2016) (cit. on p. 51).

89. Dillon, S. J. *et al.* Complexion: A new concept for kinetic engineering in materials science. *Acta Materialia* **55,** 6208–6218 (Oct. 2007) (cit. on p. 51).

90. Merkle, K. L. & Smith, D. J. Atomic structure of symmetric tilt grain boundaries in NiO. *Physical Review Letters* **59,** 2887 (1987) (cit. on p. 51).

91. Yan, Y. *et al.* Impurity-induced structural transformation of a MgO grain boundary. *Physical review letters* **81,** 3675 (1998) (cit. on p. 51).

92. Liebscher, C. H. *et al.* Strain-Induced Asymmetric Line Segregation at Faceted Si Grain Boundaries. en. *Physical Review Letters* **121** (July 2018) (cit. on pp. 51, 64, 97).

93. Schweinfest, R. *et al.* Bismuth embrittlement of copper is an atomic size effect. en. *Nature* **432,** 1008–1011 (Dec. 2004) (cit. on p. 51).

94. Sigle, W. *et al.* Insight into the atomic-scale mechanism of liquid metal embrittlement. *Applied Physics Letters* **89,** 121911 (Sept. 2006) (cit. on p. 52).

95. Divinski, S. V. *et al.* Diffusion and segregation of silver in copper \Sigma 5(310) grain boundary. en. *Physical Review B* **85** (Apr. 2012) (cit. on pp. 52, 53).

96. Hickman, J. & Mishin, Y. Extra variable in grain boundary description. en. *Physical Review Materials* **1,** 010601 (June 2017) (cit. on pp. 52, 64).

97. Freitas, R. *et al.* Free energy of grain boundary phases: Atomistic calculations for Σ5(310)[001] grain boundary in Cu. *Physical Review Materials* **2.** arXiv: 1807.03274 (Sept. 2018) (cit. on p. 52).

98. Carrion, F. *et al.* Evidence for grain boundary phase transition in a 2d bicrystal. en. *Scripta Metallurgica* **17,** 915–918 (July 1983) (cit. on pp. 52, 63).

99. Guillopé, M. Transition de phase allotropique dans un joint \Sigma = 5 (210) a moyenne temperature. *Journal de Physique* **47,** 1347–1356 (1986) (cit. on p. 52).

100. Kundu, A. *et al.* Identification of a bilayer grain boundary complexion in Bi-doped Cu. *Scripta Materialia* **68,** 146–149 (Jan. 2013) (cit. on p. 54).

101. Dillon, S. J. & Harmer, M. P. Multiple grain boundary transitions in ceramics: A case study of alumina. *Acta Materialia* **55,** 5247–5254 (Sept. 2007) (cit. on p. 54).

102. Chookajorn, T. *et al.* Design of Stable Nanocrystalline Alloys. en. *Science* **337,** 951–954 (Aug. 2012) (cit. on p. 54).

103. Kalidindi, A. R. & Schuh, C. A. Stability criteria for nanocrystalline alloys. *Acta Materialia* **132,** 128–137 (June 2017) (cit. on p. 54).

104. Siow, K. S. *et al.* Mechanical properties of nanocrystalline copper and nickel. en. *Materials Science and Technology* **20,** 285–294 (Mar. 2004) (cit. on p. 54).

105. Khalajhedayati, A. *et al.* Manipulating the interfacial structure of nanomaterials to achieve a unique combination of strength and ductility. *Nature Communications* **7,** 10802 (Feb. 2016) (cit. on p. 54).

106. Khalajhedayati, A. *et al.* Manipulating the interfacial structure of nanomaterials to achieve a unique combination of strength and ductility. en. *Nature Communications* **7,** 10802 (Feb. 2016) (cit. on p. 54).

107. Liebscher, C. H. *et al.* Electronic structure of metastable bcc Cu–Cr alloy thin films: Comparison of electron energy-loss spectroscopy and first-principles calculations. *Ultramicroscopy* (cit. on pp. 54, 113).

108. Schiøtz, J. & Jacobsen, K. W. A Maximum in the Strength of Nanocrystalline Copper. en. *Science* **301,** 1357–1359 (Sept. 2003) (cit. on p. 54).

109. Schwaiger, R *et al.* Some critical experiments on the strain-rate sensitivity of nanocrystalline nickel. *Acta Materialia* **51,** 5159–5172 (Oct. 2003) (cit. on p. 54).

110. He, L. & Ma, E. Processing and microhardness of bulk Cu-Fe nanocomposites. *Nanostructured Materials* **7,** 327–339 (Mar. 1996) (cit. on p. 54).

111. Guduru, R. K. *et al.* Mechanical behavior of nanocrystalline copper. *Materials Science and Engineering: A. TMS 2006, Mukherjee Symposium* **463,** 14–21 (Aug. 2007) (cit. on pp. 54, 55).

112. Zhao, Y. H. *et al.* Tailoring stacking fault energy for high ductility and high strength in ultrafine grained Cu and its alloy. *Applied Physics Letters* **89,** 121906 (Sept. 2006) (cit. on p. 54).

113. Atwater, M. A. *et al.* The stabilization of nanocrystalline copper by zirconium. en. *Materials Science and Engineering: A* **559,** 250–256 (Jan. 2013) (cit. on pp. 54–56).

114. Manohar, P. A. *et al.* Five Decades of the Zener Equation. en. *ISIJ International* **38,** 913–924 (Sept. 1998) (cit. on pp. 54, 94, 95).

115. Darling, K. A. *et al.* Grain size stabilization of nanocrystalline copper at high temperatures by alloying with tantalum. *Journal of Alloys and Compounds* **573,** 142–150 (Oct. 2013) (cit. on p. 54).

116. Grant, E. *et al.* Grain-boundary migration in single-phase and particle-containing materials. en. *Journal of Materials Science* **19,** 3554–3573 (Nov. 1984) (cit. on p. 54).

117. Darling, K. *et al.* Thermal stability of nanocrystalline Fe–Zr alloys. en. *Materials Science and Engineering: A* **527,** 3572–3580 (June 2010) (cit. on p. 54).

118. Tschopp, M. A. & Maupin, H. E. *US Army Research Laboratory Lightweight and Specialty Metals Branch Research and Development (FY14)* tech. rep. (ARMY RESEARCH LAB ABERDEEN PROVING GROUND MD WEAPONS and MATERIALS RESEARCH DIRECTORATE, 2015) (cit. on p. 54).

119. Okamoto, H. Cu-Zr (Copper-Zirconium). en. *Journal of Phase Equilibria and Diffusion* **29,** 204–204 (Apr. 2008) (cit. on pp. 54, 57).

120. Khalajhedayati, A. *et al.* Manipulating the interfacial structure of nanomaterials to achieve a unique combination of strength and ductility. en. *Nature Communications* **7,** ncomms10802 (Feb. 2016) (cit. on pp. 54, 56, 58, 76, 96, 97).

121. Pan, Z. & Rupert, T. J. Effect of grain boundary character on segregation-induced structural transitions. en. *Physical Review B* **93** (Apr. 2016) (cit. on pp. 56, 96, 97).

122. Subramanian, P. R. & Laughlin, D. E. The CuTa (Copper-Tantalum) system. *Journal of Phase Equilibria* **10,** 652–655 (1989) (cit. on pp. 56, 57, 94).

123. Frolov, T. *et al.* Stabilization and strengthening of nanocrystalline copper by alloying with tantalum. en. *Acta Materialia* **60,** 2158–2168 (Mar. 2012) (cit. on pp. 56, 59, 93, 95).

124. Darling, K. *et al.* Grain size stabilization of nanocrystalline copper at high temperatures by alloying with tantalum. en. *Journal of Alloys and Compounds* **573,** 142–150 (Oct. 2013) (cit. on pp. 56, 59).

125. Zubkov, A. I. *et al.* Structure of vacuum Cu–Ta condensates. en. *Physics of Metals and Metallography* **118,** 158–163 (Feb. 2017) (cit. on p. 56).

126. Wang, H. *et al.* Microstructure and mechanical properties of sputter-deposited Cu 1- x Ta x alloys. *Metallurgical and Materials Transactions A* **28,** 917–925 (1997) (cit. on p. 56).

127. Misra, R. K. & Prasad, V. S. On the dynamic embrittlement of copper-chromium alloys by sulphur. *Journal of materials science* **35,** 3321–3325 (2000) (cit. on p. 59).

128. Briant, C. L. & Banerji, S. K. Tempered martensite embrittlement and inter-granular fracture in an ultra-high strength sulfur doped steel. en. *Metallurgical Transactions A* **12,** 309–319 (cit. on p. 59).

129. Fujiwara, S. & Abiko, K. Ductility of Ultra High Purity Copper. *Le Journal de Physique IV* **05,** C7–295–C7–300 (Nov. 1995) (cit. on pp. 59–61, 102).

130. Henderson, P. J. & Sandström, R. Low temperature creep ductility of OFHC copper. *Materials Science and Engineering: A* **246,** 143–150 (May 1998) (cit. on pp. 59, 60, 117, 119).

131. Van Agterveld, D. T. L. *et al.* Effects of precipitates in Cu upon impact fracture: an ultra-high-vacuum study with local probe Scanning Auger/Electron Microscopy. *Acta materialia* **48,** 1995–2004 (2000) (cit. on pp. 60, 61).

132. Korzhavyi, P. A. *et al.* Theoretical investigation of sulfur solubility in pure copper and dilute copper-based alloys. *Acta materialia* **47,** 1417–1424 (1999) (cit. on pp. 60, 118).

133. Moya, F. *et al.* Sulphur Diffusion in Copper: Departure from the Arrhenius Plot. *physica status solidi (b)* **35,** 893–901 (1969) (cit. on pp. 60, 114).

134. Moya, F. *et al.* Sulphur diffusion in copper: Small penetration curves. *physica status solidi (a)* **2,** 101–108 (1970) (cit. on p. 60).

135. Chakrabarti, D. J. & Laughlin, D. E. The Cu-S (copper-sulfur) system. *Bulletin of Alloy Phase Diagrams* **4,** 254–271 (1983) (cit. on pp. 60, 112, 118).

136. Surholt, T. & Herzig, C. Grain boundary self-diffusion in Cu polycrystals of different purity. *Acta Materialia* **45,** 3817–3823 (Sept. 1997) (cit. on p. 60).

137. *Landolt-Börnstein Zahlenwerte und Funktionen aus Naturwissenschaften und Technik: Neue Serie: = Numerical data and functional relationships in science and technology: new series. Gruppe 3 Bd. 26: Kristall- und Festkörperphysik = Crystal and solid state physics Diffusion in festen Metallen und Legierungen* eng (eds Mehrer, H. *et al.*) OCLC: 831323042 (Springer, Berlin, 1990) (cit. on p. 60).

138. Briant, C. L. & Messmer, R. P. The effect of impurity elements on chemical bonding at grain boundaries. *Le Journal de Physique Colloques* **43,** C6–255 (1982) (cit. on p. 60).

139. Fukushima, H. & Birnbaum, H. K. High resolution saes and sims studies of grain boundary segregation of S and Cl in Ni. *Scripta Metallurgica* **16,** 753–757 (1982) (cit. on p. 61).

140. Yamaguchi, M. Grain Boundary Decohesion by Impurity Segregation in a Nickel-Sulfur System. en. *Science* **307,** 393–397 (Jan. 2005) (cit. on p. 61).

141. Han, J. *et al.* Grain-boundary metastability and its statistical properties. en. *Acta Materialia* **104,** 259–273 (Feb. 2016) (cit. on pp. 63, 64).

142. Ference, T. & Balluffi, R. Observation of a reversible grain boundary faceting transition induced by changes of composition. en. *Scripta Metallurgica* **22,** 1929–1934 (Jan. 1988) (cit. on p. 64).

143. Brown, J. A. & Mishin, Y. Dissociation and faceting of asymmetrical tilt grain boundaries: Molecular dynamics simulations of copper. en. *Physical Review B* **76,** 134118 (Oct. 2007) (cit. on p. 64).

144. Lee, B.-K. *et al.* Grain boundary faceting and abnormal grain growth in BaTiO3. *Acta Materialia* **48,** 1575–1580 (Apr. 2000) (cit. on p. 64).

145. Straumal, B. B. *et al.* Review: grain boundary faceting–roughening phenomena. en. *Journal of Materials Science* **51,** 382–404 (Jan. 2016) (cit. on p. 64).

146. Frolov, T. *et al.* Segregation-induced phase transformations in grain boundaries. en. *Physical Review B* **92** (July 2015) (cit. on p. 64).

147. Frolov, T. *et al.* Structures and transitions in bcc tungsten grain boundaries and their role in the absorption of point defects. en. *Acta Materialia* **159,** 123–134 (Oct. 2018) (cit. on p. 64).

148. Aramfard, M. & Deng, C. Mechanically enhanced grain boundary structural phase transformation in Cu. en. *Acta Materialia* **146,** 304–313 (Mar. 2018) (cit. on pp. 64, 74).

149. Oganov, A. R. & Glass, C. W. Crystal structure prediction using *ab initio* evolutionary techniques: Principles and applications. en. *The Journal of Chemical Physics* **124,** 244704 (June 2006) (cit. on pp. 64, 67).

150. Lyakhov, A. O. *et al.* New developments in evolutionary structure prediction algorithm USPEX. *Computer Physics Communications* **184,** 1172–1182 (Apr. 2013) (cit. on pp. 64, 67).

151. Kuzmina, M. *et al.* Linear complexions: Confined chemical and structural states at dislocations. en. *Science* **349,** 1080–1083 (Sept. 2015) (cit. on p. 76).

152. Hu, T. *et al.* Role of disordered bipolar complexions on the sulfur embrittlement of nickel general grain boundaries. en. *Nature Communications* **9** (Dec. 2018) (cit. on p. 76).

153. Krakauer, B. W. & Seidman, D. N. Absolute atomic-scale measurements of the Gibbsian interfacial excess of solute at internal interfaces. *Physical Review B* **48,** 6724 (1993) (cit. on p. 89).

154. Felfer, P. J. *et al.* A quantitative atom probe study of the Nb excess at prior austenite grain boundaries in a Nb microalloyed strip-cast steel. en. *Acta Materialia* **60,** 5049–5055 (Aug. 2012) (cit. on p. 89).

155. Cahn, J. W. The impurity-drag effect in grain boundary motion. *Acta Metallurgica* **10,** 789–798 (Sept. 1962) (cit. on p. 94).

156. Koju, R. K. *et al.* Zener Pinning of Grain Boundaries and Structural Stability of Immiscible Alloys. en. *JOM* **68,** 1596–1604 (June 2016) (cit. on p. 95).

157. Koju, R. K. *et al.* Atomistic modeling of capillary-driven grain boundary motion in Cu-Ta alloys. *Acta Materialia* **148,** 311–319 (Apr. 2018) (cit. on p. 95).

158. Schuler, J. D. & Rupert, T. J. Materials selection rules for amorphous complexion formation in binary metallic alloys. en. *Acta Materialia* **140,** 196–205 (Nov. 2017) (cit. on p. 96).

159. Borovikov, V. *et al.* Effects of grain boundary disorder on dislocation emission. *Materials Letters* **237,** 303–305 (Feb. 2019) (cit. on p. 97).

160. Da Rosa, G. *et al.* Co-segregation of boron and carbon atoms at dislocations in steel. *Journal of Alloys and Compounds* **724,** 1143–1148 (Nov. 2017) (cit. on p. 105).

161. Larson, D. J. *et al. Local Electrode Atom Probe Tomography* en (Springer New York, New York, NY, 2013) (cit. on p. 106).

162. Yao, L. *et al.* On the multiplicity of field evaporation events in atom probe: A new dimension to the analysis of mass spectra. en. *Philosophical Magazine Letters* **90,** 121–129 (Feb. 2010) (cit. on pp. 106, 107).

163. de, L. J. R. *et al.* Atomic weights of the elements. Review 2000 (IUPAC Technical Report). *Pure and Applied Chemistry* **75,** 683–800 (2009) (cit. on p. 109).

164. *EMS, Emergency Medical Services - Training, Paramedic, EMT News & Magazine - JEMS.com* (cit. on p. 112).

165. Leapman, R. D. *et al.* Study of the L 23 edges in the 3 d transition metals and their oxides by electron-energy-loss spectroscopy with comparisons to theory. *Physical Review B* **26,** 614 (1982) (cit. on p. 113).

166. Laporte, V & Mortensen, A. Intermediate temperature embrittlement of copper alloys. en. *International Materials Reviews* **54,** 94–116 (Mar. 2009) (cit. on p. 114).

167. Watanabe, M. & Williams, D. B. Atomic-level detection by X-ray microanalysis in the analytical electron microscope. *Ultramicroscopy* **78,** 89–101 (1999) (cit. on p. 116).

168. Watanabe, T. *et al.* Grain boundary hardening and segregation in alpha Iron-Tin alloy. *Acta Metallurgica* **28,** 455–463 (Apr. 1980) (cit. on p. 117).

169. Pineau, A. *et al.* Grain boundary cosegregation and diffusion in Cu (Fe, S) solid solution. *Acta Metallurgica* **31,** 1047–1052 (1983) (cit. on p. 117).

170. Bouchet, D. *et al.* EXPERIMENTAL EVIDENCE OF SULFUR EFFECT ON THE PLANE AND ON THE EXTRINSIC DISLOCATIONS OF A Sigma = 3 GRAIN BOUNDARY IN NICKEL. *Le Journal de Physique Colloques* **49,** C5–417–C5–422 (Oct. 1988) (cit. on p. 118).

171. Fraczkiewicz, A. & Biscondi, M. INTERGRANULAR SEGREGATION OF BISMUTH IN COPPER BICRYSTALS. *Le Journal de Physique Colloques* **46,** C4–497–C4–503 (Apr. 1985) (cit. on p. 118).

172. Swiatnicki, W. *et al.* INTERGRANULAR SULFUR SEGREGATION AND GRAIN BOUNDARY PLANE IN A NICKEL BICRYSTAL. en. *Le Journal de Physique Colloques* **51,** C1–341–C1–346 (Jan. 1990) (cit. on p. 118).

173. *Chalcocite Mineral Data* (cit. on p. 119).

174. Quintana-Ramirez, P. V. *et al.* Growth evolution and phase transition from chalcocite to digenite in nanocrystalline copper sulfide: Morphological, optical and electrical properties. *Beilstein Journal of Nanotechnology* **5,** 1542–1552 (Sept. 2014) (cit. on p. 119).

A. Appendix

A.1. Supplementary information to chapter 6

In the following additional information is provided to supplement the results from the study presented in chapter 6. The first subsection deals with the multi-slice simulations of selected structures from the USPEX algorithm.

Grain boundary structures of simulated STEM images

The grain boundary energy of pearl structures is plotted against the number of inserted atoms [n] as fraction of the (178) GB plane in A.1 (a). The approximate locations of the input GB structures used for STEM image simulations in the plot are highlighted by red, green and yellow circles, respectively. In A.1 (b), (c) and (d), the corresponding projections of the GB structures along the [$11\bar{1}$] tilt axis and perpendicular to it are shown in the left and right panels, respectively. The ground state structure of the pearl phase, as predicted by USPEX at $0\,K$, with a GB energy of $0.835\,J/m^2$ is shown in A.1 (b), highlighted in red. The higher energy structures with GB energies of $0.932\,J/m^2$ (green) and $1.023\,J/m^2$ (yellow) are illustrated in A.1 (c) and (d). Locations where atoms are displaced from there ideal positions with respect to the [$11\bar{1}$] viewing direction are marked by arrows in A.1 (b). The atomic displacements in these regions leads to de-channeling of the electron probe and hence a reduction of the HAADF-STEM image intensity.
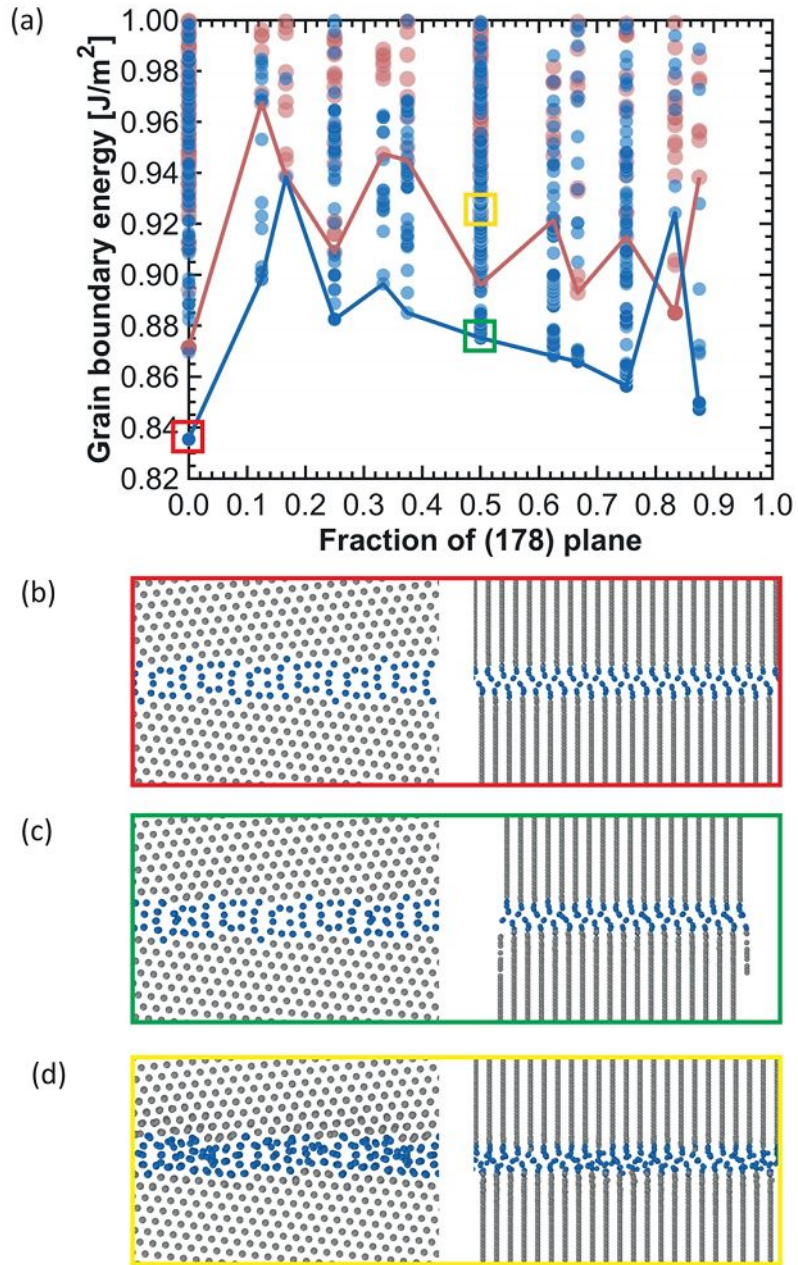
Fig. A.1.: Input GB structures for STEM image simulations. (a) GB energy plotted versus the number of inserted atoms [*n*] as fraction of the (178) GB plane. The red, green and yellow circles indicate the locations of the GB structures shown in (b) to (d). (b) to (d) show the three GB structures used for STEM image simulation. The left panel shows the structure along the tilt axis [11$\bar{1}$], the right panel perpendicular to the tilt axis. The colored boxes indicate where these structures are located in the energy plot.

A.1.1. Grain boundary phase transitions at finite temperatures

A.1.2. Symmetric tilt grain boundary

To model the transition from the metastable domino phase to the pearl phase, we performed independent isothermal simulations at temperatures of $300\,K$, $400\,K$, $500\,K$, $600\,K$, $650\,K$, $700\,K$, $800\,K$, $850\,K$ and $900\,K$. We used blocks with periodic boundary conditions along the boundary as well as blocks with open surfaces. We also used different sizes of the simulation block to investigate the effect of the GB phase junction length on the kinetics of the transformation.

Simulations with periodic boundary conditions parallel to the GB plane. We used a simulation block with dimensions $3.6 \times 34 \times 14\,nm^3$ containing $1,339,740$ atoms. The z direction was normal to the GB plane. The simulations were performed for up to $200\,ns$. We observed a transformation of the domino phase to the pearl phase at $850\,K$ and $900\,K$. At temperatures below $850\,K$, the initial domino phase remained stable and well ordered throughout the entire simulation. Based on these simulations, we estimated the limit of pearl phase stability to be around $900\,K$. The simulations also confirmed that the supply of atoms was not necessary for the transformation.

Simulations with open surface. When the boundary was terminated at an open surface, we were able to observe the transition from domino to pearl at much lower temperatures. In all of these simulations the pearl phase nucleated at the surface triple junctions. The simulations showed strong effect of temperature on the kinetics of the transformation. The initial simulation block had dimensions of $45 \times 0.626 \times 14\,nm^3$ and contained $33,080$ atoms. Here, the y periodic dimension, which also defines the length of the GB phase junction, was only one periodic unit length along the $[11\bar{1}]$ direction $L_y = a_0 \times \sqrt{3} = 0.626\,nm$. In this quasi-2d simulations, we were able to observe the nucleation of the pearl phase at 400K, which was significantly lower compared to the homogeneous nucleation at $850\,K$ in a block with periodic boundary conditions.

However, after the pearl phase nucleated, the migration of the junction was too slow and we were not able to observe a complete transformation at this temperature. At $300\,K$ we did not observe pearl phase nucleation at all. More rapid nucleation kinetics and complete transformations were observed at higher temperatures of $500\,K$, $600\,K$ and $650\,K$. Already at $500\,K$, the full transformation was completed within only $13\,ns$ of the simulation. During this time, the two GB junctions travel the distance of $L_x = 45\,nm$. In principle, these simulations allow to evaluate the velocity of the GB junction and, by approximating the driving force as the GB energy difference at $0\,K$, even the mobility of the GB phase junction at $300\,K$ can be predicted on the experimental time-scale. However, while these simulations with the artificially short dimension $L_y = 0.626\,nm$ allowed to observe GB phase transitions at low temperatures, they are likely to overestimate the mobility of the GB phase junction.

To study the effects of the GB phase junction length, we increased the size L_y of the simulation block by replicating the initial block along the periodic direction y 40 times. The final dimensions of the simulation block were $45 \times 25 \times 14\,nm^3$ and it contained $1,323,200$ atoms. The initial configurations were taken from the middle of the $500\,K$ simulation and contained both the pearl and the domino phases. We obtained the large simulation block for $200\,ns$ at $500\,K$ and did not observe any substantial migration of the GB phase junction. This behavior was very different from a complete transformation at the same temperature in a thinner block, in which the GB phase junctions traveled the entire length L_x of $45\,nm$. In these simulations, we effectively froze the transformation at $500\,K$ by making the GB phase junction longer. At higher temperatures such as $650\,K$, we observed a complete transformation again even in the thicker block during $48\,ns$ of the simulation.

A.1.3. Asymmetric tilt grain boundary

The asymmetric boundary is $6°$ inclined relative to the symmetric orientation. Its periodic dimensions were substantially larger than that of the symmetric boundary. As a result, we did not attempt a full grand canonical optimization of the boundary with USPEX. Instead, we used the common gamma-surface method which neverthe-

less generated both pearl and domino structures with energies of $\gamma_{gb} = 0.87 \, J/m^2$ and $0.89 \, J/m^2$, respectively. Due to the different inclination, the energy difference between the two structures reduces to 1.9 %, which is even smaller than that for the symmetric GB. The structures of both asymmetric pearl and domino ground states are shown in A.2.
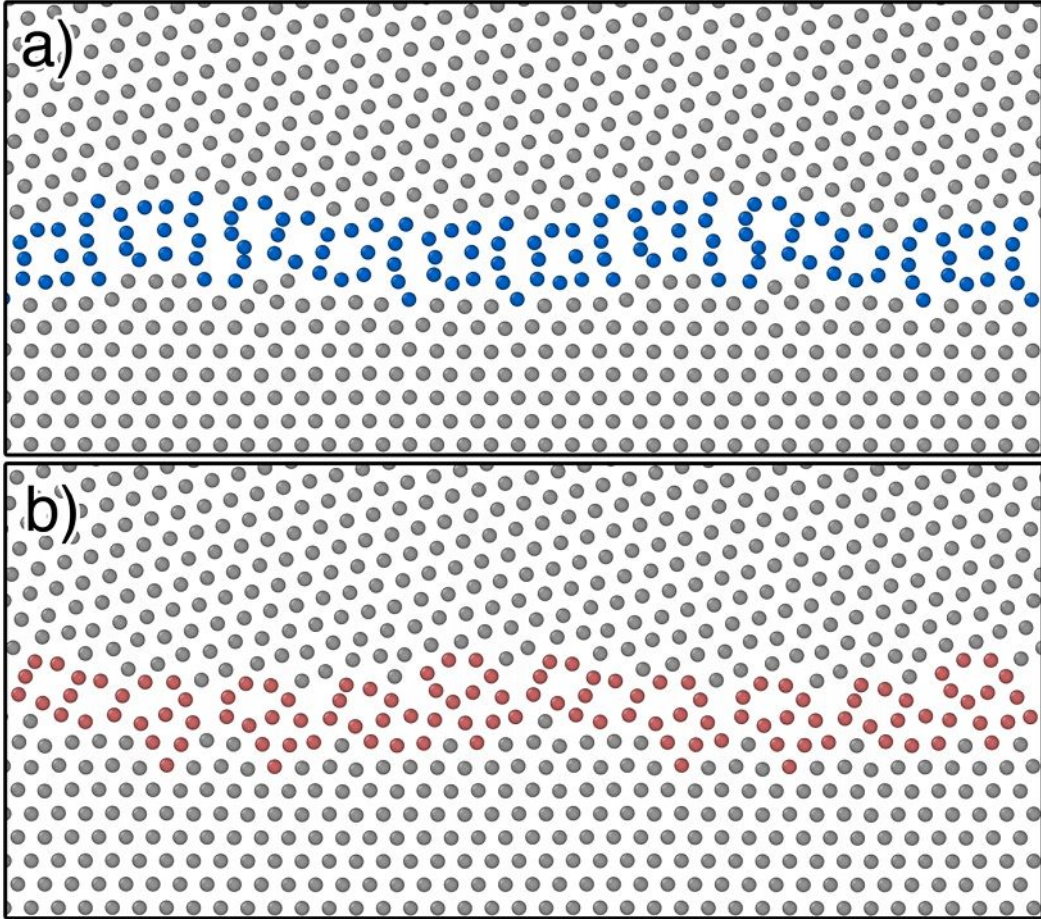

Fig. A.2.: Asymmetric grain boundary structures. (a) Ground state pearl and (b) metastable domino structures of the asymmetric boundary at 0K. The two structures have the same number of atoms and correspond to two different translations of the bulk grains relative to each other.

Despite the smaller energy difference at $0\,K$, the pearl phase remains more stable at finite temperature for the asymmetric GB. MD simulations of a transformation from domino to pearl structure were performed at $600\,K$, $700\,K$, $800\,K$ and $900\,K$ using simulation blocks with dimensions of $34 \times 2.5 \times 3.1\,nm^3$ containing $43,248$ atoms. At these temperatures, we observed complete transformations to pearl phase as illustrated in A.3 and A.4. We intentionally used a relatively small size $L_z = 3.1\,nm$ to stabilize the asymmetric configuration.
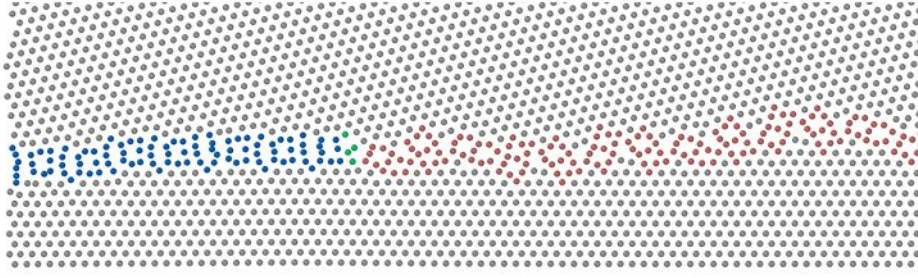
Fig. A.3.: Early stage of the asymmetric grain boundary transformation at $600\,K$**.** Nucleation of a pearl GB phase at the open surface (left) at the asymmetric GB at $600\,K$.
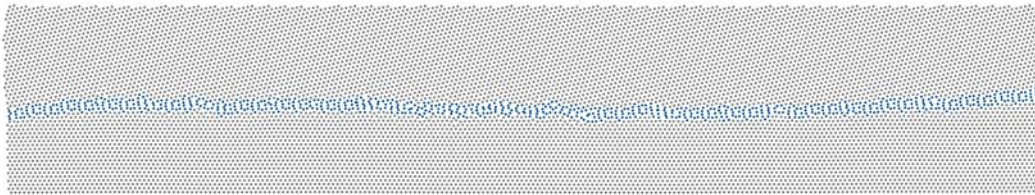

Fig. A.4.: Completed asymmetric grain boundary transformation at $600\,K$**.** Asymmetric pearl GB phase after the transformation at $600\,K$ is complete. The boundary remains asymmetric.

Interestingly, at a temperature of $600\,K$, the GB in the pearl structure remained asymmetric, while at all higher temperatures the symmetric configuration appears. The nucleation of the asymmetric pearl phase from the open surfaces at $700\,K$ is shown in A.5. The transformation from the initially asymmetric domino structure to the symmetric pearl phase is illustrated in A.6.

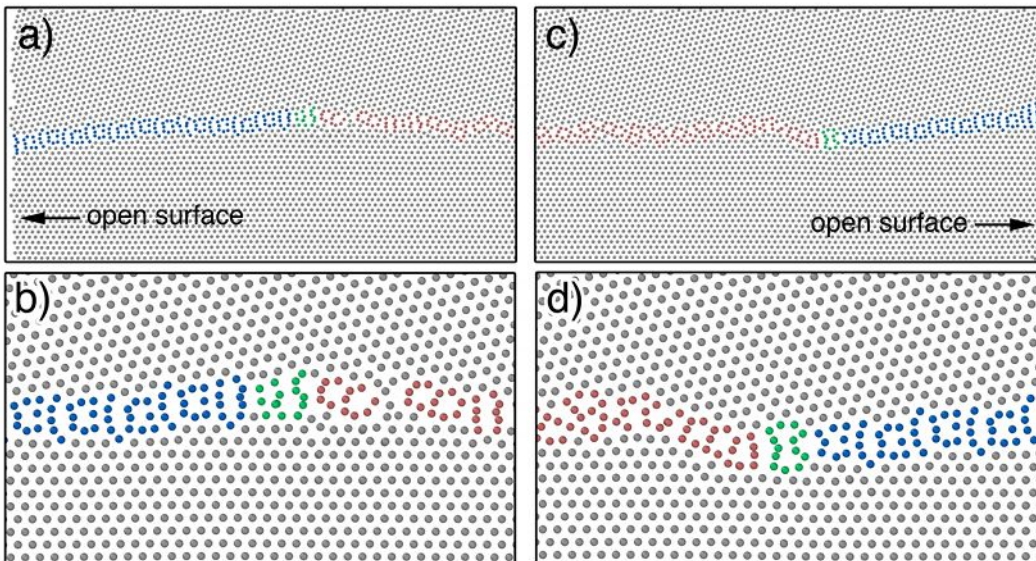**Fig. A.5.: Early stage of the asymmetric grain boundary transformation at** $700\,K$**.** (a) and (b) show the nucleation of the pearl GB phase from the open surface on the left of the simulation cell. (c) and (d) from the right.

Fig. A.6.: Asymmetric to symmetric grain boundary transformation at $700\,K$**.** The asymmetric domino structure transformed into a symmetric pearl phase in MD at $700\,K$.

A.2. Influence of grain boundary inclination on the atomic structure of [111] tilt GBs

The two symmetric GBs (zipper and pearl structure), presented in this thesis, differ only in GB plane inclination by 30°, but show a very different GB core structure. Since the grains have a cylindrical shape, the GBs are often not perfectly symmetric, but show slightly asymmetric variations. While the $\Sigma 19b(2\bar{5}3)$ forms steps between symmetric facets, the $\Sigma 19b(1\bar{8}7)$ introduces additional structural sub-units into the GB core structure.

In case of the zipper structure ($\Sigma 19b(2\bar{5}3)$), the GB incorporates steps between symmetric $(2\bar{5}3)$ facets. Two examples are shown in Fig. A.7 with different GB plane inclination, namely (a) $(\bar{4}31)(12\bar{6}\bar{5})$ and (b) $(1\bar{3}2)(1\bar{2}1)$. The steps shown a much more disordered structure than the symmetric facets and structural units can not be identified. The step spacing between the facets in the two GBs is very different. In Fig. A.7 (a) is is $\sim 2.5\,nm$ and in Fig. A.7 (b) $\sim 5.2\,nm$. Therefore, it can be concluded that the amount of steps scales with the degree of asymmetry, which is in (a) $\sim 10°$ and in (b) $\sim 5.5°$. Thus, the asymmetry is roughly doubled from $\sim 5.5°$ to $\sim 10°$ and the step spacing is also reduced by roughly a factor of two. To visualize the different GB planes, the two asymmetric planes from Fig. A.7 (a) and (b) are translated into the symmetric $\Sigma 19b(2\bar{5}3)$ from chapter 7 in Fig. 7.2 (a). This is shown in Fig. A.7 (c), where the orange line corresponds to the inclination in Fig. A.7 (a) $(\bar{4}31)(12\bar{6}\bar{5})$ and the red line to Fig. A.7 (b) $(1\bar{3}2)(1\bar{2}1)$. The purple line belongs to the symmetric $(2\bar{5}3)$ plane.

In the pearl structure, a different behavior is observed and is demonstrated in Fig. A.8 (a) and (b), also for two different asymmetric GB inclinations. The inclination can be described by the planes $(210\bar{1}\bar{1})(15\bar{6})$ in (a) and $(161\bar{1}\bar{7})(\bar{6}15)$ in (b). Instead of forming symmetric facets separated by GB steps, additional structural sub-units are incorporated into the GB core, which is indicated by the colored arrows in Fig. A.8 (a) and (b). A corresponding magnified view is given by the yellow and red box. The extra sub-unit appears similar to the pearl unit in a slightly modified/distorted way. In (a) the spacing between those sub-units is $\sim 7\,nm$ and in (b) $\sim 2.5\,nm$, which results

(a) 45.5° [111],($\bar{4}$31)(12 $\bar{6}\bar{5}$)　(b) 47° [111],(1$\bar{3}$2)(1$\bar{2}$1)　(c) Σ19b [111],(2$\bar{5}$3)

10° off from symmetric　　5.5° off from symmetric　　($\bar{4}$31)(12 $\bar{6}\bar{5}$) ,(1$\bar{3}$2)(1$\bar{2}$1) ,(2$\bar{5}$3)
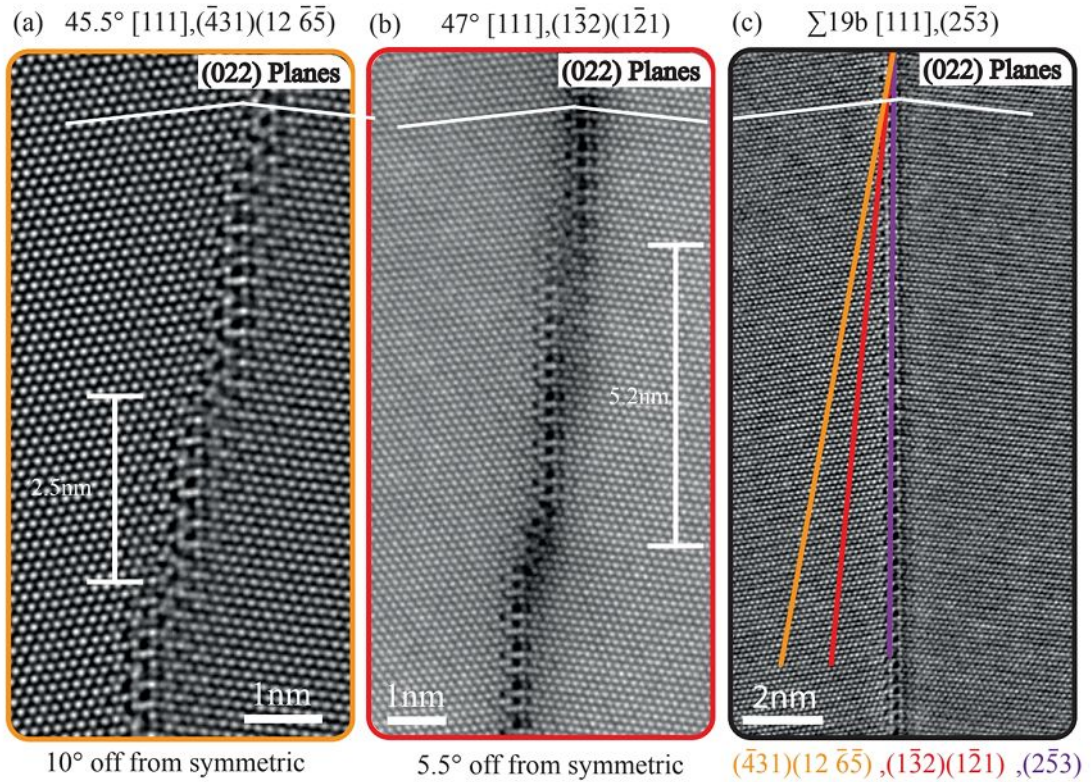
Fig. A.7.: Influence on the GB inclination on the zipper structure:(a) and (b) show HAADF STEM images on two different, asymmetric zipper structures. In (c), their GB planes are transferred to a symmetric $\Sigma\,19\,b\,(2\bar{5}3)$ to visualize the GB plane differences.

in a ratio of roughly 1 : 3. In addition, the GB in (b) appears not straight anymore but reveals a wavy character, which locally changes the plane inclination back and forth. MD simulations at $0\,K$ at an asymmetric $(0\bar{1}1)(\bar{9}27)$ (which is very close the the GB in (b)) results in the same behavior, as shown in Fig. A.8 (c). Also here the GB shows a wavy character and introduces additional sub-units, indicated by orange arrows. The inclination in Fig. A.8 (a) differs from the symmetric $(1\bar{8}7)$ plane by $\sim 1.5°$ and in (b) by $\sim 3.2°$, which is a ratio of roughly 2 : 1. Thus, with higher degree of misorientation, more sub-units are introduced. The wavy character is not seen for the less asymmetric GB (as in Fig. A.8 (a)), but only at higher degrees as in Fig. A.8 (b). In Fig. A.9, the GB planes of the symmetric and two asymmetric GBs are compared. For that each image was aligned with respect to the (022)-planes and then a line was drawn along the GB (see (a) for the symmetric $(1\bar{8}7)$ GB, (b) and (c) for asymmetric $(210\bar{1}1)(15\bar{6})$ and $(161\bar{1}7)(\bar{6}15)$). In Fig. A.9 (d) all planes have been translated to the symmetric GB to visualize the different inclinations. Higher inclinations, as in the

zipper structure with ~ 10° have not been observed in the pearl structure.

(a) 47° [111],(2 10 $\bar{1}\bar{1}$)(15$\bar{6}$) (b) 48°[111],(16 1 $\bar{1}\bar{7}$)($\bar{6}$15) (c) 46.83° [111]($0\bar{1}1$)($\bar{9}$27)
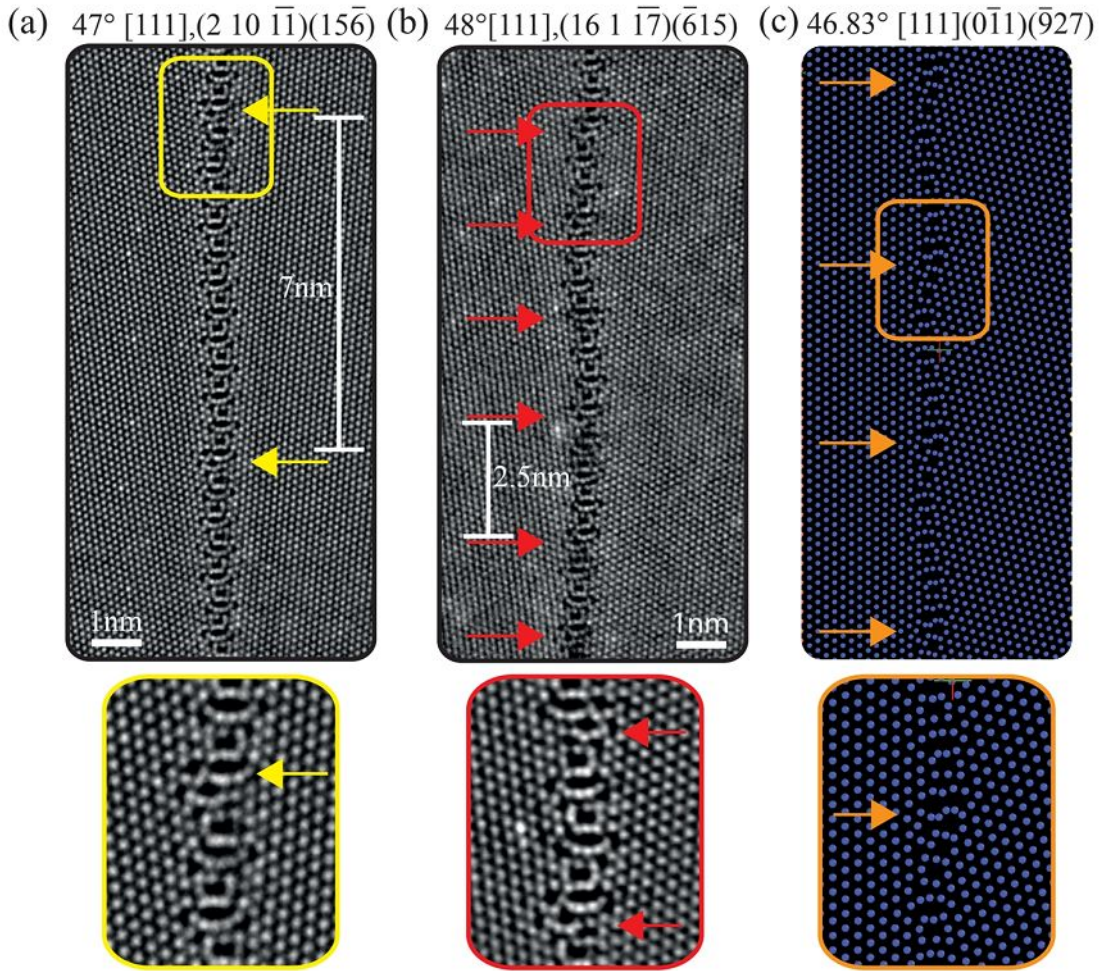

Fig. A.8.: Influence on the GB inclination on the pearl structure: (a) and (b) demonstrate two HAADF STEM images different, asymmetric pearl structures. In (c), a corresponding MD simulation was carried out on a similar asymmetric boundary showing very similar characteristic compared to the experiment. The arrows indicate in each case the positions of additional sub-units. Below each images a magnified view on these additional sub-units is shown.
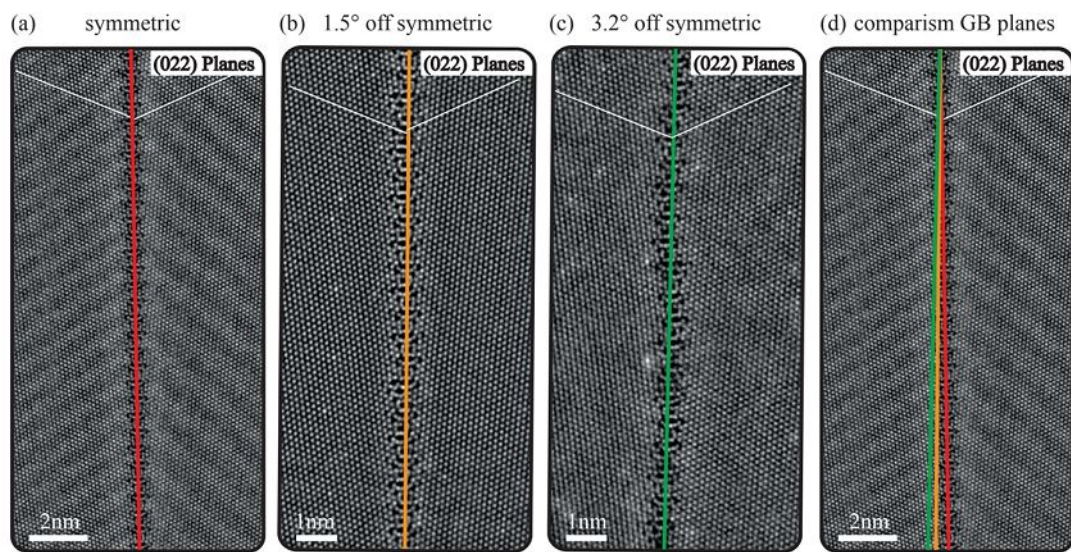
Fig. A.9.: Comparison of the GB inclination of the symmetric and asymmetric pearl GBs: (a-c) show HAADF STEM images of the different pearl GBs and the colored line indicates the GB plane inclination. In (d) all GB planes are transferred to the symmetric $\Sigma 19\,b\,(1\bar{8}7)$ to visualize the inclination differences.

B. Curriculum vitae

Personal data

Name	Thorsten Meiners
Date of birth	05.12.1988
Place of birth	Lingen (Ems), Germany
Nationality	German

Education

2008	Abitur, Windthorst Gymnasium Meppen, Germany
2008-2009	Community service, Kindergarten St. Bernadette Dalum, Germany
2009-2012	Academic study of Physics (Bachelor of Science), Rheinisch-Westfälische Technische Hochschule Aachen, Germany
2012-2015	Academic study of Physics (Master of Science), Rheinisch-Westfälische Technische Hochschule Aachen, Germany
2013-2014	Semester abroad within the ERASMUS program (Photonics), Universitat Autónoma de Barcelona, Spain
2015-2019	PhD thesis under supervision of Prof. Dr. rer. nat. Gerhard Dehm, Max-Planck-Institut für Eisenforschung GmbH in Düsseldorf, Germany. Title: *Grain Boundary Structure, Phase Transitions and Segregation Phenomena in Copper Alloys*

Professional Experience

2019-present	Customer Support and Application, Oxford Instruments GmbH, Nano Analysis, Germany

Advanced trainings

2017	Electron energy loss spectroscopy Workshop from Gatan, Application Center Jeol Germany in Munich, Germany
2017	Quantitative electron microscopy workshop 2017, Balaruc-les-Bains, France

First author publications

2018	Meiners, T., Peng, Z., Gault, B., Liebscher, C. H., Dehm, G.: Sulfur – induced embrittlement in high-purity, polycrystalline copper. *Acta Materialia* **156**, 64-75 (Sept. 2018).
2020	Meiners, T., Frolov, T., Rudd, R.E., Dehm, G., Liebscher, C. H.: Observations of grain boundary phase transitions in an elemental metal. *Nature* **579**, 375-378 (2020).

Co-author publications

2017   Z. Peng, M. Rohwerder, P.-P. Choi, B. Gault, T. Meiners, M. Friedrichs, H. Kreilkamp, F. Klocke, D. Raabe, Atomic diffusion induced degradation in bimetallic layer coated cemented tungsten carbide, *Corrosion Science* **120**.

2017   B. Arndt, F. Borgatti, F. Offi, M. Phillips, P. Parreira, T. Meiners, S. Menzel, K. Skaja, G. Panaccione, D.A. MacLaren, R. Waser, R. Dittmann, Spectroscopic Indications of Tunnel Barrier Charging as the Switching Mechanism in Memristive Devices, *Adv. Funct. Mater.* **27**.

2018   S.K. Makineni, A. Kumar, M. Lenz, P. Kontis, T. Meiners, C. Zenk, S. Zaefferer, G. Eggeler, S. Neumeier, E. Spiecker, D. Raabe, B. Gault, On the diffusive phase transformation mechanism assisted by extended dislocations during creep of a single crystal CoNi-based superalloy, *Acta Materialia* **155**.

Oral presentation at national and international conferences

2017   Meiners, T.; Peng, Z.; Liebscher, C.H.; Dehm, G.: Grain boundary embrittlement in copper by sulfur. DPG Tagung 2017, Dresden, Germany

2017   Meiners, T.; Peng, Z.; Gault, B.; Liebscher, C.; Dehm, G.: Sulfur-induced embrittlement of copper. Microscopy congress 2017 – Dreiländertagung (MC 2017), Lausanne, Switzerland

2018   Meiners, T.; Frolov, T.; Liebscher, C.H.; Dehm, G.: Direct observation of novel structures and transitions in Cu [111] tilt grain boundaries. DPG Tagung 2018, Berlin, Germany

2018   Meiners, T.; Frolov, T.; Liebscher, C.H.; Dehm, G.: Experimental observation of novel long-period structures and phase transitions in fcc [111] tilt grain boundaries by atomic resolution STEM, 19th international microscopy congress 2019, Sydney, Australia

2018   Meiners, T.; Frolov, T.; Liebscher, C.H.; Dehm, G.: Experimental observation of novel long-period structures and phase transitions in [111] tilt grain boundaries. MRD Young Materials Researcher Day, Bochum, Germany

2019   Meiners, T.; Frolov, T.; Duarte, M.J.; Liebscher, C.H.; Dehm, G.: Influence of Ta and Zr segregation on the atomic structure of [111] tilt GBs in Copper, DPG Tagung 2019, Regensburg, Germany

Poster presentation at national and international conferences

2017   Meiners, T.; Liebscher, C.; Dehm, G.: Atomic structure and segregation phenomena at copper grain boundaries. EMC2016, The 16th European Microscopy Congress, Lyon, France

2018   Meiners, T.; Frolov, T.; Liebscher, C.H.; Dehm, G.: Direct observation of novel structures and transitions in [111] Cu tilt grain boundaries. Materials Day Ruhr-Universität Bochum, Germany

2019   Meiners, T.; Duarte, M.J.; Liebscher, C.H.; Dehm, G.: Segregation-induced structural transitions in [111] tilt grain boundaries in Cu, Pico 2019, Frontiers of aberration corrected electron microscopy fifth conference, Kasteel Vaalsbroek, Netherlands